Photoemission Spectroscopy of a Strongly Interacting Fermi Gas

by

John Pagnucci Gaebler

B.S., Rice University, 2004

A thesis submitted to the

Faculty of the Graduate School of the

University of Colorado in partial fulfillment

of the requirements for the degree of

Doctor of Philosophy

Department of Physics

2010

This thesis entitled:
Photoemission Spectroscopy of a Strongly Interacting Fermi Gas
written by John Pagnucci Gaebler
has been approved for the Department of Physics

Deborah Jin

Eric Cornell

Date _____

The final copy of this thesis has been examined by the signatories, and we find that both the content and the form meet acceptable presentation standards of scholarly work in the above mentioned discipline.

Gaebler, John Pagnucci (Ph.D., Physics)

Photoemission Spectroscopy of a Strongly Interacting Fermi Gas

Thesis directed by Prof. Deborah Jin

The ability to study ultracold atomic Fermi gases holds the promise of significant advances in testing fundamental theories of many-body quantum physics. Of particular interest are strongly interacting Fermi gases in the BCS to BEC crossover that exhibit a transition to a superfluid state at temperatures near $0.2T_F$, where T_F is the Fermi temperature. This transition, as a fraction of T_F, is extremely high compared to any known superfluid or superconductor. These gases are also in a universal regime where the physics is independent of the details of the atomic interactions and is therefore relevant to fields as diverse as condensed matter, nuclear physics and astrophysics. In this thesis, I present an experimental probe of atomic gases that uses momentum-resolved RF spectroscopy to realize an analog of angle-resolved photoemission spectroscopy (ARPES) in materials. This measurement reveals the energy and momentum of single-particle states in the strongly interacting Fermi gas. In condensed matter, ARPES has proved to be one of the most powerful experimental techniques for studying the electronic structure of strongly correlated electron materials. The ability to perform analogous measurements in ultracold Fermi gases constitutes a significant advance in our ability to directly connect ultracold atomic gases to strongly correlated electron systems. Taking advantage of this new measurement technique, I investigate a long-standing problem in the field of strongly interacting fermions, namely whether a pseudogap state consisting of incoherent fermion pairs exists at temperatures above the critical temperature for superfluidity. The photoemission data I present provide strong evidence for this state and have implications for fundamental theories of strongly interacting Fermi gases and strongly correlated electron materials. I also discuss the experimental confirmation of recently predicted universal relations for strongly interacting Fermi gases, as well as some of the first experiments involving atomic Fermi gases with p-wave pairing.

Acknowledgements

This thesis represents the work of nearly six years of my life, and as it is with most things, it would simply not have been possible without all of the people around me, not even close. First, there are the people without whom I would never have come here in the first place. I should thank my parents first. They have encouraged me nearly every day of my entire life and helped me through so many problems and challenges. I want to thank my mom for encouraging me, helping me stay organized, and always fighting for the best for me. Sometimes having an Italian mother willing to go all the way for her children comes in handy. Grazie mille mama. I want to thank my dad for being my chess coach, for building model airplanes and science projects in the garage with me, for helping me with my homework despite my ADD, for encouraging me in math and science, and for being a great dad. I know you became a lawyer (I blame Harvard), but I'm sure you could easily have been a great scientist in another life. I'd like to thank my Gramps for being a wonderful grandfather and for always being, at least to me, a model intellectual with great compassion and humanity, and an extraordinary mind. It meant a lot to see you at my thesis defense. I'd also like to thank my siblings, it is so nice to have you both as good friends now that we are finally grown up.

I should also thank all of my teachers. In particular, my high school physics teacher Mr. Pettus introduced me to the subject that I've never stopped studying. He challenged me and that has kept my interest ever since. The way I feel about physics can be summed up by a quote from John F. Kennedy who, in a now famous speech in Rice stadium, said "Why go to the moon? They may well ask...why does Rice play Texas? Not because [it is] easy, but because [it is] hard." I may

still get confused by basic quantum mechanics, and Rice may loose to Texas by 30 points and call it a good game, but at least it's not easy.

I had a number of great professors at Rice who helped me along the way. I'd like to thank Paul Padley for advising me and giving me the opportunity to work at Fermi Lab, and Paul Stevenson for being such an excellent teacher of quantum mechanics. Most importantly, I'd like to thank Randy Hulet. I can still remember the day in our modern physics class when he described an experiment in which electrons pass through a double slit mask and form an interference pattern. It was at that moment when it struck me how amazing quantum mechanics is and that feeling has never really left me since. He also told us about laser cooling of atoms, which later inspired me to come to him and ask for the opportunity to work in his lab, which he gladly afforded me. It was that experience that ultimately led me to apply to the University of Colorado and seek a research assistantship with Debbie Jin. I should also thank Randy for contacting Alain Aspect and helping me set up my year abroad in France after college. That was a great year where I made many good friends from all over the world. What I learned working in Alain Aspect's lab really made a difference when I started at JILA. I must also thank the French department at Rice and the Clyde Bull Ferguson travel fellowship they offered me that made that year possible.

The work in this thesis is the research I performed in Debbie Jin's group at JILA and I thank her for being such a wonderful advisor. She is an outstanding scientist and an incredibly clear thinker. However, I would especially like to thank her for treating me as a colleague and taking my ideas seriously, even at the beginning of graduate school when I barely knew what I was talking about half of the time (still the case occasionally). This gave me the confidence to keep trying out my own ideas, and eventually function as a real scientist (most of the time). One of the things I enjoyed most in graduate school was sitting around with Debbie and brainstorming ideas or coming up with research strategies. I especially need to thank Jayson Stewart, who worked along side me for nearly all of what is in this thesis. Jayson is a very talented experimentalist and certainly deserves equal credit for the majority of the work in this thesis. I think we made a really great research team and I had a lot of fun, whether it was messing around in the lab, mountain biking

before work, fishing for trout, or skiing. I look forward to keeping up contact with Jayson and am sure he will be a very successful scientist. I'd also like to thank Tara Drake and Rabin Paudel, the more recent additions to our group. They have been very helpful, and will undoubtedly do a great job carrying on this research.

I'd like to thank Brian DeMarco, Debbie Jin, and Cindy Regal for building such a great experiment and laying the groundwork for the research in this thesis. As many scientists have noted at one time or another, we only see farther than others by standing on the shoulders of the giants before us.

I'd also like to thank all of the Jin and Cornell group members who have become my good friends and helped me so many times. I'd like to especially thank Juan Pino, Josh Zirbel, Kang-Kuen Ni, Michele Olsen, Russ Stutz, Laura Sinclair, Aaron Leanhardt, Rob Wild, Tyler Cumby, Marcio Miranda, Brian Neyenhuis, Silke Ospelkaus, Huanqian Loh, Ruth Shewmon, and Phil Makotyn.

I also need to acknowledge all the help I have gotten from theorists, here at JILA and elsewhere. John Bohn is an amazing resource for atomic physics knowledge and his calculations were particularly useful for the p-wave Feshbach resonance paper. Leo Radzihovsky, Victor Gurarie, and Jim Shepard helped me better understand many-body theory and condensed matter ideas. I would also like to thank the Strinati group in Camerino, Italy and especially Andrea Perali. It was a pleasure to see Andrea here in Boulder and collaborating with him on the pseudogap work has been very helpful and has led to many interesting results.

I really have to thank all the people at JILA, NIST, and CU that help create what is probably the world's most concentrated center of knowledge in atomic physics and experimental techniques. I especially acknowledge help from Eric Cornell, Jun Ye, and the JILA electronics and machine shops. I think the collaborative environment at JILA combined with the great expertise of the members is vitally important to all of the success we have here and I can only hope to find a similar environment in my future work.

Finally, I would like to thank Katie. Thanks for all of your support, and for lifting my spirits, and making me happy. The last few years of my life here with you in Boulder have been amazing,

and I'm so happy we will be staying here together.

Contents

Chapter

1 Introduction 1

2 Creating a strongly interacting quantum degenerate atomic Fermi gas with a tabletop experiment 8

2.1 What is a quantum degenerate Fermi gas? 8

2.1.1 A harmonically trapped Fermi gas 12

2.2 Cooling an atomic gas 13

2.2.1 Measuring temperature 15

3 Feshbach resonances 18

3.1 Interactions in an ultracold atomic gas 18

3.2 Wide vs narrow resonances and universality 22

3.3 Measurement of molecule binding energies and resonance centers 25

3.3.1 Determination of s-wave Feshbach resonance parameters with rf molecule dissociation 25

3.3.2 Determination of p-wave molecule binding energies with magneto-association 29

3.4 Measurement of molecule lifetimes 34

3.5 Creating p-wave molecules near the Feshbach resonance 38

3.6 p-wave superfluids 41

4 Fermi superfluids and the BCS-BEC crossover 44

4.1 The pairing theory of Fermi superfluidity (BCS Theory) 44

4.1.1 Cooper pairs 44

4.1.2 Properties of the superfluid state 46

4.2 Turning up interactions: The BCS-BEC crossover 51

5 Fermi liquids, spectral functions, and photoemission spectroscopy 57

5.1 Landau's Fermi liquid theory 57

5.2 Green's function and many-body quantum theory 62

5.3 Photoemission spectroscopy 64

5.4 Photoemission spectroscopy experiments with a strongly interacting Fermi gas . . . 71

5.5 Improvements to the signal-to-noise ratio 75

6 The Pseudogap state of a strongly interacting Fermi gas 81

6.1 The pseudogap phase in the BCS-BEC crossover 81

6.2 (Some) History of the pseudogap phase and relation to high temperature superconductors 85

6.3 Atom photoemission spectroscopy and the pseudogap phase in the BCS-BEC crossover 88

6.4 Pseudogap to molecular gas crossover 101

6.5 Comparisons to a theory of the pseudogap 106

6.6 Extracting information from BCS-fits to the spectral functions 111

6.7 Conclusions 115

7 Towards atom-photoemission spectroscopy of a homogeneous gas 117

7.1 Focusing on the center of the cloud 118

7.1.1 Optical pumping 120

7.2 Application to a weakly interacting Fermi gas 123

7.3 Studying the effect of the trapping potential on atom-photoemission spectroscopy . . 128

8 Universal relations and the contact 137

8.1 The contact . . . 137

8.2 Measuring the contact . . . 140

8.3 Testing the Tan relations . . . 144

9 Conclusion and Outlook 151

9.1 Summary . . . 151

9.2 Outlook . . . 152

Bibliography 155

Appendix

A ^{40}K Transitions 163

B Subtracting the high-momentum background signal from optical pumping 168

C Accounting for interactions with the third spin-state in measurements of the contact 171

D Simulating photoemission spectroscopy of molecules 174

Chapter 1

Introduction

The realization of Bose Einstein condensation in 1995 was a crowning achievement, marking a major shift and a new direction for the field atomic physics [23, 24, 25]. To understand the significance of this shift, we can briefly examine the history of atomic physics. Modern atomic physics started at the beginning of the 20^{th} century with, as the name implies, an effort to understand the mechanics of an atom, the basic building block of all materials. It was at this time that the failure of classical physics to explain the stability of the atom led to the revolutionary development of quantum mechanics, and a golden age for atomic physics that spanned the 1910s and 1920s. The new theory of quantum mechanics led to such rapid progress that, beginning with Planck in 1918, twelve of the next fifteen Nobel prizes were awarded for work in atomic physics. However, at this point, the wild success of atomic physics became its downfall as physicists took the new theoretical concepts developed to understand atoms and used them to begin the fields of nuclear and particle physics, condensed matter and astrophysics. Indeed from 1933 to 1996, there were only nine more Nobel prizes awarded in fields of traditional atomic physics. However, this drought doesn't tell the story of a major change that was slowly taking place in atomic physics, which was moving away from developing theories of the mechanics of an atom, and towards controlling and using atoms as ideal quantum systems. Much of this progress was enabled by the invention of the laser in 1960, which gave scientists the ability to coherently and precisely control the quantum states of atoms. Developments in the 1980s to control and entangle the quantum states of atoms and photons would lead to dramatic demonstrations of non-locality in quantum mechanics, and

eventually the field of quantum information, which seeks to use precise control of quantum states to perform computation. At the same time in the 1980s, there were ongoing developments in the use of lasers to control the motion of atoms, including the demonstration of how to slow atoms, and achieve laser cooling of atomic gases. This eventually led to the achievement of Bose-Einstein condensation of atomic gases in the miraculous summer for atomic physics of 1995.

Bose-Einstein condensation (BEC) is a phase transition to a new state of matter where all of the particles in the system occupy the same quantum state. It can occur only at very low temperatures or high densities, regimes where the quantum nature of the individual atoms in the gas cannot be ignored. In the dilute alkali gas experiments that reached BEC in 1995, the atoms were cooled to nanoKelvin temperatures, which is (as far as we know) the coldest temperatures ever reached in the universe. This dramatic achievement led to an explosion in the new field of ultracold atomic gases, with publication rates increasing exponentially to nearly a thousand academic papers a year by 2000 [26]. Nobel prizes have been awarded in 1997, 2001, and 2005 in atomic physics with surely many more to come to recognize this new and exciting research field.

But beyond the "wow" factor of these ultracold gases, exactly what has attracted so much attention? While ultracold gases have enabled new progress in precision measurement, leading to ultra-precise interferometers and atomic clocks, much of the interest comes from the potential to use cold atomic gases as models to test fundamental theories of quantum matter. Indeed, the work presented in this thesis regards the use of ultracold gases to test fundamental theories of strongly interacting fermions. It is because of our ability to control and study these systems at the quantum level, using the tools of atomic physics, that they are so useful in modeling and studying quantum matter. Over the last 15 years, this high level of control has allowed experiments with quantum gases to realize physics previously believed to only exist as textbook or gedanken (thought) experiments. Indeed, until 1995 a weakly interacting Bose-Einstein condensate was widely assumed to be a gedanken experiment, with no relevance to any physically realizable system. Yet, if all we could do with atomic gases is realize experiments for which we already understand the physics, this would be a shallow field. Fortunately, the development of Feshbach resonances and optical

lattices to control atomic interactions and create strongly correlated gases means that we can use ultracold atomic gases to investigate some of the most pressing scientific issues to date, such as high temperature superconductivity and quantum phase transitions. Indeed, developing theories to understand strongly correlated systems is a central challenge in nearly all modern fields of physics including nuclear physics, astrophysics, and condensed matter. The great importance of developing theories of strongly correlated systems, and the high level of precision and control afforded by ultracold gases to study these regimes is what motivates the work in this thesis.

Phillip Anderson laid out the basic premise for why we study large and complicated systems like materials or quantum gases in his oft cited paper "More is different [27]". He writes that even if "the elementary entities of science X obey the laws of science Y ... this hierarchy does not imply that science X is "just applied Y." At each stage entirely new laws, concepts, and generalizations are necessary, requiring inspiration and creativity to just as great a degree as the previous one. Psychology is not applied biology, nor is biology applied chemistry." In other words, if we take some atoms, which we understand perfectly well on an individual basis, but then let them interact with each other to form a larger system, we may know little to nothing of use about the behavior of that system based only on our understanding of those individual atoms. Instead, we must develop new laws and concepts to understand this larger and more complicated system. In the extreme case, this is quite obvious, our knowledge of the quantum mechanics of atoms does not imply we now have all the basic tools to understand life, despite the fact that life is actually made of a bunch of atoms obeying the laws of quantum mechanics. Amazingly, it turns out that systems of multiple atoms become complicated so fast that simply trying to solve the basic equations of quantum mechanics becomes impossible even for only a few tens of atoms, even with the worlds most powerful supercomputers. This is why we need to develop new ways of understanding these systems. At a simplified level, one can divide physics into fields that are still trying to develop a more fundamental understanding of the basic constituents of matter and energy in the universe, such as fields like high energy particle physics, and fields that are tackling systems for which we understand the properties of the basic constituents but are unable to formulate complete theories

of the whole. Our study of ultracold atomic gases falls into the latter category.

So far, physicists have been quite successful at explaining large systems of particles if those particles are weakly interacting. This is because the behavior of the system as whole may not deviate that far from what would be expected of a single particle, but occurring many times over in each of the particles constituting the system. Thus, as a first approximation, one can simply try to describe large systems by ignoring the presence of interactions. The next level of approximation, mean-field theory, is to take into account the average interaction between particles, but ignore fluctuations around the average. The electrons in most metals and semiconductors, as well as weakly interacting ultracold atomic gases, are good examples of systems that can be largely understood in terms of mean-field theory. However, a separate class of systems exist where the constituent particles are strongly interacting with each other and deviations from mean-field theory are important. It is in these systems that we should expect new behaviors and properties to emerge. In materials, some examples of strongly correlated systems are high-temperature superconductors, heavy-fermion materials, giant magneto-resistors, Mott insulators, and materials near quantum phase transitions [28]. Many of these materials have significant potential applications, such as high-temperature superconductors that could be used for efficient transport of electricity. Developing theories to understand strongly correlated materials could unlock new and important technologies.

While ultracold atomic gases and strongly correlated electron materials may be worlds apart in many ways, including their density (dense solids vs dilute gases) and temperatures (Kelvin vs nanoKelvin), their behaviors are underpinned by many of the same theoretical concepts of strongly interacting quantum systems. The connections to certain strongly interacting systems is especially strong. Indeed, when the short-range atomic interactions are increased to their maximum strength using a Feshbach resonance, the system enters a universal regime where its properties no longer depend on the details of the atomic species or interactions[29, 30]. Any other strongly correlated system with short-range interactions in this universal regime will behave identically, after a simple rescaling of the parameters depending on the density. It is thought that dense nuclear matter may in fact be in this same regime, displaying identical behavior to an ultracold atomic gas [31, 32].

The real interest in studying ultracold atomic gases to learn about strongly interacting systems comes from the fact that the control and detailed information experimenters have with atomic systems is so great. Ultracold atomic gases allow the experimenter to start with a simple system, like a gas of weakly interacting particles, and incrementally add complexity by, for example, turning up interactions with a Feshbach resonance, adding a periodic potential, or adding disorder. This ability to start from what you understand and slowly go towards something you don't understand is far more difficult to achieve in materials, where the system often has many inseparable and complicated interactions going on at once. Furthermore, atomic gases offer experimenters many new measurement techniques that are not available in other systems. For example, a common measurement in atomic gases is to measure the momentum distribution of the constituent particles, which is something far more difficult to achieve for electrons in materials. Almost always in physics, the ability to make new kinds of measurements drives the development of theories and leads to advances in basic understanding. Atomic gases thus offer the opportunity to develop a ground-up understanding of strongly interacting systems, which can ultimately impact our ability to understand other complicated systems, whether in condensed matter, nuclear, or astrophysics.

A central challenge in realizing the great promise of ultracold atomic gases is to develop experimental measurements that can directly connect to the theories of strongly interacting systems and enable sensitive searches for new phenomena. In this thesis, I will discuss a new measurement technique for strongly interacting atomic gases that I helped to develop. This technique is called atom photoemission spectroscopy, and it has allowed us to make a number of important measurements of fundamental properties of strongly interacting Fermi gases. We have used this technique to address the existence of a pseudogap state in the BCS-BEC crossover, as well as verify a number of recently derived universal relations known as the Tan relations. In the next section, I will give a more detailed outline of the contents of this thesis.

Outline of Thesis Contents

Much of my graduate career was alongside John (Jayson) Stewart who wrote a Ph.D. thesis in 2009 and, underlying my organization of this thesis, is a competing desire to give both a complete

description of the work I have done with adequate background information, while not repeating too much of what is already contained in Jayson's thesis. Furthermore, background information on the experimental apparatus is contained in Brian Demarco's thesis, and Cindy Regal's thesis contains excellent introductions to Feshbach resonances and the BCS-BEC crossover. As such I will be brief in my discussions of those topics and refer the reader to appropriate sources.

In the second chapter, I introduce and review basic concepts for quantum degenerate Fermi gases. I also give a brief description of the experimental apparatus, explaining how we cool an atomic ^{40}K gas to ultracold temperatures and make measurements.

In the third chapter, I explain how we realize a strongly interacting Fermi gas using a magnetically tunable Feshbach resonance. I discuss the physics of Feshbach resonances in atomic gases including the concepts of narrow versus wide resonances and s-wave versus p-wave resonances. While most of the work in this thesis regards s-wave resonances, we conducted some experiments using a p-wave Feshbach resonance in order to explore the possibility of creating a p-wave superfluid. I discuss the results of these experiments, which include forming p-wave pairs and observing their lifetimes and non-isotropic momentum distributions. I also review some prospects for further research of atomic gases with p-wave interactions.

In the fourth chapter, I review the results of conventional BCS theory, which describes how fermions pair up to form a superfluid or superconductor in the presence of weak attractive interactions. I then discuss what happens as the strength of interactions is increased to the limit of the BCS-BEC crossover and, eventually, molecular pairing. The BCS-BEC crossover occurs as the attractive interaction between fermions is increased to the limit where the typical pair size is on order of the interparticle spacing, and thus too strongly interacting to be described by BCS theory, but not yet to the deeply-bound molecular limit where the fermionic properties of the constituents play no role. It is in this crossover that the gas is the most strongly correlated, and therefore where the most interesting physics takes place. I review past experiments in the BCS-BEC crossover and discuss some of the goals of ongoing work.

In the fifth chapter, I begin with a review of the concepts of Fermi-liquid theory and spectral

functions, which serve as a language for discussing and understanding interacting Fermi gases. I then present the technique of atom photoemission spectroscopy to measure the spectral function. Atom photoemission spectroscopy measures the single-particle spectral function and is analogous to angle resolved photoemission spectroscopy (ARPES) in materials. I present our first atom photoemission spectroscopy measurements in the BCS-BEC crossover. Finally, I explain how we have improved on the techniques presented in that paper to significantly increase the signal-to-noise ratio of the data.

In the sixth chapter, I discuss the idea of a pseudogap state in the BCS-BEC crossover. This is a state in which the Fermi gas contains incoherent pairs of fermions existing at temperatures above the superfluid phase transition. Then, I present our atom photoemission data that searches for evidence of this state by looking at the properties of the single-particle spectral function above and below the superfluid phase transition. Indeed, we observe a spectral function that demonstrates backbending both above and below the superfluid transition, consistent with the predictions of a pseudogap state. I also present data that maps out the pseudogap regime as a function of interaction strength and shows how the pseudogap state evolves into the molecular regime where the physics is described by deeply bound molecules. Finally, I show comparisons to a theory of the pseudogap state that captures many essential elements of the data.

In the seventh chapter, I present a new technique for measuring the momentum distribution of atoms at the center of a trapped gas using intersecting hollow light beams. This technique allows us to obtain atom photoemission spectroscopy signal from the center of the atom cloud and thereby reduce some of the effects of density inhomogeneity. This allows us to better understand the effect of the trapping potential on our atom photoemission experiments.

In the eighth chapter, I discuss experiments to verify the universal Tan relations for quantum gases with short range interactions. These relations predict connections between numerous measurable quantities in ultracold gases. We take advantage of multiple measurement techniques, including atom photoemission spectroscopy, to verify these powerful relations.

In the end, I present a summary of results and a brief outlook for future research.

Chapter 2

Creating a strongly interacting quantum degenerate atomic Fermi gas with a tabletop experiment

2.1 What is a quantum degenerate Fermi gas?

In quantum mechanics all identical particles must be considered to be completely indistinguishable from each other, which implies important restrictions on the behavior of systems of identical particles. All particles can be classified as following one of two sets of quantum mechanical rules, Fermi-Dirac statistics or Bose statistics, and the corresponding particles are called fermions and bosons respectively. Whether a particle is a fermion or boson is determined by a quantum mechanical phenomena called spin, which can take on any integer or half integer value (anything else is called an anyon). Particles with either no spin or integer values of spin are bosons, while particles with half integer values of spin are fermions. The basic building blocs of matter, electrons, protons, and neutrons, are all spin $\frac{1}{2}$ particles and thus fermions. However, atoms are made up of many of those particles and can be either bosons or fermions depending on whether they have an even (bosons) or odd (fermions) number of constituents. An important result of Fermi statistics is that no two identical fermions can occupy the same quantum state; this is referred to as the Pauli exclusion principle. This arises from the requirement that the many-particle wave-function describing a system of identical fermions must be antisymmetric under the exchange of any two of those particles.

Let's consider the case of two non-interacting identical fermions. To begin with, let's take two fermions with no internal degree of freedom so that they are completely described by their position-

space wave-functions. We will assume there is a ground state wave-function $\psi_0(r)$ and a first excited state $\psi_1(r)$. Intuitively, one would think that the lowest energy state for the two fermions would be $\psi(r_1, r_2) = \psi_0(r_1)\psi_0(r_2)$ where r_1 (r_2) is the coordinate for particle 1 (2). This wave-function puts both fermions in the ground state. However, this wave-function is symmetric under the exchange of particles 1 and 2, in other words $\psi(r_1, r_2) = \psi(r_2, r_1)$, which is not allowed for fermions. The lowest energy wave-function that obeys the antisymmetry principal, $\psi(r_1, r_2) = -\psi(r_2, r_1)$, is $\psi(r_1, r_2) = \frac{1}{\sqrt{2}}\psi_0(r_1)\psi_1(r_2) - \frac{1}{\sqrt{2}}\psi_1(r_1)\psi_0(r_2)$. This wave-function has one particle in the ground state and one particle in the first excited state. Thus, by restricting the two-particle wave-function to be antisymmetric, the ground state energy is raised because we are forced to put one particle in an excited state. Note that the two fermions can never be found at the same location since $\psi(r_1 = r_2) = 0$.

Now, let's consider a case where the fermions also have an internal degree of freedom, which may be spin in the case of an electron or internal atomic state in the case of an atom. We will consider the simple case where there are two degenerate internal states, labeled up $|\uparrow\rangle$, and down $|\downarrow\rangle$. The spin wave-function of the two identical fermions can be in one of four states: the spin triplet states $|\uparrow\rangle_1|\uparrow\rangle_2$, $\frac{1}{\sqrt{2}}\Big(|\uparrow\rangle_1|\downarrow\rangle_2 + |\downarrow\rangle_1|\uparrow\rangle_2\Big)$, $|\downarrow\rangle_1|\downarrow\rangle_2$, and the spin singlet state $\frac{1}{\sqrt{2}}\Big(|\uparrow\rangle_1|\downarrow\rangle_2 - |\downarrow\rangle_1|\uparrow\rangle_2\Big)$. The spin triplet states are all symmetric under exchange of particle 1 and 2, whereas the spin singlet state is antisymmetric under exchange of particles. Since the overall wave-function for the two fermions must be antisymmetric, if the fermions are in a spin triplet state, their position space wave-function must be antisymmetric just as in the case where we had no internal degree of freedom, but if they are in the spin singlet state, then their position space wave-function must be symmetric. Thus, the lowest energy state is now $\psi(r_1, r_2) = \frac{1}{\sqrt{2}}\psi_0(r_1)\psi_0(r_2)\Big(|\uparrow\rangle_1|\downarrow\rangle_2 - |\downarrow\rangle_1|\uparrow\rangle_2\Big)$, which has one spin up particle and one spin down particle, both in the ground position-space state. In this way, even if the internal degree of freedom is not explicitly contained in the Hamiltonian, it can affect the energy of the system by determining which wave-functions are allowed.

If there are many fermions, the antisymmetry principal says that the overall wave-function must be antisymmetric under exchange of any two fermions. Again assuming two degenerate

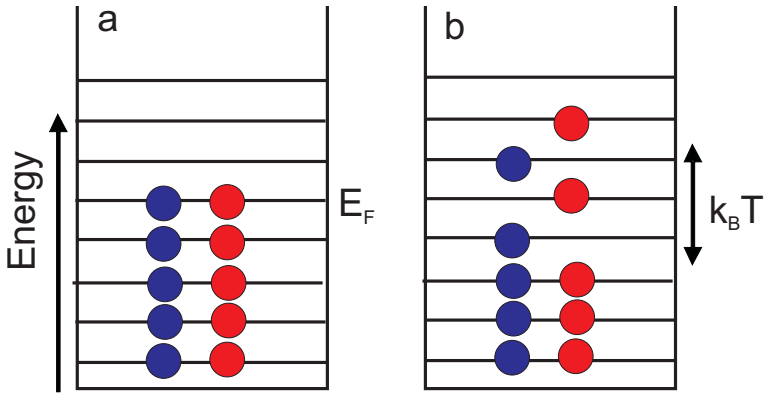

Figure 2.1: **Fermions in a square well** The quantized motional states are shown as horizontal lines with the ground state at the bottom and energy increasing upwards. Blue circles are spin up fermions and red circles are spin down fermions. a) The ground state of the fermion system has a fermion of each spin into each motional level, filling up all the quantum states until there are no more fermions. The energy of the highest occupied level is the Fermi energy. b) Finite temperature causes excitation of fermions above the Fermi energy by energies of order $k_B T$.

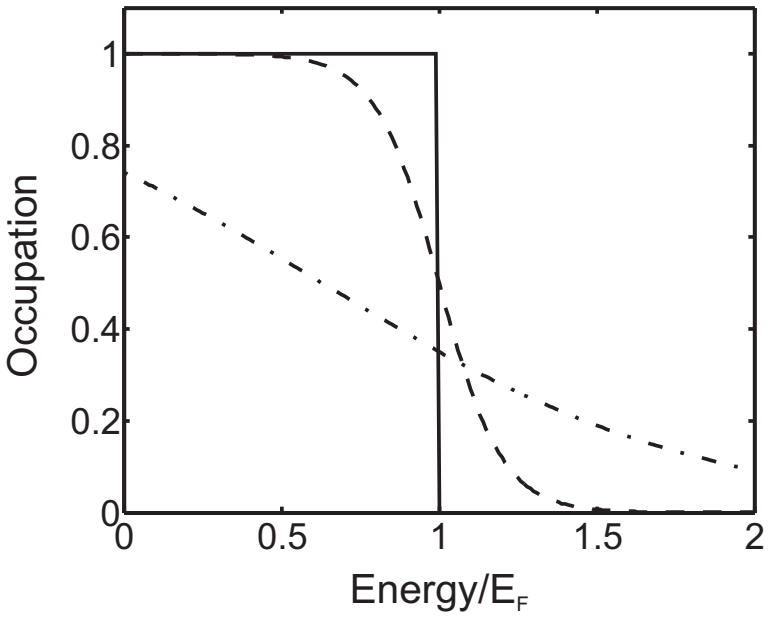

Figure 2.2: **The fermion distribution function** The average occupation number of quantum states for fermions of a single spin state are plotted as a function of the energy of the state for different temperatures. Reduced temperatures of $T/T_F = 0, 0.1$,and 0.6 are shown as solid, dashed, and dot-dashed lines. At zero temperature (solid line), the occupation is 1 for all states below the Fermi energy and 0 for all states above. At $T/T_F = 0.1$ (dashed line) the Fermi surface is broadened by roughly $0.1E_F$. At $T/T_F = 0.6$ (dot-dashed) there is no recognizable Fermi surface and the distribution approaches the classical limit of an exponential.

internal states, the ground state wave-function will have one fermion of each spin in the ground position-space state, one of each spin in the first excited state, and so on with two particles in each state until there are no more particles, as shown in Fig. 2.1 a. The energy of the highest occupied state is called the Fermi energy, denoted E_F. If we take the example of a 3-d square well potential, the states are labeled by their momentum $\hbar k$ and the density of states in k-space, $\rho(k)$, is given by $\rho(k)dk = \frac{V}{2\pi^2}k^2dk$, where V is the volume of the system. The total number of fermions is $N = 2\int_0^{k_F} \frac{V}{2\pi^2}k^2dk$. Here the factor of two is because we can put one fermion of each internal state in each k state, and k_F is the Fermi wave vector, which is the value of k that corresponds to the highest occupied state, and is given by $k_F = \frac{\sqrt{2mE_F}}{\hbar}$, where m is the fermion mass and $\hbar = \frac{h}{2\pi}$, where h is Plank's constant. This gives

$$k_F = (3\pi^2 n)^{1/3} \tag{2.1}$$

and correspondingly

$$E_F = \frac{\hbar^2}{2m}(3\pi^2 n)^{2/3} \tag{2.2}$$

where $n = N/V$ is the total fermion density.

At finite temperature there will be excitations above this ground state, with some particles near the Fermi surface being excited to states above it, as shown in Fig 2.1 b. A system at temperature T will have excitations going up above the Fermi energy by an extra energy on order of k_BT where k_B is the Boltzmann constant, Fig. 2.1. We can define a unitless reduced temperature of the system as T/T_F where T_F is the Fermi temperature corresponding to E_F/k_B. A gas at $T/T_F \ll 1$ will have a particle distribution that looks mostly like the ground-state particle distribution, but with a smearing around the Fermi surface of width k_BT, see Fig. 2.2. A Fermi gas at $\frac{T}{T_F} \ll 1$ is called a quantum degenerate Fermi gas and is strongly affected by quantum statistics. As T/T_F is increased, the smearing will grow larger and larger until at $T/T_F \gg 1$ the particle occupation will drop to much less than one per state, and the gas will essentially behave as a classical gas. The particle distribution for a finite temperature Fermi gas is given by the Fermi-Dirac distribution

function

$$f(E) = \frac{1}{e^{\frac{E}{k_b T}}/\zeta + 1} \tag{2.3}$$

where $\zeta = e^{\mu/k_b T}$ is called the fugacity and μ is the chemical potential, which is approximately E_F for a weakly interacting low-temperature Fermi gas.

Let's consider an example. The valence electrons inside a metal can be considered to be a weakly-interacting Fermi gas. If we take copper, which has a density of 9 grams/cm^3, an atomic mass of 63.5 and one valence electron, we get an electron density of 8.4×10^{28} m^{-3}. Using the electron mass, this gives $T_F = 81,000$ K. Thus, even at room temperature, copper has a reduced temperature of approximately $T/T_F = 0.004$, which is far into the quantum degenerate regime. This thesis is about dilute atomic Fermi gases made up of potassium-40 (^{40}K) atoms. A typical atomic density in the gas is 10^{19} m^{-3} which gives $T_F = 270$ nK, a full twelve orders of magnitude lower than for electrons in copper. Thus, to study a degenerate atomic Fermi gas in this regime, we will need to cool our atomic vapor to nano-Kelvin temperatures.

2.1.1 A harmonically trapped Fermi gas

Eqs. 2.2 and 2.1 give the Fermi energy and Fermi momentum for a homogenous Fermi gas, however, in ultracold atom experiments the gas is typically confined by a harmonic potential, which alters the density of states. For a cylindrically symmetric trap, parameterized by a radial trap frequency $\omega_r = 2\pi f_r$ and an axial trap frequency $\omega_z = 2\pi f_z$, which gives a trap aspect ratio of $\lambda = \omega_z/\omega_r$, the density of states becomes $\rho(E) = \frac{E^2}{2\lambda(\hbar\omega_r)^3}$. The Fermi energy is then

$$E_F = \hbar\omega_r(6\lambda N)^{1/3} \tag{2.4}$$

where N is the number of atoms in a single spin-state. A corresponding Fermi momentum can be defined as $k_F = \sqrt{2mE_F}/\hbar$. A typical confinement trap has $\omega_r = 2\pi \times 250$ Hz and $\lambda = 0.1$, which gives $E_F = h \times 10$ kHz or $T_F = 450$ nK for $N = 10^5$ atoms.

The equation for the Fermi energy of a homogenous gas and a trapped gas can be linked by noting that the Fermi energy obtained by plugging the peak density of an ideal, harmonically

trapped gas at zero temperature into Eq. 2.2 gives the same Fermi energy as Eq. 2.4. In fact, one way to think about a trapped gas is using local density approximation (LDA), which says that each concentric shell of constant density n in the gas can be thought of as a homogenous system, with a local Fermi energy given by Eq. 2.2. Any quantity for the trapped gas can be obtained by calculating the same quantity for a homogenous gas with density ranging from $n = 0$ to $n = n_0$, where n_0 is the peak density of the trapped gas, and then performing a density weighted average of that quantity using the density profile of the trapped gas.

In the rest of this thesis, the Fermi energy will typically refer to Eq. 2.4; however, at times we will also use Eqs. 2.2 and 2.1, and I will try to clearly specify when this is the case.

2.2 Cooling an atomic gas

The experimental techniques we use to create ultracold ^{40}K gases are now more than a decade old, and they vary little from the techniques presented in the original BEC papers of 1995, with the exception of the final stage of evaporation being done in a far-detuned optical trap (FORT), and that two spin states are now occupied during the evaporation. I will provide a brief description of the experimental apparatus below; for a more detailed presentation I would recommend Brian Demarco's thesis [33] for everything concerning the MOT and magnetic trap, and Cindy Regal's [6] and Jayson Stewart's thesis [34] for the optical trap.

The first stage of cooling is laser cooling in a magneto-optical trap (MOT). A MOT uses counterpropagating laser beams on three orthogonal axes as well as a quadruple magnetic field to slow down and trap atoms using the radiation pressure of light. With the MOT we are able to create a ^{40}K gas of a few 10^9 atoms cooled to a few hundred mK. The second stage of cooling involves trapping two spin states of ^{40}K in a cloverleaf magnetic trap and performing microwave evaporation to selectively remove atoms with the highest energy. In the ground state, ^{40}K is a spin 9/2 atom, and the spin states we use for evaporation are the $|f, m_f\rangle = |9/2, 9/2\rangle$ and $|9/2, 7/2\rangle$ states, where f is the total atomic spin and m_f is the projection along the magnetic-field axis. After evaporating for approximately 45 s in the magnetic trap, we typically achieve conditions of 25×10^7

atoms at 7 μK. At this point the gas has a reduced temperature close to $T/T_F = 3$. For the final stage of evaporation, we use a crossed-beam FORT with lasers near 1070 nm, which is far enough detuned from the atomic transitions near 770 nm that resonant scattering is essentially negligible. A FORT works through the AC atomic Stark shift, and for red detuned lasers, the Stark shift will always be negative. Thus, a focused laser beam creates a trapping potential because atoms will be attracted to the high intensity at the focus. The laser beam creates a gaussian confinement potential for the atoms, which can be approximated as harmonic near the center. We use a FORT consisting of two crossed beams to achieve a higher axial trap frequency and thus a lower trap aspect ratio. Forced evaporation in a FORT is achieved by slowly lowering the laser beam intensity to allow the highest energy atoms to fall out of the trap. After about 10 s of evaporation in the FORT, we reach a degenerate Fermi gas with 2×10^5 atoms at or just below $T/T_F = 0.1$.

For the evaporation stages in both the magnetic trap and the FORT, it is important to have two spin states of ^{40}K occupied in order to have collisions, and thus allow rethermalization of the gas as high energy atoms are removed. In scattering theory, collisions can be understood using partial-wave analysis on the two-particle wave functions. The wave-function of the two colliding particles can be broken into angular and radial parts, with the angular part being described by the spherical harmonics. An $l = 0$, or s-wave collision, involves two atoms interacting with a wave-function in the lowest spherical harmonic, while an $l = 1$, or p-wave collision, has atoms interacting in the first spherical harmonic. For $l > 0$, the collisions involve angular momenta and there is a centrifugal barrier that can prevent the atoms from getting close, and this reduces their chances of colliding. For interacting atoms with kinetic energy greater than the height of the centrifugal barrier, this is not an impediment to colliding; however, for kinetic energies lower than the barrier height, the centrifugal barrier suppresses scattering. This is known as the Wigner threshold law. As the temperature of a gas is reduced, the average collision energy decreases, and below a certain temperature collisions with $l > 0$ will be "frozen out" (except in the case of a $l \neq 0$ scattering resonance as described in the next chapter). For ^{40}K, the barrier height or threshold for p-wave collisions is approximately 1 mK, and only s-wave collisions are energetically allowed

in the evaporation stages of the experiment [33]. However, fermions in a single spin state cannot interact via an s-wave channel due to the antisymmetry principal, as discussed above, and thus it is important to occupy at least two spin states to allow collisions in the gas to take place.

The experimental apparatus consists of two glass cells connected by a meter long tube. Each cell has a MOT. The collection cell contains potassium getters, enriched for ^{40}K, for a source. The getters are small samples of potassium-chloride salt and calcium that emit potassium vapor when heated by running current through them. We can control the background vapor pressure of potassium in the collection cell by changing the current we are running through getter. However, the background pressure in the collection cell is too large for efficient evaporation because a typical atom will be hit by a high-energy background atom once every second or so. This is why we have a second cell, that we call the science cell, for evaporation where the typical time for a collision with a background atom is approximately 100s. We move atoms from the collection cell MOT to a second MOT in the science cell with a "push beam."

The bias coils used for the magnetic trap in the science cell can also be used to create a bias magnetic-field for atoms trapped in the FORT. We can create fields up to 250 G. In order to increase interactions in the gas, we take advantage of a Feshbach resonance near 200 G that can increase collisions in the gas by orders of magnitude. This both allows the evaporation in the FORT to be more efficient, by decreasing the rethermalization time scale, and also allows us to create a strongly interacting Fermi gas at the end of the evaporation. I will explain Feshbach resonances in detail in the next chapter, including the physics behind them as well as some experiments to measure them and use them to create diatomic molecules.

2.2.1 Measuring temperature

You might be wondering: How do we measure the temperature of a dilute microscopic gas that is only a few nano-Kelvin? There are rather significant challenges: the gas has a size of just a few tens of microns, it exists in an ultrahigh vacuum, it is a million times more dilute than air, it will only scatter light that is precisely tuned to the atomic transition, and it is the coldest thing

in the universe (assuming intelligent life somewhere else in the universe haven't created something even colder without us knowing); hwoever, it turns out it is not that difficult to measure the temperature. First, we already have lasers precisely tuned to the atomic transition that we use to make the MOT. Also, even though the gas is dilute compared to air, the trapped cloud can be very optically dense for resonant light and absorb more than 99% of light that travels through it. This allows us to take a picture of the cloud, using lenses to magnify and focus the image onto a low noise CCD camera. Specifically, the atom gas absorbs photons and scatters them to create a shadow image. By taking a second image of the light without any atoms present, we can determine how many photons were absorbed at each position and back out the column density of the atoms. One minor problem is that when the atoms absorb and scatter photons during an image acquisition, they are heated. In fact, a single photon imparts an energy to an atom that is roughly equal to the average energy of an atom in the ultracold gas. To take a high quality image, we need to scatter hundreds of photons off of each atom, which easily imparts enough energy to the heat the gas out of the trap. Fortunately, we are able to scatter hundreds of photons off of each atom in just a few tens of microseconds such that they are essentially frozen in place during the picture. However, this means that after each picture we will need to prepare another ultracold Fermi gas from scratch in order to make another measurement.

There are two kinds of measurements we can make by taking a picture of an ultracold Fermi gas. The first is to take a picture of the cloud while it is being held in the confinement trap. This gives the density profile $n(r)$ of the trapped gas. Actually, it gives the projection of $n(r)$ onto a 2d surface. From this, the 3d density distribution can be extracted assuming symmetry and using an inverse Abel transform. One can compare the measured $n(r)$ to the theoretical prediction for a non-interacting Fermi gas held in a harmonic trapping potential and extract a temperature. In reality, this measurement turns out to be rather difficult with our apparatus due to the difficulty of measuring a very small and optically dense sample with our imaging system. A second kind of measurement is to take a picture after a time of flight (TOF). This involves quickly turning off the trapping potential, after which the atom cloud begins to fall due to gravity, as well as expand as the

gas flies apart. If the atom cloud is weakly interacting, we can assume the expansion is ballistic, or in other words, that no momentum changing collisions take place during the expansion. Once the cloud has expanded to much larger than its original size, the density distribution of the cloud will reflect the velocity distribution of the gas just before we turned the trap off. A typical expansion time is 10 ms. With a TOF measurement, we can compare the measured velocity distribution to the theoretically predicted velocity distribution for a harmonically trapped Fermi gas to extract a temperature.

For a non-degenerate Fermi gas, we can use classical thermodynamics, which predicts a gaussian distribution for the velocities, with the rms velocity $\sqrt{\langle v^2 \rangle}$ being related to temperature by the equipartition theorem as $\frac{1}{2}m\langle v^2 \rangle = \frac{3}{2}k_b T$. Once the gas is cooled below approximately $T/T_F = 0.6$ it becomes necessary to account for quantum effects and use Fermi-Dirac statistics to understand velocity distributions. Below $T/T_F = 0.1$, the velocity distribution approaches the zero temperature limit of a trapped Fermi gas and it becomes difficult to measure the temperature to high accuracy due to imaging resolution and a limited signal-to-noise ratio. The lowest temperature gases we have measured are $T/T_F = 0.07 \pm 0.01$.

For more detailed discussions of measuring the temperature of a trapped Fermi gas, I would recommend the discussions in the theses of Brian Demarco, Cindy Regal, and Jayson Stewart [33, 6, 34].

Chapter 3

Feshbach resonances

In this chapter, I will discuss how atoms in an ultracold gas interact with each other and, specifically, how these interactions can be tuned using a Feshbach resonance to make the system strongly interacting. Feshbach resonances can enhance scattering in any angular momentum channel, and I will discuss both experiments near an s-wave and near a p-wave Feshbach resonance. In particular, I will present a new measurement of the location of an s-wave Feshbach resonance for ^{40}K atoms as well as experiments creating and observing p-wave molecules near a p-wave Feshbach resonance. The theoretical discussion of Feshbach resonances follows largely from Ref. [35] although for the s-wave case similar treatments can be found elsewhere, for example Ref. [4]. Cindy Regal's thesis [6] is also a good reference for the particular case of ^{40}K Feshbach resonances. The experiments involving the p-wave Feshbach resonance were published in references [2, 3].

3.1 Interactions in an ultracold atomic gas

One of the great features of using ultracold atomic gases to study the physics of strongly interacting systems is that the interactions at the two-body level, between two isolated atoms, can be understood in a rather simple framework. This is due to the fact that we are usually in a situation where the dominant interaction, the Van der Waals interaction, which falls off as r^{-6} where r is the distance between atoms, is a short-range interaction and can be mapped onto a pseudopotential consisting of a delta-function interaction. The interaction can then be characterized by single parameter, a, the s-wave scattering length. This amounts to an approximation for scattering at low

energy with a short-range potential. Specifically, the s-wave scattering amplitude from a short-range potential can be expanded for low k as

$$f(k) = \frac{1}{\frac{-1}{a} + r_{\text{eff}}\frac{k^2}{2} - ik} \tag{3.1}$$

where $\hbar k$ is the collision momentum, and r_{eff} is the effective range of the potential [36, 35]. In the limit $ka \to 0$, the scattering amplitude asymptotes to a constant value, $-a$, which gives a scattering cross section $\sigma = 4\pi a^2$. For $ka \gg 1$ and $r_{\text{eff}}k \ll 1$, we find $f = i/k$ giving the unitarity limited cross section of $\sigma = \frac{4\pi}{k^2}$. In the limit where $r_{\text{eff}}k \ll 1$, the interaction can be modeled by a delta function pseudopotential and the atom-atom interaction energy becomes [35]

$$U(r) = \lambda\delta(r) \tag{3.2}$$

where λ is adjusted to produce the proper scattering length via

$$a = \frac{m}{4\pi\hbar^2}\frac{\lambda}{1 - \frac{\lambda}{\lambda_c}} \tag{3.3}$$

where m is the atom mass and λ_c is the critical value of λ where a bound state appears in the attractive delta-function potential ($\lambda_c < 0$) [35]. It can be seen that as $\lambda \to \lambda_c$ the scattering length diverges. It is in this limit of large scattering length where the many-body system becomes strongly interacting.

This delta function pseudopotential reproduces all of the essential physics of the more complicated atom-atom interaction [35] (note: it is important to impose a proper cutoff at large momenta for the delta function potential to obtain a non-zero scattering length [35]).

In principle, the scattering length a depends on the details of the full atom-atom potential, but in practice a is almost completely determined by the position of the single bound state closest to the threshold energy for two atoms scattering with zero collision energy (as in the case above for the delta function potential). If there is a bound state at an energy slightly below threshold, the scattering length is positive. If there is a bound state exactly at threshold, there will be a zero energy scattering resonance and $|a| \to \infty$. In a situation where there is no bound state below

threshold, but if the potential were to be made a little bit deeper one would appear, the scattering length is negative [36].

This picture gives an idea of how one could tune the scattering length and thus the strength of the pseudopotential. If the interatomic potential could be tweaked in such a way as to move the position of the last bound state around threshold then the scattering length, and thus the strength of the pseudopotential, could be tuned to any value. This is exactly how a magnetic-field Feshbach resonance works. It turns out that the position of the bound states relative to the threshold energy of the atoms can be tuned using the differential Zeeman energy shifts of the various spin channels[6, 35]. The magnetic-field strength, B_0, where a new bound state appears at threshold corresponds to the peak of a Feshbach resonance, and near B_0 the scattering length tunes with the magnetic field strength B as [4, 6]

$$a = a_{bg}(1 - \frac{w}{B - B_0}) \tag{3.4}$$

where a_{bg} is the background scattering length, w is the width of the resonance, and B_0 is the center position of the Feshbach resonance, see Fig. 3.1. Feshbach resonances are an amazing tool for studying strongly interacting quantum gases because they allow us to tune the scattering length to any value simply by varying the strength of an applied external magnetic field.

The bound state that is brought into resonance can be either an s-wave (ground-state rotational) or p-wave (1st excited rotational) molecular state and the corresponding scattering resonance then occurs in the s-wave or p-wave collision channel. Away from any scattering resonance, the low collision energies in ultracold gases mean that p-wave scattering is usually "frozen out" in accordance with the Wigner threshold law. However, in the presence of a p-wave scattering resonance, a spin-polarized Fermi gas can be dominated by p-wave interactions. This raises the interesting possibility of creating a p-wave paired superfluid. Before we discuss this possibility further, it will be helpful to go over a few more concepts and basic measurements. In particular, an understanding of the concepts of broad and narrow resonances is essential.

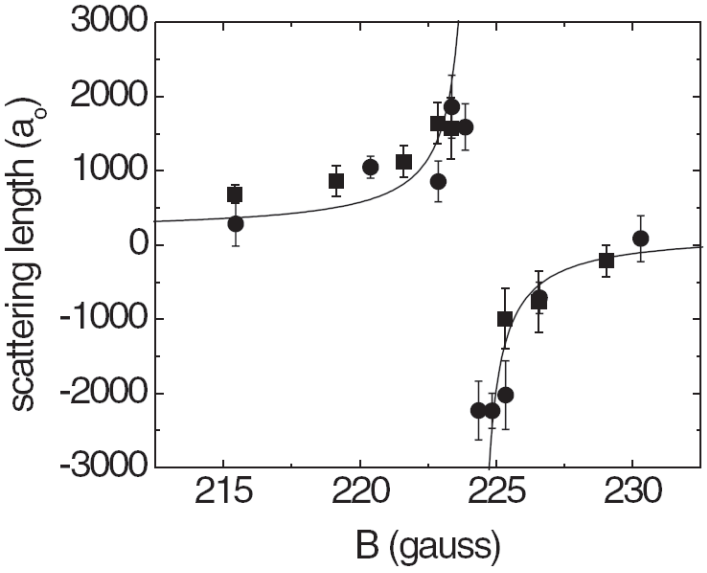

Figure 3.1: **A Feshbach resonance** The scattering length near an s-wave Feshbach resonance for ^{40}K atoms is plotted as a function of magnetic field. The solid lines are the theoretical prediction given by Eq. 3.4 where the parameters B_0 and w were adjusted to fit the data and a_{bg} was known from previous measurements. The data points (circles and squares) are measurements of the scattering length from rf spectroscopy of mean-field energy shifts. The data shows that the scattering length, and therefore the strength of the atom-atom interactions, can be tuned over a large range. It is important to note that one would not expect to be able to measure scattering lengths above a few thousand Bohr radii (a_0) in this experiment due to the unitarity limit. This figure is taken from Ref. [1]

.

3.2 Wide vs narrow resonances and universality

The situation I described in the last section, where the interactions can be parameterized by a single parameter, the scattering length a, and understood in terms of a delta function pseudopotential, is the situation of a universal or broad resonance [6, 35]. To understand what is meant by this, consider Eq. 3.1, which gives the scattering amplitude for s-wave collisions, and take $ka \to \infty$. In order for the scattering amplitude to be approximately what it would be in the case where $r_{\text{eff}} = 0$, we require $r_{\text{eff}} k \ll 1$ for all relevant k in the system [35]. We can see this by rewriting eq. 3.1 as $f(k) = \frac{i}{k}(1 + \frac{i}{2} r_{\text{eff}} k - \frac{i}{ka})^{-1}$. For a degenerate Fermi gas, this means we require $r_{\text{eff}} k_F \ll 1$, where k_F is the Fermi wavevector, for a "broad" or "universal" Feshbach resonance. The resonance is universal in the sense that the scattering only depends on the scattering length a, as opposed to a situation where higher order terms would need to be taken into account and interactions would depend on the details of the full atom-atom potential. It is "broad" in the sense that when $ka \to \infty$ all collisions in the gas are resonant; in other words, they all have the unitarity limited value for the scattering amplitude. An equivalent definition of a broad resonance is that the energy width of the resonance, given by $\Gamma = \frac{4\hbar^2}{m r_{\text{eff}}^2}$, be larger than the Fermi energy [35].

If a resonance is narrow, then only a small fraction of collisions in a band of energies of width Γ (or a band of momenta of width $\hbar / r_{\text{eff}}$) are resonant. The width of that band depends on r_{eff}, and therefore the physics is not universal. Interestingly, when the resonance is narrow the many-body problem can be treated perturbatively, even at the center of the resonance [35].

Studying the scattering problem in a two-channel model allows one to relate r_{eff} to the parameters of the Feshbach resonance, which is fundamentally a multi-channel scattering problem. It can be shown that

$$r_{\text{eff}} = -\frac{2\hbar^2}{m \mu_{co} a_{bg} w} \tag{3.5}$$

where μ_{co} is the difference in magnetic moment between the closed and open channels and is typically close to $2\mu_B$ where μ_B is the Bohr magneton [35, 4, 37]. For the ^{40}K resonance, near 202 G, we find $r_{\text{eff}} \approx -60 a_0$. Using a typical value of k_F we have $k_F r_{\text{eff}} \approx -0.03$, so the resonance is

well into the universal regime.

The discussion above centered on s-wave resonances, but it turns out that the situation for p-wave resonances is a bit different due to the existence of a centrifugal barrier. In particular, the long-range nature of the centrifugal barrier (the potential falls of as $\frac{1}{r^2}$) ensures that a quasi-bound resonance state with a well defined energy persists down to asymptotically low scattering energies. In contrast, for s-wave scattering resonances, a quasi-bound state only exists at high energies and is not accessed when one is in the limit of a broad resonance [35]. For p-wave scattering, the expansion for the scattering amplitude becomes

$$f_p(k) = \frac{k^2}{-\nu^{-1} + \frac{1}{2}k_0 k^2 - ik^3} \tag{3.6}$$

where ν, the scattering volume, is the p-wave analog of the scattering length and k_0 is the analog of the effective range [38, 35]. By expanding the scattering amplitude in the low energy limit it can be shown there is a resonance at energy $E \approx \frac{2\hbar^2}{m\nu k_0}$, which scales approximately linearly with magnetic field [2, 35], and has an energy width given by

$$\Gamma_p \approx \frac{4m^{1/2}E^{3/2}}{k_0\hbar}. \tag{3.7}$$

Unlike the energy width for a broad s-wave resonance, where there is no quasi-bound state and the resonance is at zero collision energy, the width of the p-wave resonance depends on a finite resonant scattering energy and scales as $E^{3/2}$. This means that as $E \to 0$, then $\frac{\Gamma_p}{E} \propto E^{1/2} \to 0$. In other words, in the low energy limit the p-wave resonance is always a narrow resonance. The physical reason for this is that the energy width Γ_p of the p-wave resonance can be thought of in terms of the inverse tunneling time into a quasi-bound state at energy E, which scales as $E^{3/2}$ [35] due to the centrifugal barrier (see Fig. 3.2). At low energies, the tunneling time becomes infinite and thus the energy width goes to zero.

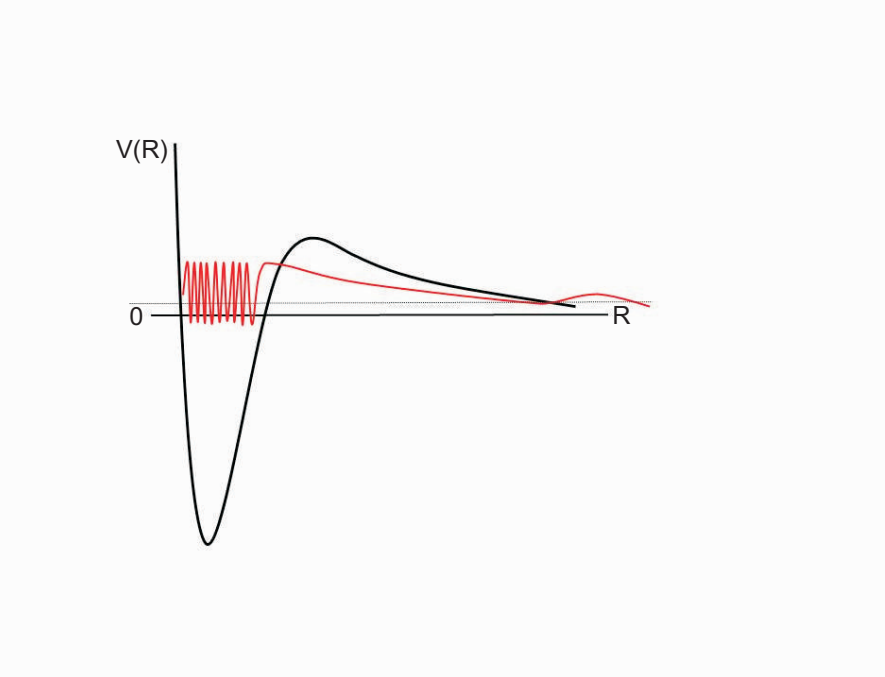

Figure 3.2: **Tunneling through a p-wave barrier** The schematic curve $V(R)$ shows the atom-atom potential with the p-wave centrifugal barrier equal to $\frac{\hbar^2}{mR^2}$ where R is the internuclear separation. The curve is not drawn to scale as the height of the barrier is $h \times 5.8$ MHz for ^{40}K atoms whereas the depth of the full potential is in the THz regime. The red line is a sketch of the wave function for a low energy quasi-bound state which oscillates quickly inside the potential, decays exponentially underneath the centrifugal barrier, and then oscillates slowly in free space at large R. For E much smaller than the barrier height, the tunneling time through the barrier scales as $E^{-3/2}$ where E is the scattering energy.

3.3 Measurement of molecule binding energies and resonance centers

In this section I describe measurements of the molecule binding energies near an s-wave resonance and near a p-wave Feshbach resonance. These binding energies can be used to determine Feshbach resonance parameters including the center of the resonance. While previous work in our group made determinations of the positions and widths of these resonances, the measurements I present here are more precise and also give some important insight into these resonances. The measurement of the p-wave molecule binding energies was published in Ref. [2].

3.3.1 Determination of s-wave Feshbach resonance parameters with rf molecule dissociation

One way to efficiently create Feshbach molecules is to adiabatically convert atom pairs into molecules by slowly ramping the magnetic field from above the resonance (where there is no bound state near threshold) to below the resonance where a bound state exists [39]. This method was first demonstrated in Ref. [39] for a resonance between the $|9/2, -9/2\rangle$ and $|9/2, -5/2\rangle$ states of ^{40}K near 220 G. The s-wave resonance we are interested for the purpose of this thesis is between the $|9/2, -9/2\rangle$ and $|9/2, -7/2\rangle$ states of ^{40}K and occurs near 202 G [6]. Here, we create molecules in an atom gas consisting of an equal mixture of atoms in the $|9/2, -9/2\rangle$ and $|9/2, -7/2\rangle$ states at $T/T_F = 0.1$ by ramping the magnetic field from 203.5 G to a value B below the resonance. The ramps are done at rates much slower than 40μs/G to be well within the adiabatic limit for creating molecules [39].

In order to measure the molecule binding energy, we perform rf spectroscopy on the gas. Specifically, we apply an rf field at a frequency near the energy splitting of the $|9/2, -7/2\rangle$ and $|9/2, -5/2\rangle$ states, which is approximately 47 MHz for fields near 200 G. Then, we selectively image any atoms in the $|9/2, -5/2\rangle$ state and record their number as a function of the rf frequency. To make sure the rf lineshape is unaffected by many-body effects, we first turn off the trapping potential and let the cloud expand for $5 - 15$ ms to lower the atom density before applying the rf

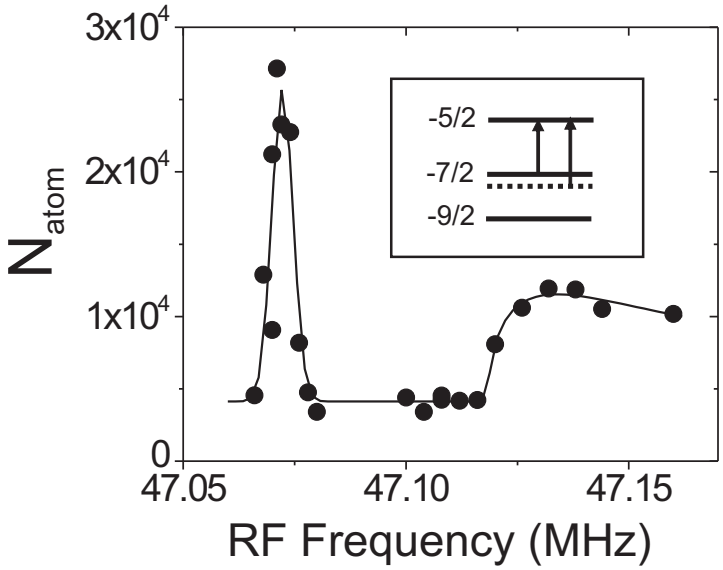

Figure 3.3: **RF molecule dissociation** (Main figure) An rf lineshape taken at 201.25 G at frequencies near the $|9/2, -7/2\rangle$ and $|9/2, -5/2\rangle$ energy splitting. The sharp feature at lower energy corresponds to the bare transition for an unpaired atom with a width determined by the energy resolution. This energy splitting can be used to calibrate the magnetic field. The broad feature at higher energy is the molecule dissociation feature. The solid line is the combination of a gaussian for the bare atom transition and a theoretical molecule dissociation curve (eq. 3.8) for the higher frequency feature. By fitting the the molecule dissociation curve, the binding energy for the molecule at this magnetic field is obtained. In this case, we obtain a binding energy of $h \times (46.4 \pm 1.5)$ kHz. (Inset) A schematic showing the transitions corresponding to the two observed features. Three solid lines mark the energies (vertical axis) of the three lowest m_F states. Initially, only the lower two states are occupied. The shorter arrow marks the bare atom transition of the rf lineshape. If the atom is bound in a molecular state its energy is lowered by E_B (dotted line) and the transition is shifted to higher frequency. In addition, the atoms can be dissociated into a continuum state with finite kinetic energy above the bare $|9/2, -5/2\rangle$ line, which accounts for the high frequency tail of the molecule dissociation feature.

pulse. The power of the rf pulse is modulated by a gaussian envelope with a full width $1/e^2$ max duration of 300 μs, such that the Fourier limited energy resolution is a Gaussian of full width $1/e^2$ max equal to 4.3 kHz. A sample rf lineshape is shown in Figure 3.3.

Two features can be observed in the lineshape. A narrow feature at low frequency corresponds to flipping the spin of unpaired or free atoms from the $|9/2, -7/2\rangle$ state to the $|9/2, -5/2\rangle$ state. The center frequency of this feature can be used to calibrate the experimental value of the magnetic field. A second broad feature at higher energy corresponds to the dissociation of bound molecules. The shape of this feature is determined simply from the wavefunction overlap between the molecular state and scattering states of two atoms and Fermi's golden rule. An analytic formula for the number of atoms transferred as a function of rf frequency is given in Ref. [39, 40] to be

$$I(\nu_{rf}) \propto \frac{\sqrt{h\nu_{rf} - E_B}}{(h\nu_{rf})^2} \tag{3.8}$$

where ν_{rf} is the rf frequency minus the frequency of the single-atom transition and E_B is the molecule binding energy. Here we have assumed that interactions between the initial and final states are negligible.

By fitting the rf lineshape to Eq. 3.8 we can determine E_B. This measurement was repeated for a number of magnetic-field values with the results plotted in Figure 3.4. The binding energy of the Feshbach molecules near the resonance is well approximated by [6]

$$E_B = \frac{\hbar^2}{m(a - r_0)^2} \tag{3.9}$$

where a is given by Eq. 3.4 and $r_0 \approx 60a_0$ is the range of the Van der Waals potential [6]. Fitting the binding energy data to this formula with $r_0 = 60a_0$ and $a_{bg} = 174a_0$ yields $B_0 = 202.20 \pm 0.02$ G and $w = 7.04 \pm 0.1$ G. The parameters r_0 and a_{bg} are constrained by theory and other measurements [6, 41], however, prior to this measurement B_0 was only known to within an error of 0.07 G [6].

In this experiment, rf spectroscopy simply served as a tool to measure the binding energy of a low density and, hence, weakly interacting gas of Feshbach molecules. This was possible because we have an analytic formula for the Fesbach molecule wavefunction ($\Phi(r) \propto \frac{e^{-r/a}}{r}$ [4]) and can predict

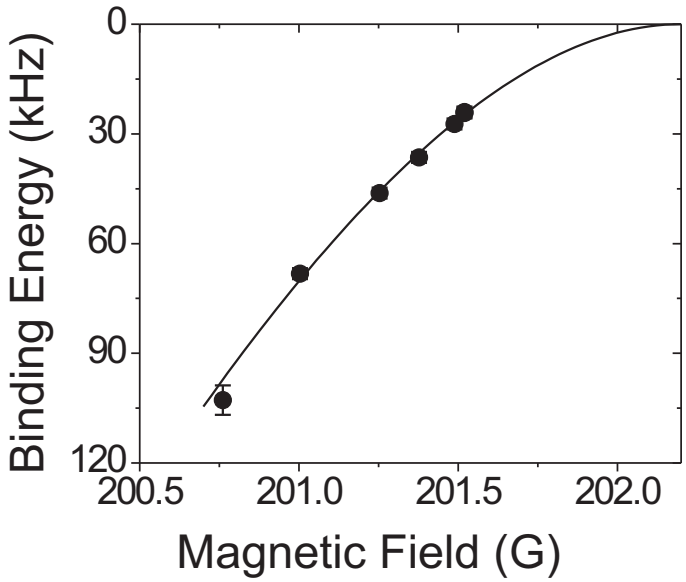

Figure 3.4: **s-Wave molecule binding energy** Measurements of molecule binding energies near the s-wave Feshbach resonance between the $|9/2, -7/2\rangle$ and $|9/2, -9/2\rangle$ states of ^{40}K atoms (black dots) are plotted as a function of magnetic field. The black line is a fit to eq. 3.9. The fit values are given in the text.

the rf lineshape (Eq. 3.8) based on this and Fermi's golden rule. However, we will see in Chapters 5,6 how rf spectroscopy can also be used as a tool for probing a strongly interacting system where we do not know the form of the many-body wave function.

3.3.2 Determination of p-wave molecule binding energies with magneto-association

To measure the binding energy of p-wave molecules we took advantage of another spectroscopic technique pioneered at JILA and demonstrated for s-wave resonances in ^{40}K by our group in Ref. [42]. The technique is a molecule association technique whereby one starts with a gas of unpaired atoms and then oscillates the magnetic field at a frequency close to the molecule binding energy divided by h. The oscillating field drives the atoms into bound molecules via a stimulated emission process. When molecules are formed they can be lost due to inelastic collisions with other atoms or molecules, which allow them to fall into deeply bound molecular states and gain enough energy to escape the confinement trap. Thus, an atom loss feature can be a signature of molecule association.

In these experiments, we cool a balanced spin mixture of atoms in the $|9/2, -9/2\rangle$ and $|9/2, -7/2\rangle$ states to $T/T_F = 0.2$. We ramp the magnetic field to a value near the p-wave Feshbach resonance, which occurs near 199 G. Then, we apply a small sinusoidal oscillation to the magnetic field at a frequency ν_{mod} for a duration of 36 ms. We record the number of atoms in the $|9/2, -7/2\rangle$ as a function of ν_{mod}; sample lineshapes are shown in Fig. 3.5.

In Fig. 3.5, we observe an asymmetric atom loss feature that has a width that increases with the cloud energy $E_G = \frac{1}{2}m\langle v^2\rangle$, where the rms velocity is obtained from a Gaussian fit to the expanded cloud. E_G is thus a measure of the average kinetic energy of the particles and is proportional to the range of atom collision energies. The width and shape of the association feature arises from the distribution of collision energies in the atom cloud. To determine the binding energy of the molecule, we measure the peak energy of the loss feature as a function of E_G and extrapolate to $E_G = 0$. We repeated this measurement at multiple fields around the resonance and the results are shown in Fig. 3.6.

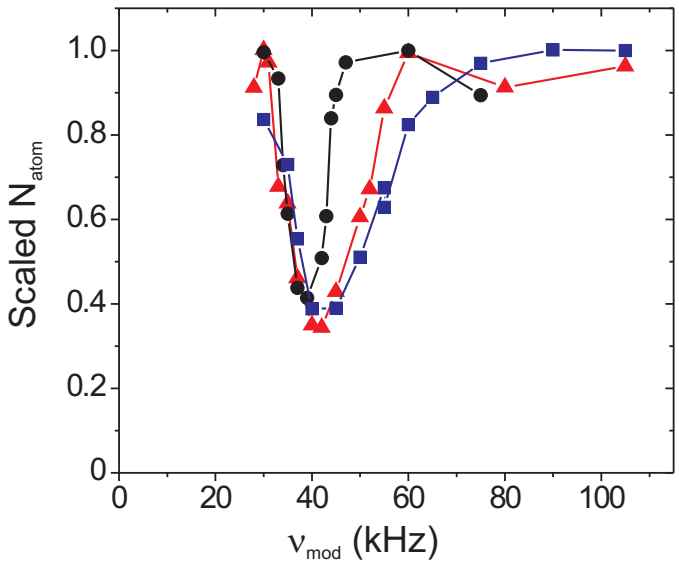

Figure 3.5: **p-Wave molecule magneto-association lineshapes** Lineshapes for association to a bound p-wave molecule using a sinusoidally modulated magnetic field. For this data, $B = 198.12$ G. We find that the line shape is asymmetric and has a width that depends on the kinetic energy of the atoms E_G, which is defined in the text. The data are for values of E_G of $h \times 2.0$ kHz (circles), $h \times 4.5$ kHz (triangles), and $h \times 6.0$ kHz (squares). To highlight the asymmetry and dependence on E_G, the total number of atoms, N_{atom}, for each lineshape was scaled to one. This figure is from Ref. [2].

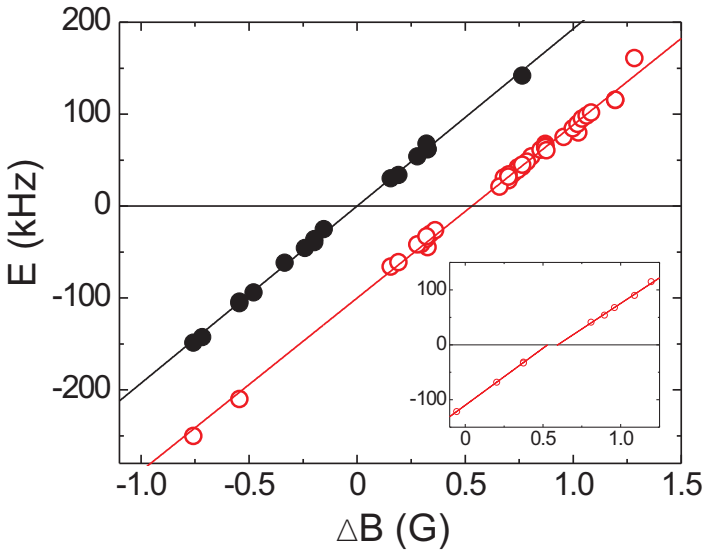

Figure 3.6: **p-Wave molecule energies** Energy of the molecule as a function of magnetic field for both the $m_l = 0$ (open circles) and $m_l = \pm 1$ (closed circles) resonances. $E < 0$ corresponds to a bound molecule; $E > 0$ corresponds to a quasi-bound state. ΔB is the detuning from the $m_l = \pm 1$ resonance position, which we measure to be $B = 198.30 \pm .02$ G. Linear fits give a slope of 188 ± 2 kHz/G for the $m_l = 0$ resonance and 193 ± 2 kHz/G for $m_l = \pm 1$. The inset shows data for the $m_l = 0$ resonance that suggest some non-linearity near the resonance. These data were taken all in one day to reduce the uncertainty in the magnetic field. This figure is from Ref. [2].

As can be seen in Fig. 3.6, there are two features, which we identify as corresponding to p-wave molecules with different values of m_l. We measure the magnetic-field difference between the resonances for molecules with $m_l = \pm 1$ and $m_l = 0$ to be approximately 0.5 G. The splitting arises from the magnetic dipole interaction and was first observed in Ref. [43] and explained in Ref. [38]. For both molecule features, we observe a linear dependence of the pair energy, E, on magnetic-field detuning. We measure the center of the $m_l = \pm 1$ resonance, the lower magnetic-field feature, to be 198.30 ± 0.02 G.

Interestingly, we can follow the molecule association feature to positive energies where no true bound molecular state exists. The feature at positive energies is due to association to a long-lived resonance state, or quasi-bound state, with the lifetime of that state being determined by the tunneling time through the centrifugal barrier (Fig. 3.2). The tunneling time causes the width of these features to be as much as three times larger than for bound states, for data taken with similar initial cloud energies.

We can take advantage of this resonant state to directly observe the presence of p-wave molecules and distinguish between the $m_l = 0$ and $m_l = \pm 1$ states. For these experiments we found it advantageous to use a spin polarized gas of atoms in the $|9/2, -7/2\rangle$ state to eliminate non-resonant s-wave collisions. We start with a 95/5 mixture of $|9/2, -7/2\rangle$ and $|9/2, -9/2\rangle$ and then obtain a nearly pure spin-polarized gas with a slow sweep through the s-wave resonance at 202.2 G where inelastic losses on the low side of the resonance ensure that nearly all $|9/2, -9/2\rangle$ atoms are lost [44]. At this point, we run into the unfortunate situation whereby the gas cannot rethermalize any further because s-wave collisions are forbidden by quantum statistics. We lower the trap depth to reach 10^5 atoms, but the gas is no longer in thermal equilibrium.

While we can create molecules using magneto-association as discussed above, it turns out to be far more efficient to simply hold the magnetic field near the Feshbach resonance for a few ms. To detect the presence of molecules, we quickly increase the magnetic field, in 10 μs, to a value above the resonance where the quasi-bound molecules have a large positive energy. The ramp adiabatically converts the bound molecule into the quasi-bound state. The paired atoms

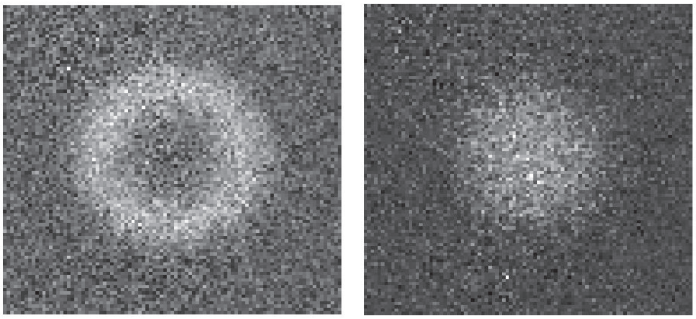

Figure 3.7: **Dissociated p-wave molecule clouds** Images of dissociated p-wave Feshbach molecules. A linear grayscale indicates the optical depth, with white corresponding to more absorption of the resonant probe light. The images are taken after a 4 ms ballistic expansion from the trap and therefore show the velocity distribution of the atoms resulting from the dissociation of the Feshbach molecules. The left image corresponds to the $m_l = \pm 1$ resonance and the right image corresponds to the $m_l = 0$ resonance. The image plane is transverse to the quantization axis, which is defined by the external magnetic field. The images show the expected angular distributions for p-wave pairs. This figure is from Ref. [3].

then tunnel out of the centrifugal barrier and this energy is converted to kinetic energy of atoms flying apart. We then immediately turn off the optical trap, expand for a variable time of 1.9 to 5 ms, and take an absorption image. If we wish to remove the unpaired atoms before imaging the molecules, we can use a pulse of laser light that is resonant with the free atoms while the magnetic field is still at a value on the bound state side of the resonance. Since the molecules do not absorb this light they are unperturbed. The result is a large energetic cloud of atoms, as seen in Fig. 3.7. This is similar to a detection scheme used in Ref. [45] for narrow s-wave resonances. The angular distributions seen in Fig. 3.7 are consistent with p-wave pairing.

3.4 Measurement of molecule lifetimes

In the discussion of p-wave resonance, we saw that to parameterize the resonance we need to measure the lifetimes of the resonant states. We accomplish this using two methods. One method takes advantage of the molecule detection technique discussed above. Here, we create molecules on resonance and then ramp to a field where we wish to measure the lifetime. Then, we detect the number of molecules by quickly jumping the field to a value where the pair energy is much higher and will be converted to kinetic energy of free atoms, as discussed above. These measurements are shown as circles in Fig. 3.8.

A second technique takes advantage of magneto-association. Here, we can use the measured width of the magneto-association line shapes to deduce an energy width or lifetime of the quasi-bound molecules. It is important to remove the effect of broadening due to the finite energy distribution of the atoms in order to measure the intrinsic energy width we are interested in. These points are shown as squares in Fig. 3.8.

Putting these two measurements together and fitting a line through the data we find that the inverse tunneling rate $\tau^{-1} = \alpha E^{3/2}$ with $\alpha = \frac{1}{h^{\frac{3}{2}}}(2.2 \pm 0.1)10^{-3} s^{\frac{1}{2}}$. This agrees well with a theory prediction from John Bohn [2] shown as the solid line in Fig. 3.8. If we use the inverse tunneling rate to calculate an energy width using $\Gamma_p = \tau^{-1}/(2\pi)$, and take $E = h \times 10$ kHz, which is a typical Fermi energy for our system, we find an energy width of $h \times 0.35$ kHz, which is much smaller than

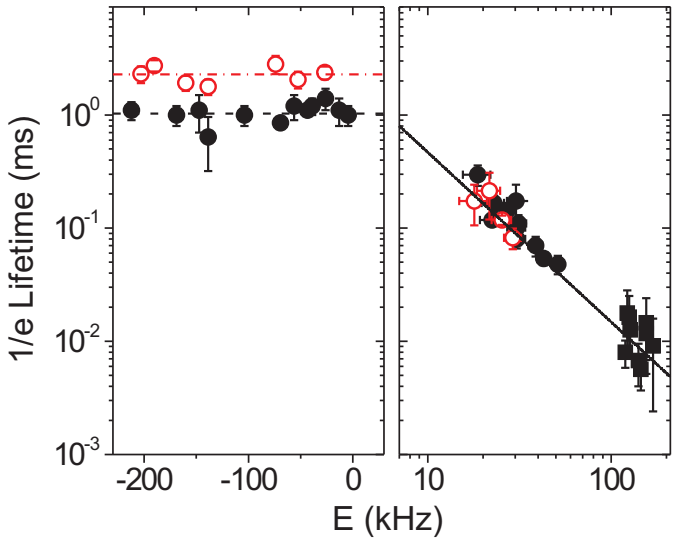

Figure 3.8: **p-Wave molecule lifetimes** Lifetimes of p-wave molecules are plotted as a function of the molecule energy. Negative energies (left) correspond to bound molecules, while positive energies (right) correspond to quasi-bound pairs. Data for the $m_l = 0$ resonance are shown in open symbols, while $m_l = \pm 1$ are closed symbols. The two dotted lines on the left indicate averages of the measured bound state lifetimes. The solid line on the right is a theory curve for the quasi-bound lifetimes. This figure is from Ref. [2].

E_F, putting us well into the narrow resonance regime.

We can also use direct molecule detection to measure the lifetimes of bound molecules below the resonance using the same method as for the quasi-bound molecules. Here, we measure lifetimes of 2.3 ± 0.2 ms for the $m_l = 0$ molecules and 1.0 ± 0.1 ms for $m_l = \pm 1$ molecules. These values show no measurable dependence on binding energy or magnetic-field value. Theory work from John Bohn predicts molecule lifetimes set by dipolar relaxation rates of 8.7 ms and 6.8 ms for the $m_l = 0$ and $m_l = \pm 1$ molecules [2]. Dipolar relaxation is a process where two atoms fall into lower energy spin states and fly apart with the extra kinetic energy. In the dipolar relaxation process angular momentum is conserved by an increase or decrease in the orbital angular momenta of the atoms. Dipolar relaxation is possible for these p-wave Feshbach molecules because atoms in the $|9/2, -7/2\rangle$ are not in the lowest energy spin state. The fact that we measured shorter lifetimes than predicted by theory points to other possible decay mechanisms such as collisional decay.

It is important to remember that Feshbach molecules are molecules in the least bound state of the atom-atom potential and that many other deeply bound states exist. In the pseudo-potential approximation, we ignore the presence of these states as they have no effect on the two-body scattering and interactions. However, if three or more atoms come together, inelastic processes that leave two atoms in a deeply bound state become possible. If two of the atoms are already in the Feshbach molecule state, the wave-function overlap with the more deeply bound states is significantly increased and the process can be strongly enhanced.

In order to test whether atom-molecule collisions were playing a role in the p-wave molecule lifetimes, we measured the molecule lifetime after removing all remaining free atoms. Since the conversion efficiency of atoms to molecules was about 20%, the remaining free atoms were the most likely collision partners for the molecules. Free atoms were removed with a resonant pulse of light that heated them out of the trap. Using this technique, we measured a molecule lifetime of 7 ± 1 ms for the $m_l = 0$ molecules (Fig. 3.9), consistent with the theoretical prediction for dipolar relaxation.

If a p-wave resonance existed in the lowest energy Zeeman state, it would be possible to

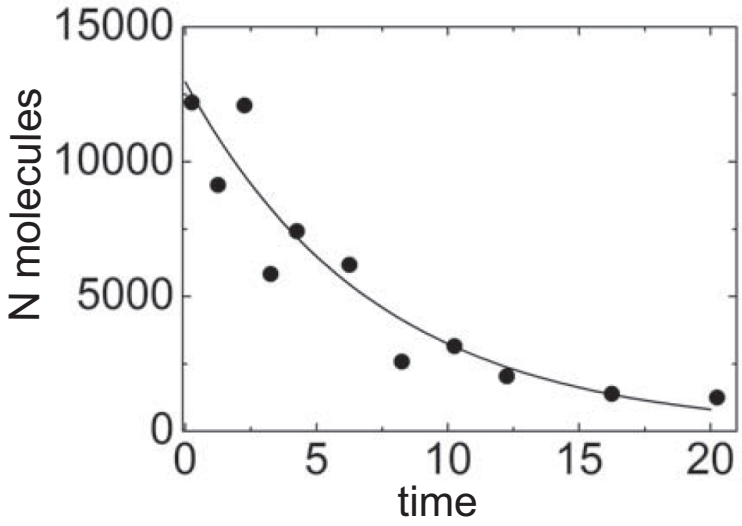

Figure 3.9: **Effect of atom removal** p-wave Feshbach molecule lifetime after removal of free atoms. The molecules were created at the $m_L = 0$ resonance. The solid line is a fit to an exponential decay which gives a lifetime of 7 ± 1 ms. This figure is from Ref. [3].

eliminate dipolar relaxation as a possible decay channel. However, no such resonance exists for ^{40}K. Interestingly, ^{6}Li has a p-wave resonance in the lowest energy state and, following our work, groups in Australia and Japan set about creating and measuring p-wave molecule lifetimes in ^{6}Li [46, 47]. The Japanese group was able to observe p-wave molecule lifetimes that were limited only by inelastic collisional losses [46].

It is interesting to contrast the general features of the p-wave molecule lifetime measurements with previous s-wave molecule lifetime measurements performed by our group [44]. First of all, measurements of quasi-bound state lifetimes were not possible for the broad s-wave resonance. For the s-wave resonance, we expect the quasi-bound state lifetimes to be extremely short, and thus the energy width of any feature to be very large, since there is no centrifugal barrier. In fact, for a broad s-wave resonance there is no quasi-bound state immediately above the resonance [35]. On the bound-state side of the resonance, the s-wave molecule lifetimes are found to depend strongly on magnetic-field detuning from the resonance. This is because the size of the s-wave molecule is a strong function of binding energy and hence detuning from the resonance. Smaller molecules have better wave function overlap (Frank-Condon overlap) with deeper bound molecular states and thus decay more rapidly into those states via inelastic collision processes. In contrast, the size of the p-wave molecules are not expected to vary with molecule binding energy since their size is largely set by the presence of the centrifugal tunneling barrier.

Furthermore, the s-wave molecules are found to have long lifetimes at small binding energies, which are much longer than what we measured in the case of p-wave molecules. This can be attributed to the greater size of the s-wave molecules and hence smaller overlap with deeper bound states as well as a stronger Pauli suppression of inelastic processes [48].

3.5 Creating p-wave molecules near the Feshbach resonance

As noted above, we found that it was possible to produce large numbers of p-wave molecules by setting the magnetic field to a value near the resonance and waiting. With our method to see the molecules, we could dynamically probe this process. In these experiments, we ramp the magnetic

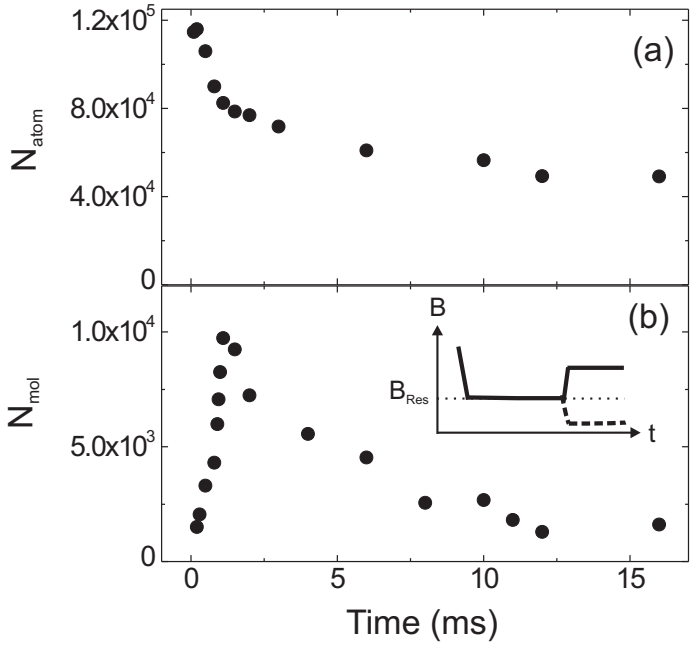

Figure 3.10: **p-Wave molecule creation** (a) Measured atom number as a function of time that the magnetic field is held at the $m_L = \pm 1$ resonance. (b) Measured molecule number for the same hold time on resonance. The inset shows the timing sequence for this experiment. The number of molecules is measured using the dissociation technique described in the text (solid line.) The number of atoms is measured by ramping the field below the resonance (dashed line) where the imaging does not detect molecules. This figure is from Ref. [2].

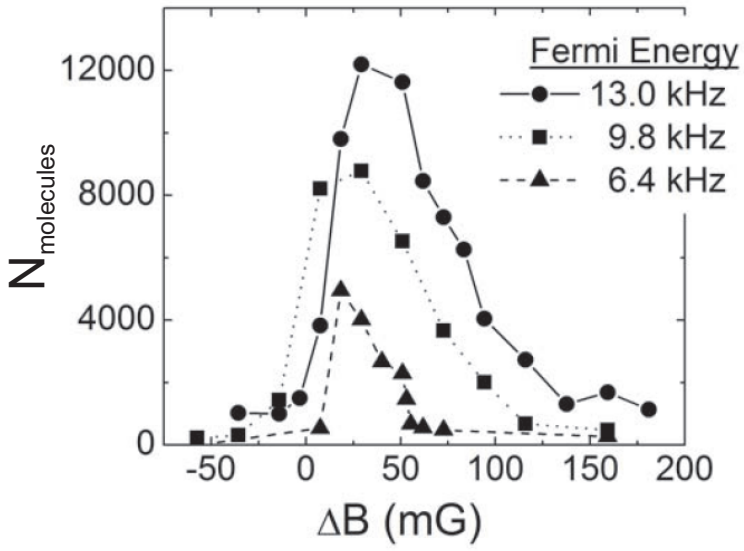

Figure 3.11: **p-Wave molecule creation vs. magnetic field** Number of molecules created for a 1 ms hold vs. magnetic-field detuning from the resonance. The data suggest that molecule creation occurs only when the p-wave resonant state has a positive energy that is less than the maximum collision energy between atoms in the Fermi gas.

field to a value near the Feshbach resonance and then hold for a variable amount of time. To detect the presence of molecules we quickly jump the field above the resonance and expand the cloud as described in the previous section. Alternatively, the number of atoms can be measured by ramping the field below the resonance where the imaging light is not sensitive to the bound molecules. The experimental sequence is shown in the inset of Fig. 3.10. In Fig. 3.10, we show the number of atoms and molecules as a function of hold time near the resonance. The data in Fig. 3.10 was taken for the magnetic-field value where we observe the highest conversion efficiency to molecules. The molecule population increases rapidly for approximately 1 ms and then decays with a time constant on the order of a few ms. At long times both the atom and molecule populations decay monotonically, indicating that inelastic loss processes are taking place.

In Fig. 3.11, we show the number of molecules created after a 1 ms hold time for different detunings from the Feshbach resonance and also for different values of the Fermi energy. We see that molecule creation occurs only over a small range of magnetic-field values near the resonance. The molecule creation feature is asymmetric and has a width that increases with increasing cloud energy. This suggests the width of the feature arises from the atomic kinetic energy distribution in the cloud rather than any intrinsic width. This is consistent with our determination that the gas is in the narrow resonance limit.

3.6 p-wave superfluids

Ultimately, the goal of this research was to explore the possibility of creating a strongly interacting Fermi gas dominated by p-wave interactions where a p-wave paired superfluid state might be accessed. Such an unconventional superfluid would be extremely interesting from the point of view of condensed matter physics due to the vector order parameter (compared to the s-wave case) and possibilities for quantum phase transitions [49, 50, 51, 52]. Furthermore, in two dimensions it is predicted that such a system could exhibit non-Abelian topological excitations, which is a topic of wide interest with possible applications to decoherence-free quantum computing [53].

In order to study many-body physics in a strongly interacting atomic gas, it is important for the rate of inelastic processes in the gas to be small compared to the rate of elastic scattering. One way to think about this is that the true ground state of the cold atom gas is actually for all the atoms to bind together and crystalize. In this sense, the dilute gas is in a highly excited metastable state. However, as long as the relaxation rate to lower energy states is slow enough, it can essentially be ignored. In this case, we can study the physics of the metastable state, which is governed by elastic scattering processes between the atoms and can be mapped onto a pseudo-potential problem that has no deeply bound states. In practice, one runs up against some inelastic processes, and in particular, three-body collisions that lead to the formation of more deeply bound dimers. The amount of energy released in such a collision is so great that the atoms promptly fly out of the trap and stick to the wall of the vacuum chamber. Thus, the presence of inelastic decay to deeply bound states manifests itself as atom and molecule loss in the trapped gas. As long as this loss process is slow compared to many-body timescales in the system, which are generally set by the elastic collision rate, we can study the low energy many-body physics of the quantum gas.

In the case of Fermi gases near s-wave resonances, this criteria is met as long as one doesn't go too far onto the molecule side of the resonance [6]. However, it does not seem to be met in the case of the narrow p-wave resonance. Atom and molecule lifetimes near the p-wave resonance in our system were too short for us to observe any elastic scattering processes. The Japanese group confirmed that for ^{6}Li near the p-wave resonance inelastic collision rates were too large to allow for equilibration of the system [46].

Nevertheless, I am hopeful that this is not the end of the story. We were never able to develop a satisfactory model of the molecule creation process that we observed for a cold gas held near the p-wave resonance [3]. It is possible that interesting many-body physics is occurring here at the same time as the inelastic decay processes. If we knew what questions to ask and had a good way to probe the gas, there might be interesting physics to be learned. I suspect atom photoemission spectroscopy, the main topic of this thesis, would be an interesting tool to try and apply to this system and there is a group out there working towards this possibility [54].

Moreover, it is predicted that for atoms confined to two-dimensions the ratio of the elastic to inelastic loss rates would be more favorable, though still less favorable than the s-wave case [48]. An optical Feshbach resonance could perhaps be used to enhance p-wave collisions while minimizing inelastic rates. Also, optical lattices may help in preventing three-body loses [55]. While these routes to p-wave superfluidity are uncertain, the reward of success would be high and it may be a worthwhile endeavor to pursue them (assuming you already have tenure). However, for the rest of this thesis, I will return to studies of strongly interacting gases via a broad s-wave Feshbach resonance.

Chapter 4

Fermi superfluids and the BCS-BEC crossover

In this section I discuss the BCS theory of superfluidity (or superconductivity in metals) and the concept of the BCS-BEC crossover. My discussion of BCS theory comes from the book by J.R. Schrieffer [5], which was written back in 1964 but is still quite readable, as well as the classic many-body theory book by Fetter and Walecka [56], and also the helpful review [4]. For the BCS-BEC crossover, I will present some of the early results obtained in our group from Cindy Regal's thesis [6] and also use insights from the review [4].

4.1 The pairing theory of Fermi superfluidity (BCS Theory)

4.1.1 Cooper pairs

While a non-interacting Bose gas undergoes a phase transition at low temeperatures to a Bose-Einstein condensate, non-interacting Fermi gases have no phase transitions even as the temperature is lowered to zero. Furthermore, Fermi gases with short-range repulsive interactions remain a Fermi liquid, a state similar to a non-interacting Fermi gas but with renormalized parameters, down to zero temperature (with the possible exception of a transition to a ferromagnetic state if interactions are extremely strong [57]). However, if attractive interactions exist, an instability in the Fermi liquid state is introduced and the system has a transition to a superfluid state at low temperatures. A hand-wavy way to think about this transition is to say that the attractive interactions allow the fermions to form pairs, those pairs are bosons, and the bosons can undergo Bose condensation. What is truly amazing about the superfluid transition however, is that it occurs even for arbitrarily

weak attractive interactions, even though those attractions would be far too weak to bind together two fermions in free space. To get some insight into this conundrum, it is helpful to examine what has been termed the Cooper instability.

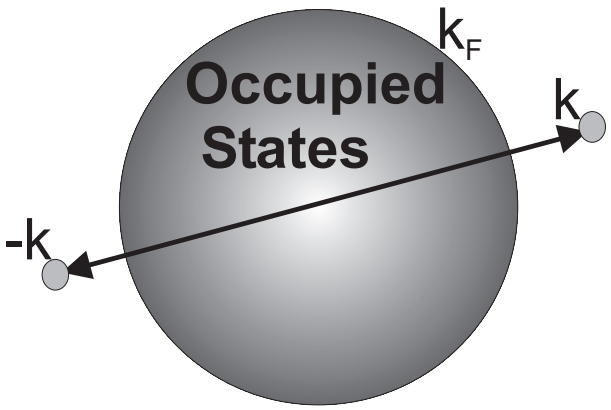

Figure 4.1: **Cooper's problem** In Cooper's problem, two fermions coexist with a non-interacting Fermi sea (filled circle). The two fermions with zero center of mass momentum interact via a weak attractive interaction. The Fermi sea affects the problem only by Pauli blocking, which prevents states with momentum less than $\hbar k_F$ from being occupied. Shown are possible wave vectors k and $-k$ outside of the Fermi sea that the two fermions may occupy. In the absence of the Fermi sea, the kinetic energy cost associated with forming a bound state would outweigh the energy decrease from forming a paired state. However, in the presence of the Fermi sea it can be shown that a such a pair will lower the energy of the two fermions below $2E_F$. This many-body pair is stabilized by the Fermi sea and called a Cooper pair.

The thought experiment is as follows [58]: Consider a non-interacting Fermi sea and then add two interacting fermions with zero center-of-mass momentum on top of that Fermi sea (Fig. 4.1). The Fermi sea affects the problem only by Pauli blocking, which prevents the two fermions from occupying any of the k states below the Fermi surface. If there were no interactions, the two new fermions would have energy $2E_F$ since each would have to sit on top of the Fermi sea. With attractive interactions, it turns out they can lower their energy a small amount by forming a loosely bound state called a Cooper pair. This problem is worked out in detail in a number of textbooks and reviews. For the problem of fermions where the interactions can be characterized by scattering length a, the binding energy would be $E_B = \frac{8}{e^2} E_F e^{-\pi/k_F|a|}$. This bound state could not exist in the absence of the underlying Fermi sea and therefore the pair is really a many-body pair, although

it is important to note that in this case the correlations with all the other atoms in the Fermi sea are not caused by interactions but by quantum statistics.

Now, we have not solved the problem of many fermions interacting via a weak attractive interactions, but we can use our insight from the Cooper problem to guess what the solution will look like. In the fully interacting problem, many fermion pairs should form and condense leading to a superfluid state. It turns out the pairing gap of the full many-body state in the BCS limit is actually [5, 56, 4]

$$\Delta_0 = \frac{8}{e^2} E_F e^{-\pi/2k_F|a|} \tag{4.1}$$

4.1.2 Properties of the superfluid state

4.1.2.1 Critical temperature

The first natural question about the superfluid state is what is the critical transition temperature. In order for the Cooper pairs to survive, one might guess that the temperature should be on the order of the pair binding energy. This turns out to be approximately correct with [5, 56, 4]

$$T_c = T_F \frac{e^\gamma}{\pi} \frac{8}{e^2} E_F e^{-\pi/2k_F|a|} = \frac{e^\gamma}{\pi} \Delta_0 \tag{4.2}$$

where γ is Euler's constant and $e^\gamma \approx 1.78$.

For ^{40}K, the background scattering length is $174a_0$ and in our experiments typically $k_F^{-1} \approx 2000a_0$ which would give $\frac{T_c}{T_F} \approx 10^{-8}$; this is far below the temperature range that is experimentally accessible. Without a Feshbach resonance to enhance interactions, atomic Fermi gas experiments would not be able to access the superfluid regime.

4.1.2.2 The energy

The total energy of the superfluid is lowered from the non-interacting state by pairing and can be written [5, 56, 4]

$$E_{\mathrm{BCS}} = \frac{3}{5}NE_F - \frac{\Delta_0}{2}\rho(E_F)\Delta_0 \tag{4.3}$$

where $\rho(E_F)$ is the density of states at the Fermi energy. The first term is simply the non-interacting energy of the normal state. The second term is the pairing energy and can be interpreted as coming from $\rho(E_F)\Delta_0$ paired atoms each with pairing energy $\frac{\Delta_0}{2}$. In other words, pairing occurs in a region of energy width Δ_0 about the Fermi surface.

4.1.2.3 The gap

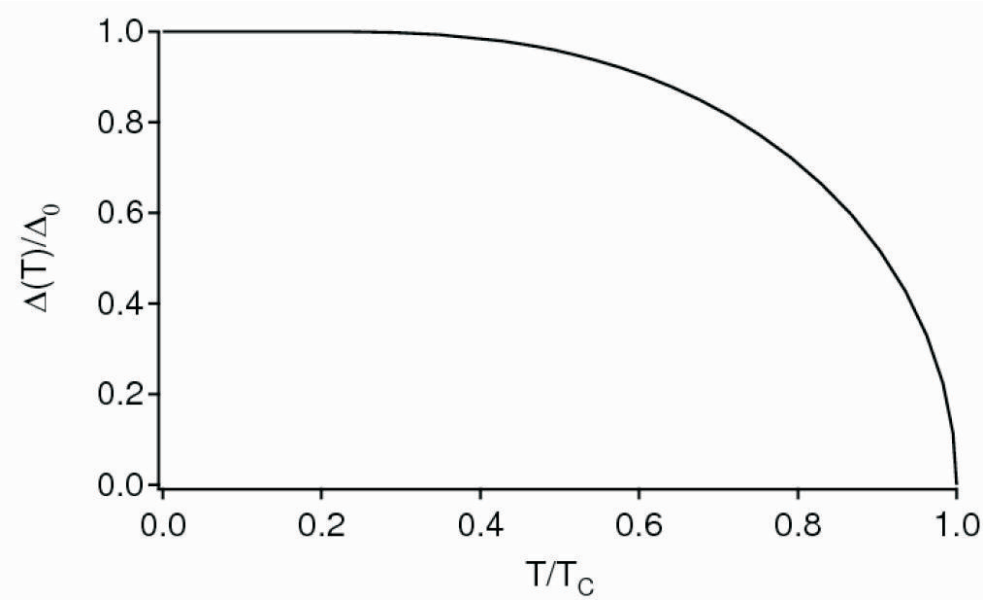

Figure 4.2: **The temperature dependence of the pairing gap** The temperature dependent pairing gap $\Delta(T)$ as a fraction of the gap at zero temperature, Δ_0, is plotted as a function of the temperature compared to the critical temperature T/T_c. The pairing gap vanishes at T_c. This figure is taken from Ref. [4].

In the superfluid phase at finite temperature, the pairing gap decreases as T increases and above T_c it vanishes. In the BCS limit, the pairing gap can be considered to be the order parameter

for the phase transition. In other words, the sudden appearance of pairing and the gap are the same phenomenon as the transition to a superfluid. The temperature-dependent gap formula must be solved numerically and is plotted in Fig. 4.2.

4.1.2.4 Pair-size

In the BCS limit, the pair wave function at large r can be approximated as $\sin(k_F r)e^{-r/\pi\xi}$ [4] where ξ can be written $\frac{2}{k_F}\frac{E_F}{\Delta}$. Since Δ is much smaller than E_F in the BCS limit, the pair size is much greater than the average inter-particle spacing, which is of order $\frac{1}{k_F}$. This is the reason it is not so easy to simply say the BCS superfluidity is a bunch of fermion pairs that Bose condense. Rather, it is a system of many very large and overlapping pairs where the pair constituents are all strongly correlated with each other through the Pauli exclusion principle.

4.1.2.5 Quasi-particles and the excitation spectrum

Another question is how does the gap manifest itself in the excitation spectrum and what do the single-particle states look like in the paired superfluid. One way to answer this question is to examine the solution of the BCS problem by canonical transformation. We can write the mean-field BCS Hamiltonian in second quantization in grand canonical (non-particle conserving) form as [56, 4]

$$H_{\mathrm{BCS}} = \sum_{k,\sigma}(\epsilon_k - \mu)a^\dagger_{k,\sigma}a_{k,\sigma} - \Delta\sum_k(a_{-k\downarrow}a_{k\uparrow} + a^\dagger_{k\uparrow}a^\dagger_{-k\downarrow}) \tag{4.4}$$

where $a^\dagger_{k,\sigma}(a_{k,\sigma})$ are the fermion creation (destruction) operators for a fermion at momentum k with spin σ and $\epsilon_k = \frac{\hbar^2k^2}{2m}$ is the bare fermion energy. In order to diagonalize the Hamiltonian, we introduce the quasi-particle operators

$$\gamma_{k,\uparrow} = u_k a_{k\uparrow} - v_k a^\dagger_{-k\downarrow} \tag{4.5}$$

$$\gamma_{k,\downarrow} = u_k a_{k\downarrow} + v_k a^\dagger_{-k\uparrow} \tag{4.6}$$

This transformation is canonical if the anticommutation relations $\{\gamma_{k,\sigma}\gamma^{\dagger}_{k',\sigma'}\} = \delta_{k,k'}\delta_{\sigma,\sigma'}$ are satisfied, which leads to $u_k^2 + v_k^2 = 1$. If we plug eq. 4.5 into eq. 4.4 and do enough algebra, we find [5, 56, 4]

$$H_{\text{BCS}} = \sum_{k,\sigma} E_k \gamma^{\dagger}_{k,\sigma}\gamma_{k,\sigma} \tag{4.7}$$

where

$$E_k = \sqrt{(\epsilon_k - \mu)^2 + \Delta^2} \tag{4.8}$$

Thus, the elementary excitations of the system are given by the $\gamma^{\dagger}_{k,\sigma}$'s and E_k is the energy due to a quasi-particle at momentum k. The energy to add a particle at k is $E_k(N+1) - E(N) = \mu + E_k$, where $E_k(N)$ is the energy of an N-particle system with a quasi-particle excitation at k. The energy to remove a particle at k is $E(N) - E_k(N-1) = \mu - E_k$. These excitation energies are plotted in the top part of Fig. 4.3. As can be seen, there is gap of 2Δ between the lower and the upper branch. One way to think about this spectrum is to say the lower branch for the quasi-particle hole excitations represents the energy of the single-particle states in the ground state and the upper branch are the excitations.

It is also possible to obtain the values of u_k and v_k, which are also called the coherences. We find [5, 56, 4]

$$u_k^2 = \frac{1}{2}(1 + \frac{\epsilon_k - \mu}{E_k}) \tag{4.9}$$

$$v_k^2 = \frac{1}{2}(1 - \frac{\epsilon_k - \mu}{E_k}) \tag{4.10}$$

The coherences are plotted in the bottom of Fig. 4.3. We see that away from the Fermi surface the quasi-particles are essentially the bare particle and hole operators. Only near the Fermi surface where pairing occurs is there significant particle-hole mixing between states with opposite spin and momenta.

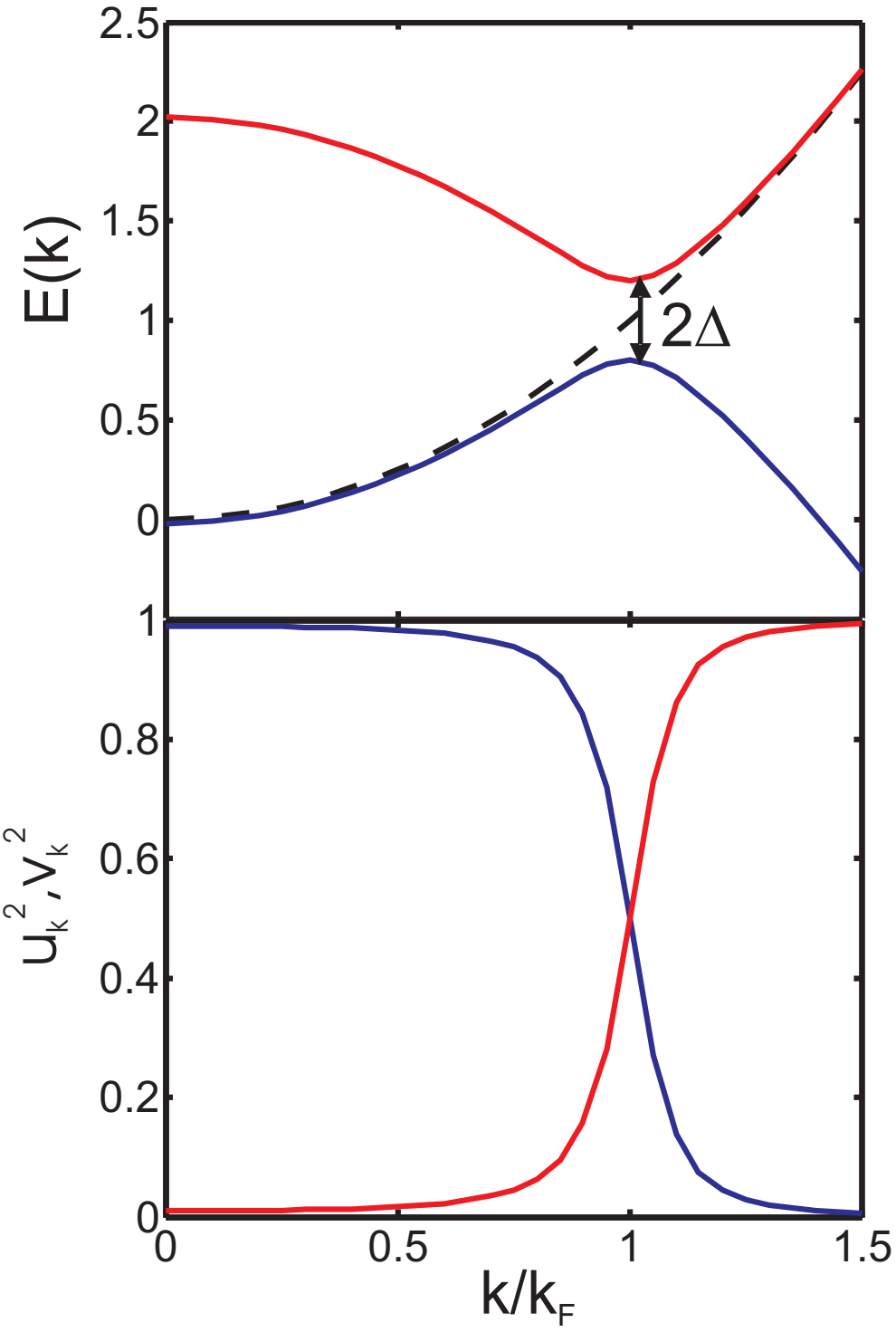

Figure 4.3: **BCS quasi-particles** Top) The dispersion relation for the BCS quasiparticles. The top branch (red) is the energy of excitations on top of the BCS ground state (adding unpaired fermions). The lower branch (blue) is the energy associated with removing particles in the BCS ground state. The dashed line is the free-particle dispersion. The upper and lower branches of the BCS dispersion are separated by twice the pairing gap Δ. Bottom) The coherences u_k^2 (red) and v_k^2 (blue) are plotted vs k. Far from the Fermi surface, the coherences approach either 1 or 0 showing that in those limits the quasi-particle states are the same as the free-particle states. Near the Fermi surface, the quasi-particles are superpositions of particle and hole states with opposite momenta and spin. The coherence v_k^2 gives the occupied k states in the ground state and shows that the momentum distribution is smeared out [5]. The plots here are for a gap equal to $0.2E_F$. We have used $\mu = \frac{\hbar^2 k_F^2}{2m}$ for a weakly interacting Fermi gas.

4.2 Turning up interactions: The BCS-BEC crossover

From eq. 4.2 we know that reaching the superfluid regime in our ^{40}K gas will not be possible with background interactions. But how high can we make T_c if we enhance interactions by turning up the scattering length using a Feshbach resonance? With the Feshbach resonance, we can tune the scattering length all the way up to $-\infty$ where a true bound state is on the verge of appearing in the atom-atom potential. If we plug this into eq. 4.2, we find $T_c = 0.61T_F$. However, this is clearly outside the regime of validity for BCS theory, which requires weak interactions and $\Delta \ll E_F$ [5, 56, 4] (here we would have $\Delta = 1.1E_F$). If we backtrack to an interaction strength where we still expect BCS theory to be approximately correct, say $k_F a = -1$, we find $T_c = 0.13T_F$ and $\Delta = 0.23E_F$. This temperature is experimentally accessible.

It is instructive to look at what happens as the Feshbach resonance is crossed and a true bound state is introduced into the two-particle potential. This is the "BEC side" of the resonance. The reason for the name is clear; if we go far enough so that we are again in the limit of weak interactions ($\frac{1}{k_F a} \gg 1$) the ground state is a Bose-Einstein condensate of dimer molecules where the binding energy of each molecule is given in Eq. 3.9 to be $\hbar^2/(ma^2)$ for a broad Feshbach resonance. Here, the pair size is on order of the scattering length a [4] and thus much smaller than the inter-particle spacing. In this limit, we can calculate T_c from the Bose-Einstein condensation temperature with a boson density of $n/2$ bosons and mass $2m$. This gives $T_c/T_F = 0.22$ for the BEC limit.

We can guess that in the range of interaction strengths of $-1 < \frac{1}{k_F a} < 1$ the transition temperature is in the range of $0.1-0.2\ T_F$, which is an extremely high superfluid transition temperature for a Fermi gas. This is the region of the BCS-BEC crossover, named because we are going from the limit of small negative scattering length where the superfluid state is described by conventional BCS theory to the limit of small positive scattering length where the ground state is a molecular BEC. It was first proposed by Leggett [59] that this crossover should be smooth with the ground state being a Fermi superfluid all the way across. As a first naive approximation, an adaptation

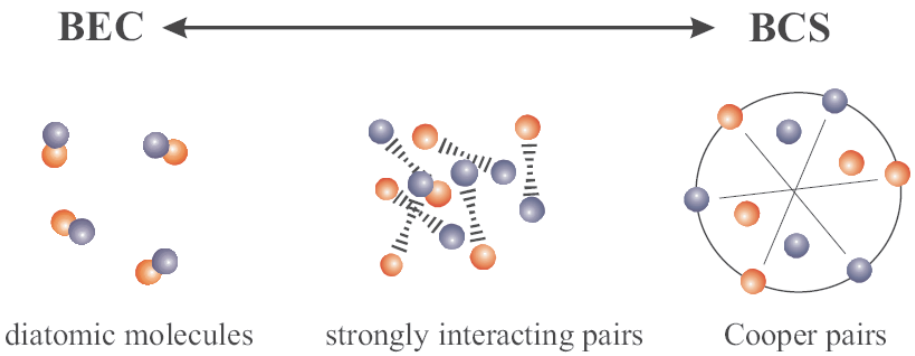

Figure 4.4: **Pairs in the crossover** The different regimes of pairing are shown for a Fermi gas with attractive interactions. In the BEC limit, the pairs are tightly bound molecules with a pair size much smaller than the inter-particle spacing and the critical temperature is given by that for Bose-Einstein condensation of weakly interacting bosons, which is approximately $0.22T_F$. In the BCS limit, where the attractive interactions are weak, Cooper pairs can form and the Fermi gas is a BCS superfluid. Here, the critical temperature is exponentially small, given by eq. 4.2. The crossover takes places for interaction strengths of $\frac{1}{k_F a} = -1$ to 1. In this region, the pair size is on order of the inter-particle spacing and the gas is strongly interacting with a critical temperature in the approximate range of $0.1 - 0.2T_F$. This figure is taken from [6].

to conventional BCS theory can be made by allowing the chemical potential, which equals E_F on the BCS side, to vary continuously to its limit of $-E_b/2$ on the BEC side where E_b is the molecule binding energy [59, 60, 61]. This allows one to solve for quantities like the chemical potential, the gap, and the pair wave function. The theory predicts that the pair size varies smoothly from the BCS limit of large Cooper pairs to a pair size on the order of the interparticle spacing in the crossover and then to a pair size on the order of the scattering length a in the BEC limit [4], as shown in Fig. 4.4. The minimum fermion excitation energy varies smoothly from twice the BCS gap, eq. 4.1, to a value on order of the Fermi energy in the crossover and then to the molecule binding energy on the BEC side [6]. However, while this theory captures some of the physics of the crossover, it is not quantitatively accurate since it does not take into account all of the strong correlations that occur in the BCS-BEC crossover. In fact, no controlled theory has been possible in this regime due to the lack of a small parameter with which one can apply perturbation theory [35]. From the point of view of experiments, though, this is exactly the regime we want to be in, where many-body correlations are the strongest and the system is the hardest to understand. It is here that we can hope to make measurements that contribute to fundamental many-body quantum theories.

The first major experimental goal was to demonstrate that a superfluid could be achieved in this strongly interaction regime and that a smooth crossover between the BCS and BEC limits of interacting fermions did indeed exist. The first experimental evidence for the strongly interacting Fermi superfluid came from our group in 2004 with the observation of a condensate in the center-of-mass pair momentum distribution [7]. This experiment is somewhat analogous to the observation of Bose-Einstein condensation by looking at the atom momentum distribution and seeing a condensate peak at zero-momentum. The important difference is that with fermions, there is no condensate in the atom momentum distribution. The trick was to find a way to measure the center-of-mass momentum distribution of the pairs, and this was done by projecting the pairs in the many-body system onto tightly bound molecules by ramping across the Feshbach resonance. Further confirmation of superfluidity followed in 2005 when the group at MIT found that at low

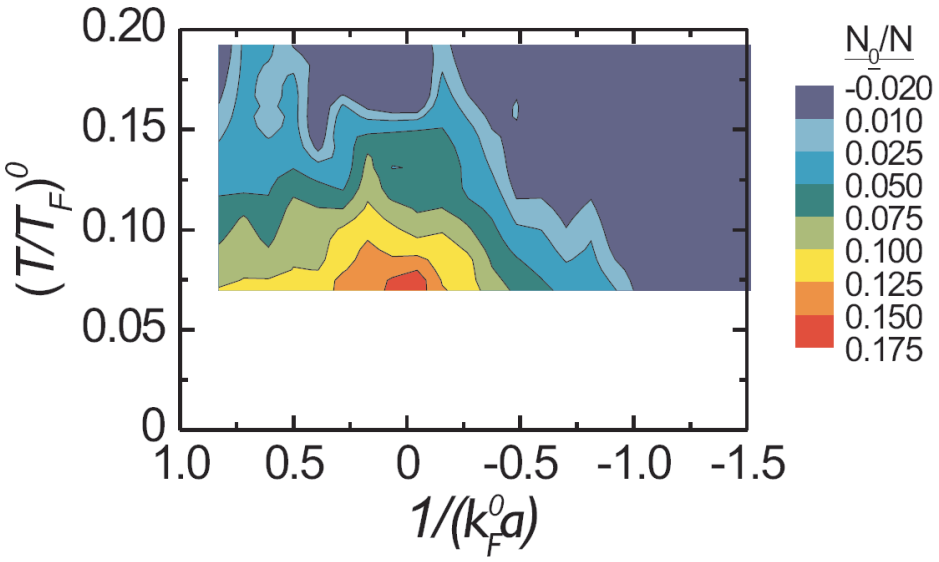

Figure 4.5: **BCS-BEC crossover phase diagram** An experimental measurement of condensate fraction, N_0/N, as a function of temperature and interaction strength allows one to map out the superfluid region in the BCS-BEC crossover. The right side of the plot is the BCS side and the left side is the BEC side. The transition temperature is the highest near the center of the crossover ($\frac{1}{k_F a} = 0$) and on the BEC side; T_c falls off quickly on the BCS side. On the vertical axis the temperature reported, $(T/T_F)^0$, is that of a weakly interacting gas before an adiabatic ramp that increases the interaction strength. This figure is taken from [6] and was first published in [7].

temperatures they could observe a vortex lattice by rotating the gas [62]. Since then a number of experiments have been consistent with the observation of a superfluid state including measurements of thermodynamics [63, 13] and collective excitations [64, 65]. It turns out the method developed at JILA to measure the pair condensate is quite sensitive to the transition and therefore is good for measuring T_c and mapping out the phase diagram. This was done in Ref. [7] and the main result is reproduced in Fig. 4.5. As can be seen in Fig. 4.5, the critical temperature decreases on the BCS side of the diagram and levels out to about $0.15T_F$ on the BEC side. It is important to note that the temperature given is that of a weakly interacting Fermi gas before it was adiabatically ramped to the strongly interacting regime. In this ramp, entropy is conserved but the temperature is expected to increase. On the BCS side, and even at unitarity, this effect is rather small (about a 15% increase in $\frac{T}{T_F}$ at T_c at unitarity [66]) but the temperature increase can be quite large for adiabatic ramps into the BEC regime [66].

After this great experimental achievement, the goal of the next generation of experiments became a bit more murky. Clearly, we had the ability to generate a very interesting system, where correlations were so strong that theories based on approximations were uncontrolled and insight into the system was more difficult. Furthermore, it was a system that was relevant to other strongly correlated systems like quark-gluon plasmas, neutron stars, and strongly correlated electron systems. So, the goal had to be to somehow make measurements that could give physical insight and guide theoretical frameworks in a way that would lead to a better overall understanding of this strongly correlated fermion system. A great number of experiments were done that helped contribute to this goal, including measurements of momentum distributions [67] and potential energy [30] in our group and other measurements of thermodynamic quantities, collective excitations, rf spectroscopy (to name only a few) in other groups across the world [4]. All of these measurements could be compared with theories and with quantum Monte-Carlo simulations to test their accuracy and to try to gain physical insight.

In this thesis, I will present some experimental measurements that I think have been particularly helpful in getting to the heart of this strongly correlated system. These measurements are

based on momentum-resolved rf spectroscopy and they directly measure the single-particle spectral function of the fermion system in a way that is analogous to angle-resolved photoemission spectroscopy of strongly correlated electron materials. The spectral function tells us about the single-particle states and knowledge of it allows us to describe the system in the language of Fermi liquid theory and standard quantum many-body theory. Measuring the spectral function will help us answer some basic questions, such as can we describe this system in terms of quasi-particles and does the normal gas behave as a Fermi liquid or does a pseudo-gap state exist? Furthermore, the spectral function is an excellent quantity to directly compare with theories because it is a fundamental quantity of the system.

In the next chapter, I will explain what the single-particle spectral function is and how it behaves for the paradigms of Fermi liquids and BCS superfluids. I will also explain how we can measure it experimentally and what some initial experiments can tell us about the BCS-BEC crossover.

Chapter 5

Fermi liquids, spectral functions, and photoemission spectroscopy

In this section I introduce the language of Fermi liquid theory and spectral functions and show how these quantities help us understand the nature of interacting Fermi systems. I discuss how to measure the spectral function of an atomic Fermi gas using a momentum-resolved rf spectroscopy technique. I present our first measurements of the spectral function in the BCS-BEC crossover, however I try to be brief as these experiments are discussed in detail in Jayson Stewart's thesis [34]. I also describe how we improved the signal-to-noise ratio of these measurements by changing our imaging scheme, and I present some recent higher-signal-to-noise data. My discussion of Fermi liquids and spectral functions borrows often from Refs. [56, 68, 69] as well as from course notes from Jim Shepard and Victor Gurarie for many-body physics courses taught at CU. The original photoemission data I present was published in Ref. [9].

5.1 Landau's Fermi liquid theory

As discussed in Chapter 2, the single-particle eigenstates of a non-interacting Fermi gas are plane-wave states characterized by a wave-vector k and energy $\frac{\hbar^2 k^2}{2m}$. In the many-body ground state, fermions fill these states up to the Fermi surface at wave-vector k_F. Excitations on top of this ground state can be classified as particle or hole excitations. A particle excitation is the occupation of an extra state $k > k_F$ above the Fermi surface with an excitation energy of $\frac{\hbar^2|k^2-k_F^2|}{2m}$ compared to the ground state of the $N+1$ particle system. If $k - k_F \ll k_F$ the excitation energy can be approximated as $\hbar v_F|k - k_F|$ where $v_F = \frac{\hbar k_F}{m}$ is called the Fermi velocity. A hole excitation

is the absence of a particle in a state $k < k_F$ and has the same energy as the particle excitation, with k now being the wave-vector of the empty state.

For an interacting Fermi gas, the plane-wave states are no longer the eigenstates and it is not clear how to describe the system in terms of a simple picture as we did for the non-interacting gas. Landau's bold insight was to adapt the non-interacting picture of single-particle plane-wave states for the interacting system with a few simple modifications. A thought experiment shows that this should be a valid approximation for excitations near the Fermi surface. In this thought experiment, we first postulate that there is still a well-defined Fermi surface in the interacting system. Then, we add a particle excitation at momentum $\vec{k}$ above the Fermi surface and ask what the probability is for that particle to scatter into another state. The mechanism for scattering is to collide with another particle with $|\vec{k}'| < k_F$ into two final states above the Fermi surface, say $\vec{k}_1$ and $\vec{k}_2$, see Fig. 5.1. If the matrix element for collisions around the Fermi surface is roughly constant, this is a question of phase space. In other words, how many possible collision partners and final states exist? We require conservation of momentum and energy, as well as $|\vec{k}'| < k_F$ and $|\vec{k}_1|, |\vec{k}_2| > k_F$. We can satisfy conservation of momentum by taking $\vec{k}' = \vec{k}_1 + \vec{k}_2 - \vec{k}$. Then we can write the total number of possible collisions for a single-particle excited above a filled Fermi sea as

$$N(k) = \int d^3\vec{k}_1 \int d^3\vec{k}_2 \;\; \delta(|\vec{k}|^2 + |\vec{k}_1 + \vec{k}_2 - \vec{k}|^2 - |\vec{k}_1|^2 - |\vec{k}_2|^2)\theta(|k_1| - k_F)\theta(|k_2| - k_F)\theta(k_F - |\vec{k}_1 + \vec{k}_2 - \vec{k}|) \tag{5.1}$$

where $\theta(x) = 1$ for $x > 0$ and $\theta(x) = 0$ for $x < 0$; this is the zero temperature limit of the Fermi Dirac function. To model a finite temperature gas, the θ functions can be replaced by Fermi Dirac functions, which give the probability of occupation, $(\theta(k_F - k) \to f(E, T))$. An analogous equation can be written down to describe the phase space for a hole excitation below the Fermi surface to decay (see Fig. 5.2).

It turns out for $k - k_F \ll k_F$, $N(k) \propto (k - k_F)^2$ or $N(k) \propto E(k)^2$ [56, 68, 69] (see Fig. 5.2). This is remarkable because it says the number of collision possibilities for a particle at k to scatter to another state goes to zero near the Fermi surface. Thus excitations near the Fermi surface are

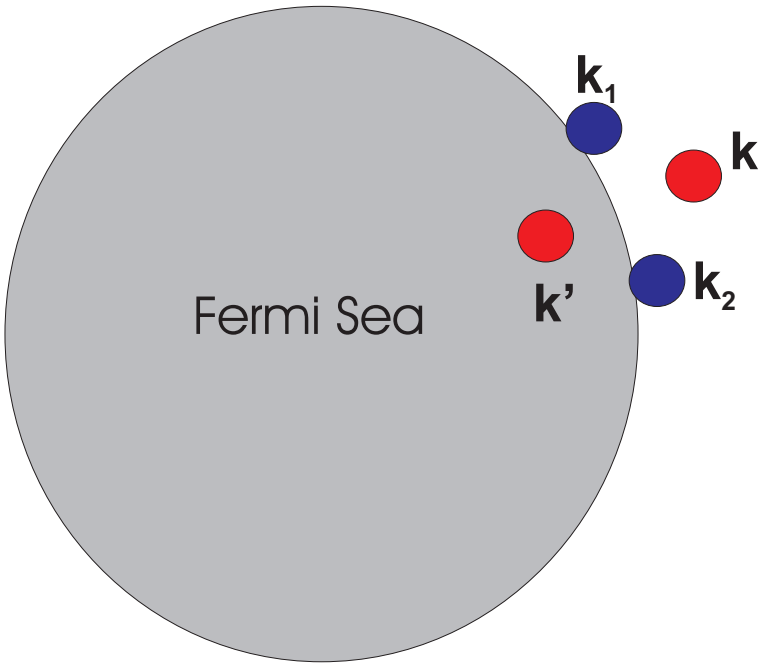

Figure 5.1: **Quasi-particle decay process** A particle excitation is made by placing a fermion in the momentum state $\vec{k}$ above the Fermi surface. It can decay by colliding with another fermion below the Fermi surface in state $\vec{k}'$. The final states are $\vec{k}_1$ and $\vec{k}_2$, which must be above the Fermi surface. The number of possible collisions that conserve energy and momentum is proportional to $|k - k_F|^2$. As $k \to k_F$, the number of possible collisions decreases to zero because of Pauli blocking.

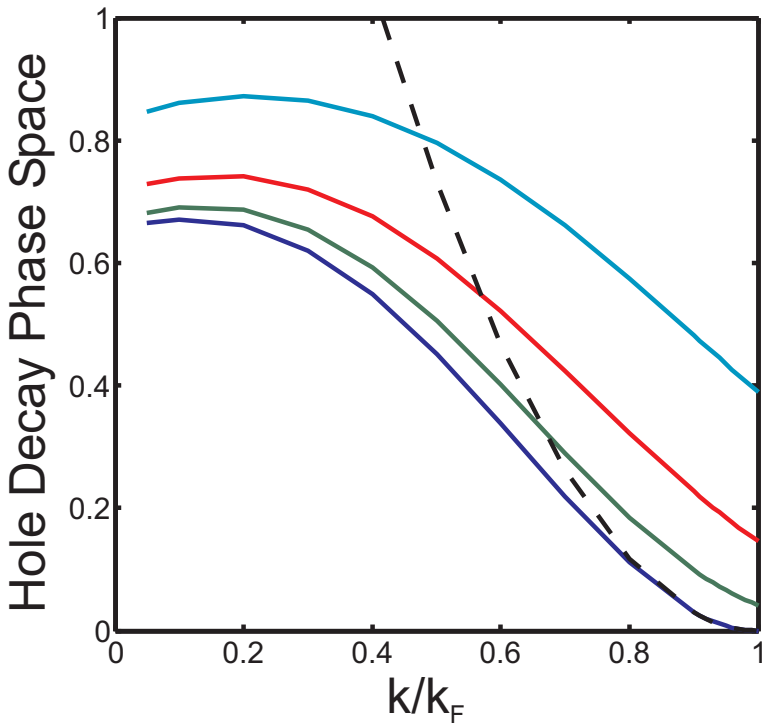

Figure 5.2: **Hole-decay phase space** The total number of collisions, or phase space, for a hole excitation to decay is plotted versus k/k_F for different temperatures. The y-axis is plotted in arbitrary units. From lowest to highest, the curves shown correspond to temperatures of $\frac{T}{T_F} = 0$, 0.1, 0.2 and 0.4. The dotted line is a quadratic curve meant to show the low energy limit where $N(k) \propto |k_F - k|^2$. As temperature increases, the phase space for collisions at $k = k_F$ is proportional to T^2 at low $\frac{T}{T_F}$. A hole excitation decays when two fermions inside the Fermi sea collide, with the final state being one fermion filling the hole at k and the other excited out of the Fermi sea. The equation describing this process is analogous to Eq. 5.1, but for hole excitations and finite temperature. It can be written $N(k) = \int d^3\vec{k}_1 \int d^3\vec{k}_2 \ \delta(|\vec{k}_1|^2 + |\vec{k}_2|^2 - |\vec{k}|^2 - |\vec{k}_1 + \vec{k}_2 - \vec{k}|^2) f(k_1, T) f(k_2, T)(1 - f(|\vec{k}_1 + \vec{k}_2 - \vec{k}|, T))$, where $f(k, T)$ is the Fermi Dirac function describing the probability for a state with wave-vector k, and energy $\frac{\hbar^2 k^2}{2m}$, to be occupied at temperature T.

long-lived. Because the inverse collision time goes to zero faster than the excitation energy, the excitations near the Fermi surface can be treated as quasi-particles. An identical argument can be made for hole excitations near the Fermi surface, as plotted in Fig. 5.2. This justifies our postulate that there will still be a well-defined Fermi surface in the interacting system. However, just because a particle or hole excitation near the Fermi surface has a well-defined energy, the magnitude of the excitation energy does not have to be identical to the non-interacting case. Even if there is no phase space for momentum changing collisions, there are still interactions and virtual processes that can lead to a shift in the excitation energies. This leads us to call these excitations quasi-particles, because they now consist of a particle excitation plus that particle's interactions with all the other fermions. For fermions interacting via a short-range potential, the $1/e$ lifetime of an excitation at k is given by

$$\tau^{-1} = \frac{E_F}{\hbar}\frac{2}{\pi}(k_F a)^2 \frac{|k-k_F|^2}{k_F^2} \tag{5.2}$$

in the limit $k - k_F \ll k_F$ and $k_F a \ll 1$ [56]. Note that the scattering rate is proportional to the two-body scattering cross-section $4\pi a^2$.

Near the Fermi surface, we can write the quasi-particle excitation energy as $\frac{\hbar^2 k_F}{m^*}|k-k_F|$ where m^* is called the effective mass of the quasi-particles. For fermions interacting via a short-range potential, the effective mass is given by $\frac{m^*}{m} = 1 + \frac{8}{15\pi^2}(7\ln 2 - 1)(k_F a)^2$ in the limit $k_F a \ll 1$ [56]. The properties of the quasi-particles can be used to determine numerous basic properties of the interacting Fermi gas such as the heat capacity (proportional to m^*), compressibility, sound velocity, and transport properties [56, 68, 69]. This treatment of interacting Fermi gases in terms of quasi-particles is known as Landau's Fermi liquid theory and has been very successful in describing a large class of electronic materials and interacting Fermi gases [56, 68, 69]. However, it is important to remember that: 1) the quasi-particle theory is only strictly valid near the Fermi surface, where the quasi-particles represent well-defined excitations and that 2) the total energy of the system does not equal the sum of the quasi-particle energies (since this would ignore interactions between quasi-particles).

Landau's Fermi liquid theory can be contrasted with the low energy theory for bosons (also developed in part by Landau), which predicts that the low-lying excitations are phonon-like and cannot simply be thought of as renormalized particles [69].

5.2 Green's function and many-body quantum theory

One way to put Fermi liquid theory into a more formal framework is to examine the properties of the Green's function of a many-body system. First, let's examine the Green's function for a single particle. In this case, the Green's function is the probability that a particle at an initial position x_i is found at x_f after a time t and can be written [36]

$$G(x_f, x_i, t) = -i \sum_n e^{-iE_n t} \psi_n(x_f) \psi_n^*(x_i) \tag{5.3}$$

For particles in a box, the Fourier transform of eq. 5.3 gives

$$G(k, E) = \frac{1}{E - \frac{\hbar^2 k^2}{2m} + i\epsilon}, \tag{5.4}$$

where ϵ is needed for convergence but is to be taken to zero. This shows that the energy eigenstates are actually poles of the Green's function [36]. This turns out to be a general structure for any one-particle Hamiltonian [36].

For a many-body problem, the Green's function is defined in an analogous way. Here we add or subtract a particle at position x_i and t_i in the many-body system, let the system propagate, and then check the overlap of that system with one where we add or subtract a particle at x_f and t_f [56]. Analyzing the properties of the Green's function in Fourier space shows that, in analogy to the single-particle problem, the poles of the Green's function represent the energy due to an excitation from adding or subtracting a particle at k [56] (either $E_k(N+1) - E(N)$ for particle excitations or $E(N) - E_k(N-1)$ for hole excitations where E_k indicates the system has an excitation at k). For a Fermi liquid, the Green's function, $G(k, E)$ can be written

$$G(k, E) = \frac{\theta(k_F - k)}{E - \frac{\hbar^2 k^2}{2m} - \Sigma(k) - i\epsilon} + \frac{\theta(k - k_F)}{E - \frac{\hbar^2 k^2}{2m} - \Sigma(k) + i\epsilon} \tag{5.5}$$

where $\Sigma(k)$ is called the self energy and contains all the physics due to the interactions [56]. The two terms correspond to quasi-hole and quasi-particle excitations. The poles will occur at $E = \frac{\hbar^2 k^2}{2m} + \mathrm{Re}\Sigma(k)$ and this is then the energy of quasi-hole or quasi-particle excitation at energy E and momentum k. An important difference from the single-particle case is that the self energy can also have an imaginary component that gives a finite width or lifetime to the quasi-hole excitation.

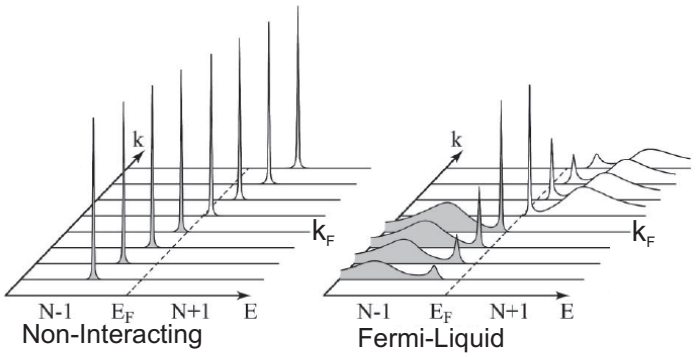

Figure 5.3: **Fermi liquid spectral functions** Left) A representation of the spectral function for a non-interacting gas. Hole excitations are shaded. In this case, the spectral function consists of delta-function peaks at the non-interacting plane-wave energies. Right) A representation of the spectral function for a Fermi liquid. Here the sharp peaks represent the quasi-particles, located at the poles of $G(k, E)$, and the broad peaks represent the incoherent contributions to $G(k, E)$. Near the Fermi surface, the quasi-particle peaks become sharper and contribute a greater fraction of the spectral weight. These figures are adapted from Ref. [8].

An important quantity is the spectral function $A(k, E) = -\frac{1}{\pi} ImG(k, E)$. For a non-interacting Fermi gas, $\Sigma = 0$ and the spectral function is given by $A(k, E) = \delta(E - \frac{\hbar^2 k^2}{2m})$ (Fig. 5.3). For a Fermi liquid, using eq. 5.5, we see that

$$A(k, E) = \frac{-1}{\pi} \frac{\mathrm{Im}\Sigma(k)}{\left(E - \frac{\hbar^2 k^2}{2m} - \mathrm{Re}\Sigma(k)\right)^2 + \left(\mathrm{Im}\Sigma(k)\right)^2} \tag{5.6}$$

which is the equation for a Lorentzian resonance centered at the quasi-particle excitation energy $\frac{\hbar^2 k^2}{2m} + \mathrm{Re}\Sigma(k)$ and with a width given by $\mathrm{Im}\Sigma(k)$ (see Fig. 5.3). For a Fermi liquid with short-range interactions, $\mathrm{Im}\Sigma(k)$ near the Fermi surface is given by $\hbar\tau^{-1}$ where τ is the collision time given in eq. 5.2. The effective mass m^* is found from $m^* = (\frac{1}{m} + \frac{1}{\hbar^2 k_F} \frac{\partial \mathrm{Re}\Sigma(k)}{\partial k}|_{k_F})^{-1}$.

In the superfluid phase, the spectral function of a Fermi gas changes markedly from the Fermi

liquid phase. The spectral function splits into two branches and the energy of the quasi-particles is given by eq. 4.8 and shown in Fig. 4.3. Importantly, at the Fermi surface ($E = \mu$), the spectral function is zero because the gap prevents any states from existing in this region.

Ultimately, the knowledge of the spectral function tells us what has happened to the single-particle states in the interacting system. The nature of those single-particle states tells us how we should think about the physical system we are studying and can help give us physical intuition. Is it a Fermi liquid described by fermionic quasi-particles, a superfluid described by pairing, or is it something completely different? Furthermore, the Green's function is a fundamental quantity that many-body perturbation theory directly computes and so is a good quantity to measure and compare to theory. If a theory does not at least qualitatively get properties of the spectral function right, then it is not a good theory of the underlying physics in the system.

5.3 Photoemission spectroscopy

While several observables of a many-body quantum system can be related back to the Green's function, experiments that directly remove or add single fermions are the most direct probes of this quantity. In materials, angle resolved photoemission spectroscopy (ARPES) directly measures the spectral function of the electrons [8]. ARPES removes electrons via the photoelectric effect. The energy and momentum of the ejected electrons are measured with a hemispherical electron spectrometer (Fig. 5.4). As long as the electron is able to leave the material without colliding with any other electrons, its momentum is preserved. Thus, by using kinematics and knowledge of the photon energy and emission angle, one can back out the electron energy and momentum in the material [8]. This energy and momentum information allows one to reconstruct the electron spectral function by making a two-dimensional plot of the intensity of measured electrons as function of energy and momentum (see Fig. 5.5). Of course, this technique can only measure occupied single-electron states. To measure the unoccupied states, or excitations, there is inverse photo-emission spectroscopy or (IPES) as well as tunneling experiments [8].

ARPES has proven to be an extremely important measurement tool for understanding the

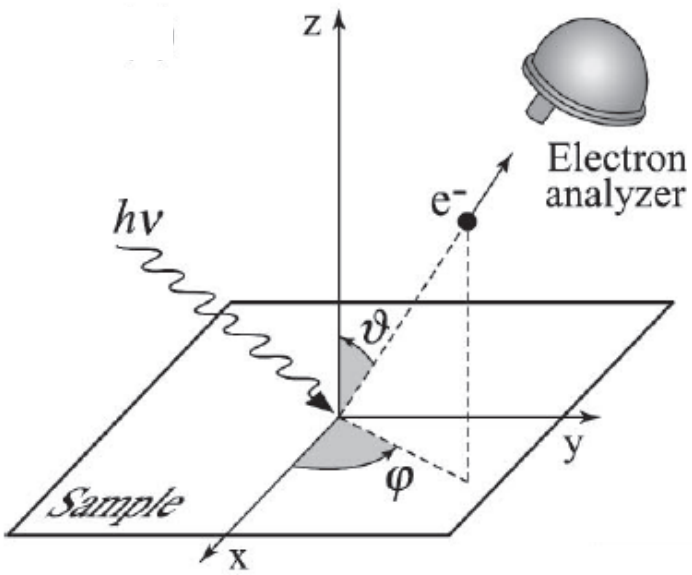

Figure 5.4: **Angle-resolved photoemission spectroscopy** In ARPES, a high energy photon kicks an electron out of the sample via the photoelectric effect. The electron is measured in an electron analyzer that determines the electron energy. This figure is adapted from Damascelli et al. [8].

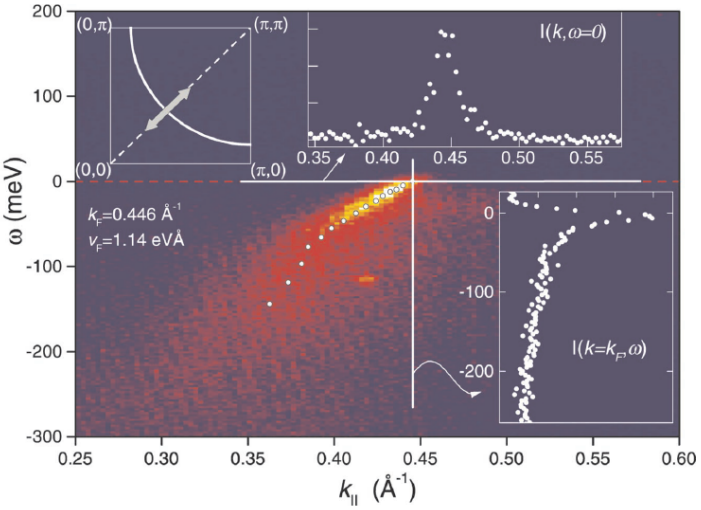

Figure 5.5: **ARPES data** A surface plot is shown representing an ARPES data set obtained from a $Bi_2Sr_2CaCu_2O_{8+\delta}$ for a cut in momentum space, which is shown in the upper left corner and which goes through the Fermi surface ($\omega = 0$). The electron counts are indicated by the red and yellow colors. The quasi-particle dispersion, marked by the white dots, can be followed up to the Fermi surface where the quasi-particles are the sharpest and best defined. Cuts through the data at constant energy ($\omega = 0$) and constant momentum ($k = k_F$) are shown at the top and lower right respectively. These cuts are called momentum distribution curves (MDC) for fixed energy and energy distribution curves (EDC) for fixed momentum. The EDC shows both the quasi-particle feature and broad incoherent background and can be compared to the interacting Fermi gas picture of Fig. 5.3. This figure is taken from Ref. [8].

electronic properties of solids and, in particular, for learning about the nature of strongly correlated electron systems such as high-T_c superconductors, colossal magneto-resistors, graphene, and many others. In particular, ARPES has been important in the discovery of the d-wave symmetry of the gap and elucidation of the properties of the pseudogap state in high-T_c cuprates [8].

It is natural to seek a way to make the same kind of measurement in ultracold atomic Fermi gases. With photoemission spectroscopy for a Fermi gas in the BCS-BEC crossover, one could address questions about the basic nature of the gas. How do the single-particle states evolve from the BCS-like quasi-particles to deeply bound molecules on the BEC side? Can a Fermi liquid state persist with resonant interactions? How large is the pairing gap? At what point do pairing and superfluidity become separate phenomena and does a pseudogap state of many-body pairs exist in the crossover?

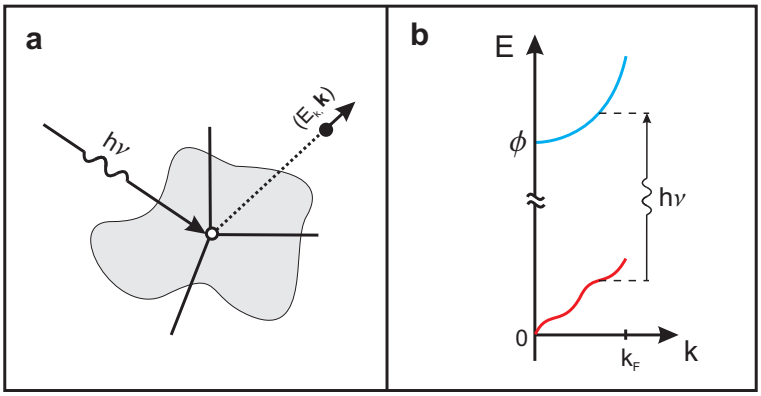

Figure 5.6: **Momentum-resolved atom rf spectroscopy** a) In momentum-resolved rf spectroscopy experiments, one outcouples atoms by flipping them to a weakly interacting spin state via an rf transition. This is analogous to ejecting an electron from a material with a high energy photon Fig. 5.4. b) The rf photon drives a vertical (momentum conserving) transition. By measuring the energy and momentum of the outcoupled atoms (upper curve), we can determine the quasi-particle excitations and their dispersion relation (lower curve). Φ is the Zeeman energy difference between the two spin states of the atom and is analogous to the work function energy of a material. This figure is taken from [9].

Momentum-resolved rf spectroscopy gives us a tool to achieve an analogue of the photoemission spectroscopy measurement for ultracold atomic gases [9]. I will also refer to this measurement as atom photoemission spectroscopy or simply PES. The spectroscopy takes advantage of the many

spin states of the atoms in these cold gases. In a magnetic field, the degeneracy of these states is split by the Zeeman interaction and at magnetic field strengths around the Feshbach resonance (≈ 200 G), the splitting is on order of $h \times 50$ MHz. This Zeeman splitting is much larger than other energy scales in the system, for example $E_F \approx h \times 10$ kHz. Fortunately, all the spin-relaxation mechanisms available to atoms in the two lowest energy spin-states are either forbidden or strongly suppressed, so a gas mixture of atoms in those spin states happily stays that way without relaxing. In ^{40}K, our strongly interacting Fermi gas consists of a mixture of atoms in the $|9/2, -9/2\rangle$ and $|9/2, -7/2\rangle$ states with all the other spin states being unoccupied. An rf magnetic-field transverse to the quantization axis with frequency ν_{rf} can induce spin changing transitions when $h\nu_{rf}$ equals the energy splitting of the spin states. In particular, an atom in the $|9/2, -7/2\rangle$ state can be flipped by an rf photon to the $|9/2, -5/2\rangle$ state with $\nu_{rf} \approx 47$ MHz at fields near 200 G. Near a Feshbach resonance, the interactions between atoms is highly dependent on the spin-states. While interactions between atoms in the $|9/2, -9/2\rangle$ and $|9/2, -7/2\rangle$ states are resonantly enhanced near magnetic field strengths of 200 G, interactions between an atom in one of those states and an atom in the $|9/2, -5/2\rangle$ state remain near their background values characterized by scattering lengths on the order of $100a_0$. This is the key to achieving photoemission spectroscopy. An atom in the $|9/2, -7/2\rangle$ state that is strongly interacting can be "outcoupled" from the interacting system with a spin-changing rf transition. This is analogous to outcoupling an electron from a material by ejecting it with a high energy photon (see Fig. 5.6). In both cases, the energy of the fermion in the final state, either a weakly interacting atom or a free electron, is trivially known. The spin flipped atoms in the $|9/2, -5/2\rangle$ state can be counted because absorption imaging resolves spin states selectively when the Zeeman splitting is greater than the width of the absorption lineshape (approximately 6 MHz).

In a traditional (momentum-integrated) rf spectroscopy experiment, one measures the number of atoms outcoupled, or transferred to the weakly interacting spin-state, as a function of the frequency ν_{rf} (see Fig. 8.1). This sort of experiment has now been used to infer information about the pair wave-function [40] and pairing gap [19] in the BCS-BEC crossover as well as to measure

the contact [10], a subject of Chapter 8. However, a momentum-integrated rf spectroscopy experiment cannot resolve important questions about the single-particle states such as the existence of a pseudogap state or Fermi-liquid-like behavior [70, 71].

Momentum-resolved rf spectroscopy (Fig. 5.6), takes advantage of the fact that the rf photon has a negligible momentum compared to the atom's momentum and so the spin-flip transition does not change the atom's momentum state (this is a vertical transition in the language of photoemission spectroscopy). The momentum of the spin-flipped atom, and thus the momentum of the atom inside the interacting system, can be measured in a time-of-flight experiment. With this information, we can reconstruct the fermionic spectral function. Specifically, the rate of atoms transferred at momentum k and rf frequency ν_{rf}, $I(\nu_{rf}, k)$ is related to the spectral function via

$$I(\nu_{rf}, k) \propto k^2 A(k, E) f(E) \tag{5.7}$$

with $E = \frac{\hbar^2 k^2}{2m} - h(\nu_{rf} - \nu_0)$, where $h\nu_0$ is the Zeeman splitting of the two spin-states [72]. $f(E)$ is the Fermi-Dirac distribution function, which appears because photoemission spectroscopy measures only the occupied part of the spectral function. The energy E is offset so that $E = 0$ corresponds to the energy of a non-interacting atom at rest (as opposed to the usual condensed matter convention where E is measured with respect to the Fermi energy or chemical potential). To understand where this formula comes from, we can look at energy conservation for an rf transition. Initially, we have a photon of energy $h\nu_{rf}$ and the energy of the interacting system with N atoms. Then, we remove one atom and put it into another spin-state where it will have energy $\frac{\hbar^2 k^2}{2m} + h\nu_0$. Thus, the energy change to the interacting system from removing one particle at momentum k is $\frac{\hbar^2 k^2}{2m} - h(\nu_{rf} - \nu_0)$. The factor of k^2 out front in eq. 5.7 is just the volume factor for the number of states at momentum k.

Momentum-resolved rf spectrsocopy compared to ARPES for materials removes some complications but also introduces some new ones. For example, ARPES suffers from ejected electrons colliding with other electrons on their way out of the material [8]. This introduces a background signal and limits ARPES to probing near the material surface. For two-dimensional materials, this

limitation is just technical but for other materials it can make measurements of bulk properties difficult [8]. With atoms, the interactions between the atoms in the outcoupled spin state and the rest of the atoms is so weak that this is not a problem. In other words, the mean free path of the outcoupled atom is much larger than the system size [9]. Furthermore, in ARPES there is a matrix element for the process of removing an electron with a photon that depends on the angles and wave-vectors of the photon and electron [8]. This matrix element is not always known well enough to divide out [8]. In the atom case, the emission process is simply a Zeeman spin-flip transition and the matrix element is constant [72]. Experimentally, the photon source in the atom case (an rf field) is far easier to produce than a synchrotron x-ray radiation source (somewhat of an understatement) or even a laser based UV ARPES source. Also, the detection of atoms by time-of-flight absorption imaging is quite a bit simpler (requiring only a low power laser, CCD camera and imaging optics) than the detection of elctrons with an electron spectrometer. A further general advantage is the ability of ultracold atom gas experiments to reproduce identical samples repeatedly whereas this can be a real challenge in materials science.

However, it is important to note a number of new issues introduced in momentum-resolved rf experiments for atoms. In the atom case, to acquire the full spectral function a range of frequencies are needed, as opposed to ARPES where the entire spectral function for a 2-dimensional material can be measured with a single photon frequency (due to the non-conservation of momentum and energy in the direction perpendicular to the material surface [8]). In ARPES, the energy resolution of the measurements is typically set by the detector resolution and can be made very small compared to the Fermi energy (meV compared to eV) [8]. In the atom case, our energy resolution will be Fourier limited by the duration of the rf pulse, which must be kept much shorter than the oscillation period of the confinement potential in order to keep the momentum of the outcoupled atoms from changing. In our experiments, this limits us to a resolution of approximately $0.2E_F$, although there is some room for improvement here if the aspect ratio of the confinement trap can be reduced. Perhaps the most challenging complication of the ultracold atom gas experiments comes from the density inhomogeneity introduced by the confinement trap. Since the trap is harmonic, the density

is greatest in the center and then decreases to zero with increasing distance from the center. This inhomogenous system can be thought of in terms of a local density approximation. This means locally, inside the atom gas, we can think of the properties of a given shell of the gas with constant density n as having the properties of a homogenous system at that density. The total gas is composed of many of these shells, each with a different density. That means the spectral function we measure will actually be the equivalent of averaging the spectral function of many homogenous gases with different densities and therefore different values of quantities like E_F, k_F and μ, which will range from their peak values at the center of the cloud all the way to zero near the edge. However, this is not as bad as it sounds. Because we know the trap is harmonic, a theory that can predict the spectral function for a homogenous gas can easily be extended to predict the trap-averaged spectral function. The real disadvantage is that this trap averaging can wash out sharp features and make it more difficult to do a quantitative analysis of the data in the absence of theory. I will discuss this issue more and devote a later chapter to some work we have done to decrease the density inhomogeneity and understand its effect on the data.

5.4 Photoemission spectroscopy experiments with a strongly interacting Fermi gas

Ok, enough discussion, it's time to look at some data! In Fig. 5.7, momentum-resolved rf spectroscopy data for a Fermi gas near a Feshbach resonance are shown. For these experiments, the Fermi gas was cooled to $(\frac{T}{T_F})_0 = 0.16$ at a magnetic field strength of approximately 203.5 G where the gas is weakly interacting ($\frac{1}{k_F a} \approx -3$). The subscript 0 indicates the measurement was made in the weakly interacting regime. To change interactions, the gas was then adiabatically ramped to a field B around the resonance. In Fig. 5.7a, the measured spectral function of a weakly interacting Fermi gas with $E_F = h \times 9.3$ kHz and $k_F = \frac{\sqrt{2mE_F}}{\hbar} = 8.6\ \mu\text{m}^{-1}$ is plotted. The Fermi energy is determined by $E_F = \hbar\overline{\omega}(3N)^{1/3}$, where $\overline{\omega}$ is the geometric mean of the confinement trap frequencies and N is the total number of atoms. Interactions are decreased by ramping the magnetic field to $B = 208.43$ G, near the zero-crossing of the resonance, resulting in an interaction

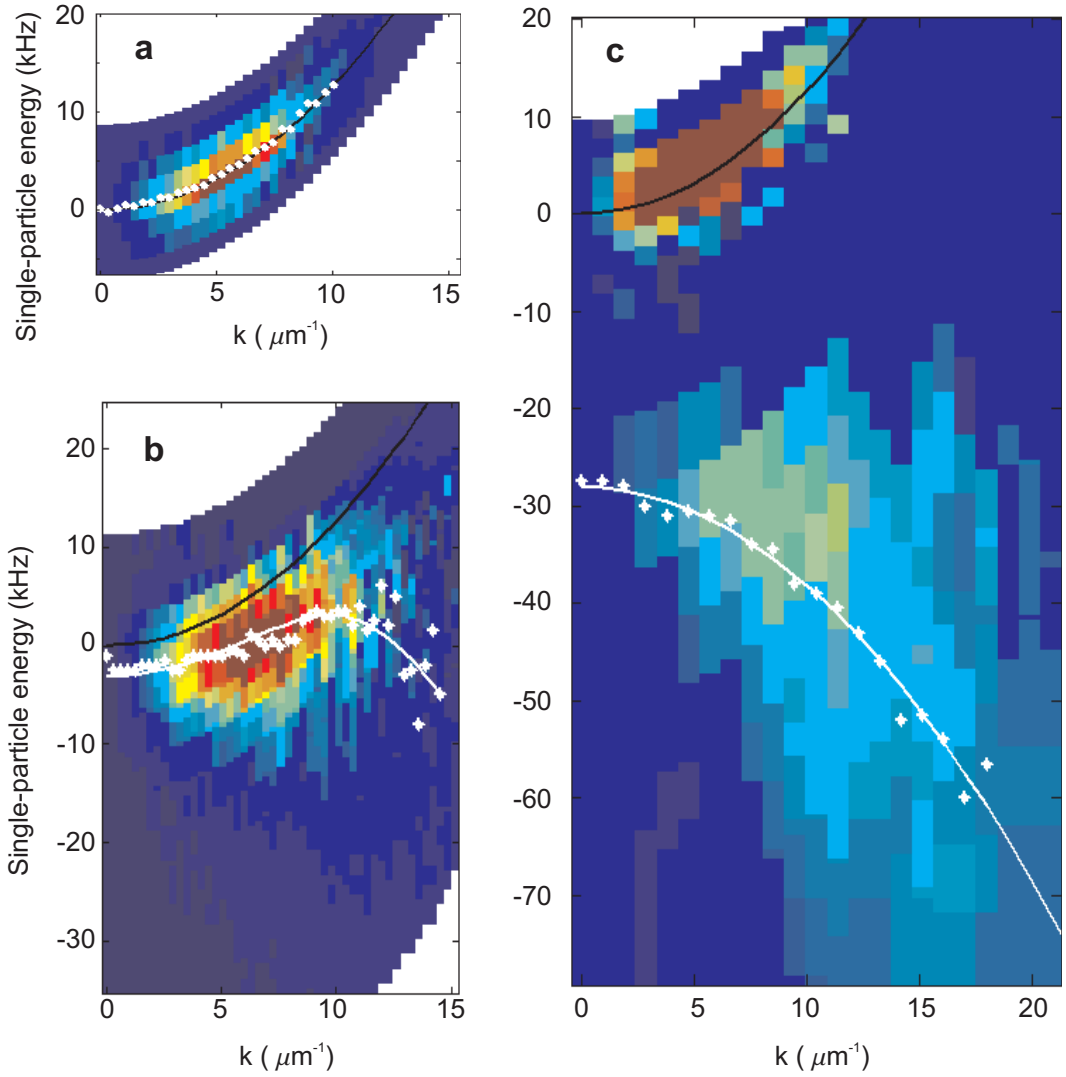

Figure 5.7: **Atom photoemission spectra** a) An atom photoemission spectra, obtained with momentum-resolved rf spectroscopy, for a weakly interacting atom gas. The quasi-particle dispersion (white dots) obtained from gaussian fits to vertical cuts through the data (EDCs) is quadratic and indistinguishable from the expected non-interacting dispersion (black line). b) The spectrum for a strongly interacting Fermi gas near the center of the BCS-BEC crossover. The quasi-particle dispersion is BCS-like, exhibiting backbending near $k = k_F$. c) The spectrum for a Fermi gas in the molecular regime. The top feature is a result of unpaired atoms, which can be treated as a weakly interacting Fermi gas. The lower feature is due to the pairs, which are in the molecular regime and exhibit a negatively dispersing spectrum. EDC's from this data set are shown in Ref. [10].

strength of $\frac{1}{k_F a} = -9.8$. For this gas, the data reveal a spectral function that follows the expected parabolic curve $\frac{\hbar^2 k^2}{2m}$ (black line in Fig. a) of a non-interacting Fermi gas. Each white dot is the center position of a fit to a vertical cut through the data at constant momentum called an energy distribution curve (EDC). An EDC at k gives information about a single-particle excitation at momentum k. Specifically, the location of the peak of the feature is the energy or real part of the self energy $\mathrm{Re}\Sigma(k)$. The width of the feature is related to $\mathrm{Im}\Sigma(k)$. We obtain values for the center and width by fitting a gaussian $Ae^{-\frac{(E-E_0)^2}{2w^2}}$ to each EDC. For the data in Fig. 5.7, we find the EDC widths are constant and equal to 2.2 ± 0.1 kHz, which is consistent with our expected Fourier-limited energy resolution of 2.15 kHz (rms width). It is expected that the intrinsic quasi-particle widths are much smaller than our energy resolution, with $\mathrm{Im}\Sigma(k) \ll E_F$ for a weakly interacting gas, as can be seen in Eq. 5.2. Momentum states are occupied up to k_F with a smearing in k consistent with a harmonically trapped gas at a temperature of $\frac{T}{T_F} = 0.16$.

In Fig. 5.7 b., the momentum-resolved rf spectroscopy data for a gas at $B = 202.1$ and $\frac{1}{k_F a} = 0.17$ [73] is plotted. The Fermi energy, as defined above, is $h \times 10.4$ kHz and $k_F = 9.1$ $\mu\mathrm{m}^{-1}$. Here, we observe a downward shifted dispersion that back-bends near k_F. This back-bending indicates pairing and is well fit by a BCS-like dispersion curve (white line in Fig. b.) with $E = \mu - \sqrt{(\epsilon_k - \mu)^2 + \Delta^2}$ where $\epsilon_k = \frac{\hbar^2 k^2}{2m}$. The best fit gives $\mu = h(12.6 \pm 0.7$ kHz) and $\Delta = h(9.5 \pm 0.6$ kHz). However, these fit values cannot be immediately interpreted as measurements of the chemical potential and the gap for two reasons: the spectral function is obtained from a trapped gas with inhomogenous density, and the gas is in the BCS-BEC crossover, where the dispersion from BCS theory may not be correct. I discuss BCS fits to atom-photoemission data in the BCS-BEC crossover in more detail in the next chapter.

We find the widths of the EDCs are now broadened beyond our energy resolution indicating that the intrinsic energy widths of the quasi-particles may be large. Another possible source of broadening is averaging the signal over the trap. I will present a more detailed comparison of the widths and amplitudes of the EDCs with theory in Chapter 6. It is worth noting that this gas is very close to the transition temperature $(\frac{T}{T_F})_0 = 0.17 \pm 0.01$ measured in Chapter 6 (Fig 6.5).

The fact that even at this high temperature we observe a BCS-like dispersion with back-bending that is consistent with a large gap is already an indication of pseudogap behavior, since it cannot be explained by BCS theory (Fig. 4.2). The temperature dependence of this behavior and its relation to the existence of a pseudogap phase is investigated in Chapter 6. It is important to note that due to the attractive interactions we expect the gas to contract as we adiabatically increase interactions; this leads to a greater atom density in the center of the cloud as compared to the weakly interacting gas. Based on previous measurements [30], we expect this to result in a local Fermi energy of $E_F(r=0) = 12.4 \pm 0.7$ kHz at the trap center.

Momentum-resolved rf spectroscopy data for a gas on the BEC side of the Feshbach resonance, at $B = 201.51$ G and $\frac{1}{k_F a} = 1.1$ is shown in Fig. 5.7c. For this gas, $E_F = h \times 9.3$ and $k_F = 8.6$ μm^{-1}. Here, we observe that the dispersion is clearly split into two features. The high energy feature follows the free particle dispersion (black line) and is similar to the data for a weakly interacting gas plotted in panel a. This feature is due to unpaired atoms, which far on the BEC side can be considered to be weakly interacting with each other and with the pairs. The lower energy feature is broad and negatively dispersing at all momenta. This feature is due to the pairs, which can now be considered to be in the molecular regime. The fact that the spectrum disperses downward starting at zero momentum instead of at k_F indicates that Fermi statistics do not play a significant role in the physics of the molecular gas. Furthermore, the large widths of the EDCs suggests that the single-particle excitations are extremely poor quasi-particles and the gas should not be thought of as consisting of fermionic degrees of freedom; this is consistent with the fact that we are in the molecular regime of the BCS-BEC crossover. The downward energy shift at zero momentum represents the amount of energy required to break apart a pair, and hence the pair binding energy. We measure this offset to be $h \times 28$ kHz, which is close to the measured two-body binding energy at this field of $h \times 25 \pm 2$ kHz. Because the pairing is a two-body effect, we can model the rf dissociation process and produce a Monte-Carlo simulation that shows remarkable agreement with the experimental data, (see Fig. 5.8). In this model, we assume a thermal distribution for the molecule center-of-mass motion and use the predicted distribution of relative kinetic energy

of the atoms for rf dissociation of weakly bound molecules [74]. In this simulation, the widths of the EDCs are a result of the center-of-mass motion of the molecules. See Appendix D for more information on the simulation.

5.5 Improvements to the signal-to-noise ratio

The results presented above represent some of our first attempts at atom photoemission spectroscopy and an immediate subsequent goal was to improve the signal-to-noise ratio of the data. In order to produce the intensity plots shown in Fig. 5.7, we acquire images of outcoupled atoms for a range of rf frequencies. Each image contains information relating to a parabolic cut in the spectral function (eq. 5.7). To extract that information, the momentum distribution of the outcoupled atoms must be derived from the image. The absorption image actually shows the momentum distribution projected onto a two-dimensional surface and an inverse Abel transform is required to convert this to a 3-d momentum distribution [9]. Because the momentum distribution is isotropic, we can perform an azimuthal average of the images about the center of the cloud before doing the inverse Abel transform. The signal-to-noise ratio of the images is directly related to the final signal to noise of the photoemission spectra. If we directly image the outcoupled atoms in the $|9/2, -5/2\rangle$ state using the optical transition to the $|11/2, -7/2\rangle$ excited state, the signal-to-noise ratio is poor because this is not a cycling transition. The $|11/2, -7/2\rangle$ state has a branching ratio of 0.9 to fall back into the $|9/2, -5/2\rangle$ state, which means that if an atom absorbs 7 photons it has a 50% chance of being pumped into another spin state and "going dark" (i.e. $1 - 0.9^7 \approx 0.5$). This means that to avoid saturation effects, we have to keep the average number of photons absorbed well under 7 per atom, which severely limits the signal-to-noise ratio. In contrast, atoms in the $|9/2, -9/2\rangle$ state can be imaged on a transition to the $|11/2, -11/2\rangle$ state, which is a closed transition. With this transition, we typically scatter 100 photons per atom. Therefore, it is obvious we would prefer to transfer the outcoupled atoms to the $|9/2, -9/2\rangle$ state for imaging. This can be done quite simply with two rf π-pulses that transfer the atoms in two steps, going through the $|9/2, -7/2\rangle$ state. However, there is a catch. The $|9/2, -9/2\rangle$ and $|9/2, -7/2\rangle$ states are already

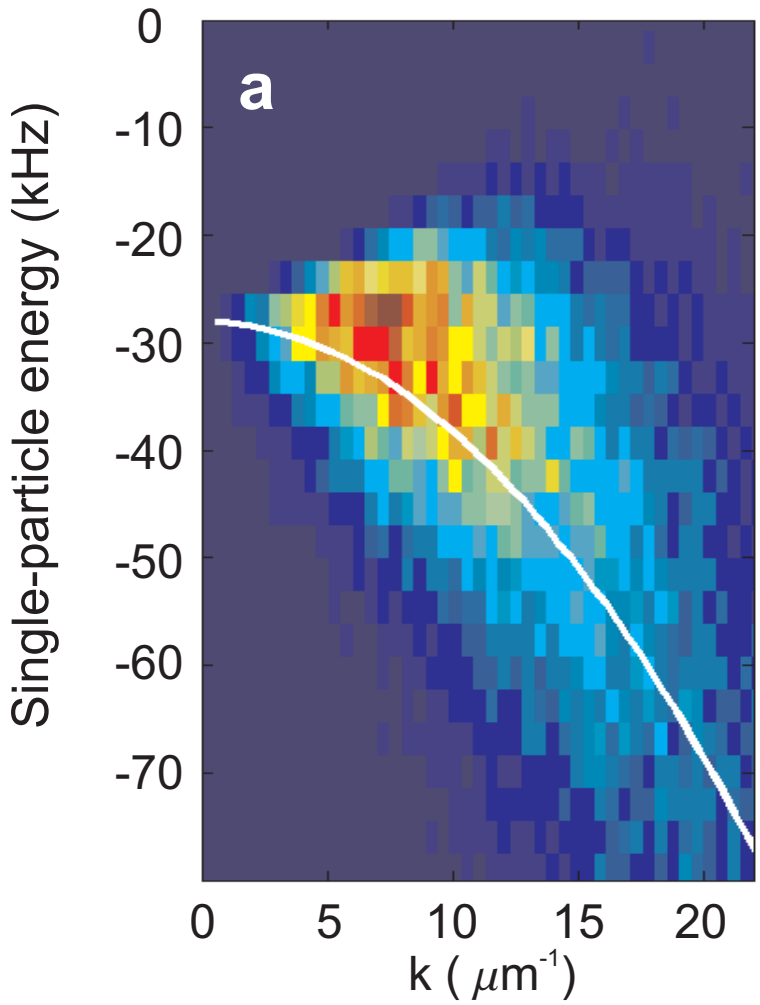

Figure 5.8: **Molecule spectrum simulation** A Monte-Carlo simulation of momentum-resolved rf spectroscopy of a molecular gas with the same conditions as Fig. 5.7 c. The white line is the fit to the data in Fig. 5.7 c. See Appendix D for more information.

populated by the atoms in the strongly interacting Fermi gas, and because we only outcouple a small percentage of the atoms in each experiment, the atoms in those states far outnumber the atoms in the $|9/2, -5/2\rangle$ state that we want to image. The rf pulses are coherent and, in principle, a perfect π pulse would completely switch the populations of the states however, a more realistic efficiency of 98% transfer would leave a large background signal. This is why we did not attempt this scheme in the original experiments.

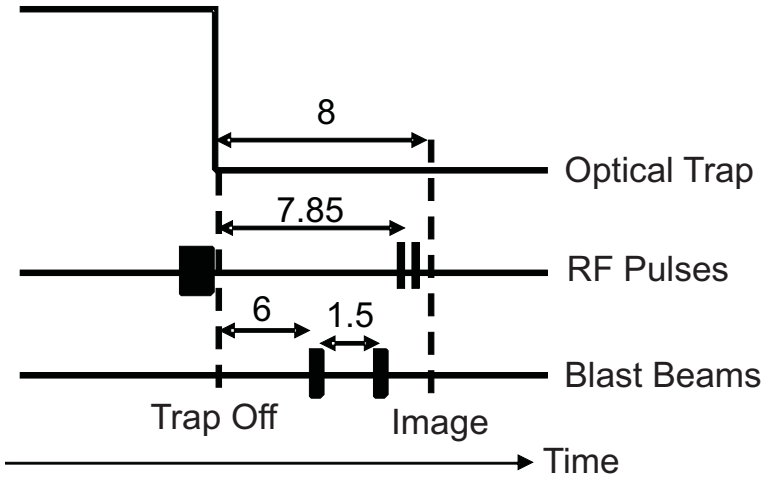

Figure 5.9: **Imaging scheme** A typical timing sequence for imaging outcoupled atoms with an 8 ms time-of-flight expansion. All times are in ms. The first rf pulse outcouples atoms from the strongly interacting system into the $|9/2, -5/2\rangle$ state and is typically 0.3 ms long. After a 6 ms wait, the first blast pulse removes atoms in the $|9/2, -7/2\rangle$ state and then a second one removes atoms in the $|9/2, -9/2\rangle$ state. Each blast pulse is typically 0.1 ms long. After the two blast pulses, two rf π pulses transfer the outcoupled atoms to the $|9/2, -9/2\rangle$ state for imaging.

The technique we later developed works by first removing the atoms in the $|9/2, -9/2\rangle$ and $|9/2, -7/2\rangle$ states with resonant light pulses. If these pulses remove 98% of the atoms and then we have an rf pulse that is 98% efficient, we get a combined efficiency of 99.96%, which is adequate for our purposes (for 2×10^5 atoms, this would leave a background of only 20 atoms, compared to the thousands we typically outcouple). The resonant light pulses must remove atoms from the desired states and not perturb the outcoupled atoms in the $|9/2, -5/2\rangle$ state. In order to accomplish this, both resonant pulses drive the atoms to the $|9/2, -9/2\rangle$ excited state. This is a σ^- transition for atoms in the $|9/2, -7/2\rangle$ state and a π transition for the $|9/2, -9/2\rangle$ atoms. These transitions are

favorable because atoms in the $|9/2, -9/2\rangle$ excited state have zero probability to fall back into the $|9/2, -5/2\rangle$ ground state. Also, the branching ratio to fall into the $F = 7/2$ ground-state hyperfine manifold is approximately 0.6, which means the atoms will only need to absorb a couple photons before they are removed to a dark state. Finally, the frequency of these transitions is not close to any transition for the $|9/2, -5/2\rangle$ ground state (see Appendix A for transitions and branching ratios). Nevertheless, we find that excessive power in these blast beams can off-resonantly excite a small percentage of the atoms in the $|9/2, -5/2\rangle$ and some of these excited atoms can fall back into the $|9/2, -5/2\rangle$ ground state with increased momentum due to the absorption and emission of a photon. This then gives an artificial contribution to the photoemission spectra. To minimize this effect, we find that the power in the removal beams should be kept only high enough to remove $95\% - 98\%$ of the atoms and that the removal should happen as close in time to the imaging as possible. The timing of the sequence is shown in Fig. 5.9. Using this imaging method, we increased the signal-to-noise rato in our images by a factor of 3 to 4. A data set taken using this imaging technique is shown in Fig. 5.10 and can be compared with Fig. 5.7b. EDC's from the data set are plotted in Fig. 5.11.

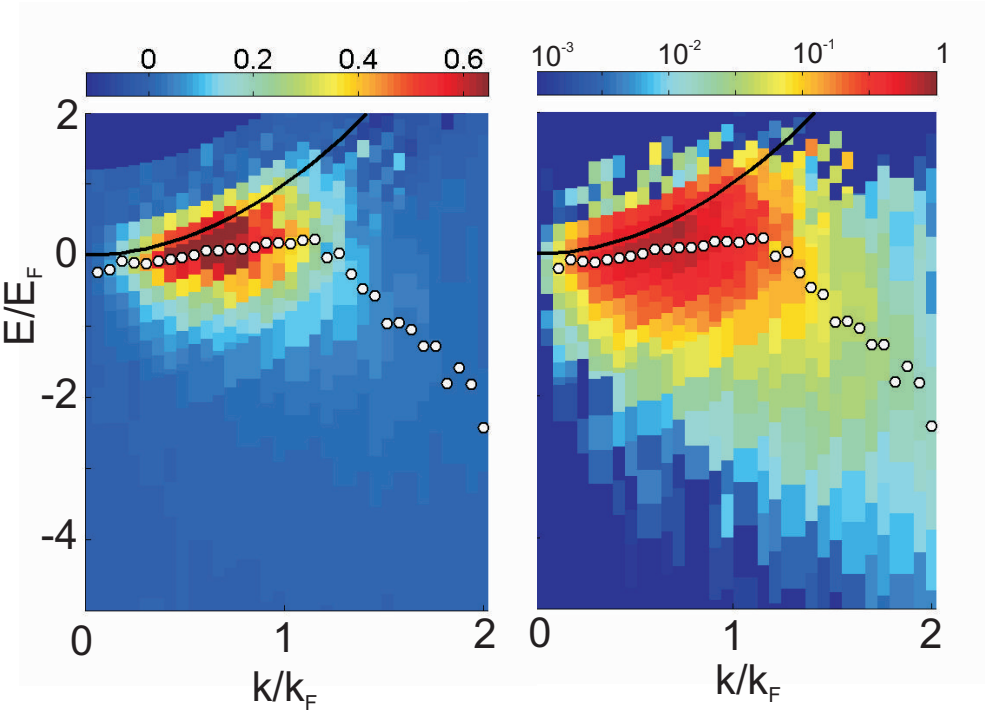

Figure 5.10: **High signal-to-noise ratio PES** Data taken with the similar conditions to the data of Fig. 5.7b using the new imaging scheme to improve the signal-to-noise ratio. On the left, the data is plotted on a linear color scale, as in Fig. 5.7b. On the right is the same data but with a log color scale to better show the data at high momentum.

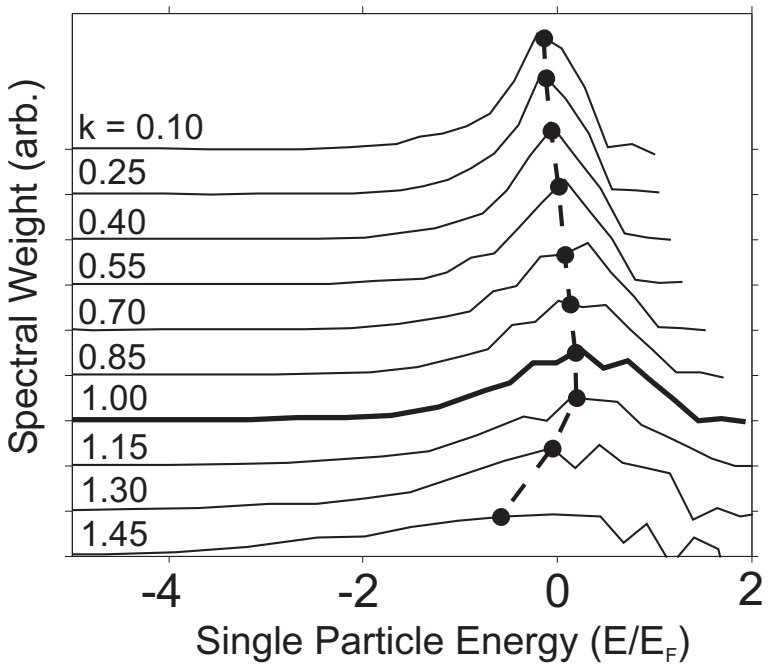

Figure 5.11: **EDCs** EDCs from the data set shown in Fig. 5.10 are plotted with values of $\frac{k}{k_F} = 0.1$ (top) to $\frac{k}{k_F} = 1.45$ (bottom). The EDC at $\frac{k}{k_F} = 1.0$ is shown in bold. Black dots indicate the centers of the gaussian fits. Each plotted EDC is the average of EDCs over a range of approximately $0.15k_F$ and has been normalized to have an area of unity.

Chapter 6

The Pseudogap state of a strongly interacting Fermi gas

In this chapter I will address the issue of the normal state of a strongly interacting gas in the BCS-BEC crossover, and, in particular, the possible existence of a pseudogap phase that arises from incoherent fermion pairs. The existence and meaning of a pseudogap phase has been a contentious issue in this field, but it is a question of utmost importance if we are to fully understand the BCS-BEC crossover and make new contributions to the field of strongly correlated systems. I will present atom photoemission spectroscopy data, both as a function of temperature and interaction strength, in order to explore the normal state in the BCS-BEC crossover and to compare to a theory of the pseudogap phase. The majority of this work is published in two articles, Refs. [18, 16].

6.1 The pseudogap phase in the BCS-BEC crossover

The ground state of a strongly interacting Fermi gas across the BCS-BEC crossover is always a paired superfluid, even if the nature of those pairs changes dramatically (consider the pair size and binding energy, for example). In contrast, the normal state, the state that exists at temperatures above the critical temperature for superfluidity, T_c, cannot be described by the same qualitative framework in both limits. In the BCS limit, which is characterized by weak attractive interactions, the normal state is a Fermi liquid, which is a state similar to a non-interacting Fermi gas but with renormalized parameters, as described in the previous chapter. In this limit, the pairs and the gap completely vanish above T_c, leaving no trace of the superfluid ground state. However, in the BEC limit, where the pair binding energy is much larger than $k_b T_c$, the normal state is a molecular gas.

Here, the pairing of the fermions is not connected to the formation of a superfluid, but rather is a result of the presence of a deeply-bound molecular state in the two-body potential. In this case, which I also refer to as the molecular regime, the pairs only dissociate at temperatures $T \approx E_b/k_b$, where E_b is the pair binding energy. It should be noted that, because there is no phase transition in the crossover, the Fermi liquid state must smoothly connect to the molecular gas in the BCS-BEC crossover.

This raises an interesting question: can only deeply bound pairs exist outside a superfluid state or might it also be possible for many-body Cooper pairs to form outside the superfluid state near the center of the BCS-BEC crossover? A state where many-body pairing exists outside the superfluid state is termed a pseudogap phase. A potential phase diagram is shown in Fig. 6.1. In the BCS state, pairing leads to the formation of two excitation branches separated by an energy gap (see Fig. 4.3) where no single-particle states exist. In the pseudogap phase, it is predicted that pairing will lead to a qualitatively similar spectral function, except that the quasi-particles will acquire energy widths and the density of states will not go all the way to zero in the gap (hence the name pseudogap) [15, 11]. The dispersion of the spectral function in the pseudogap regime can be written

$$E(k) = \mu \pm \sqrt{\left(\frac{\hbar^2}{2m}(k^2 - k_L^2)\right)^2 + \overline{\Delta}^2} \tag{6.1}$$

where the $+(-)$ is for the upper (lower) branch, k_L is the wave-vector where the two branches are at their point of closest approach (in the BCS limit $k_L = k_F$ and in the BEC limit $k_L = 0$), $\overline{\Delta}$ is the magnitude of the pseudogap, and μ determines the midpoint in energy between the upper and lower branches [15, 16].

At high enough temperatures, pairs in the pseudogap and molecular regimes will dissociate leaving a thermal Fermi gas. The temperature marking the characteristic temperature above which pairs dissociate is called T^*, and is shown as the upper dashed line in Fig. 6.1. Pairs that form above T_c are also called pre-formed pairs because they form before entering the superfluid phase. There are at least two possible definitions to mark the boundary of T^* and identify the pseudogap

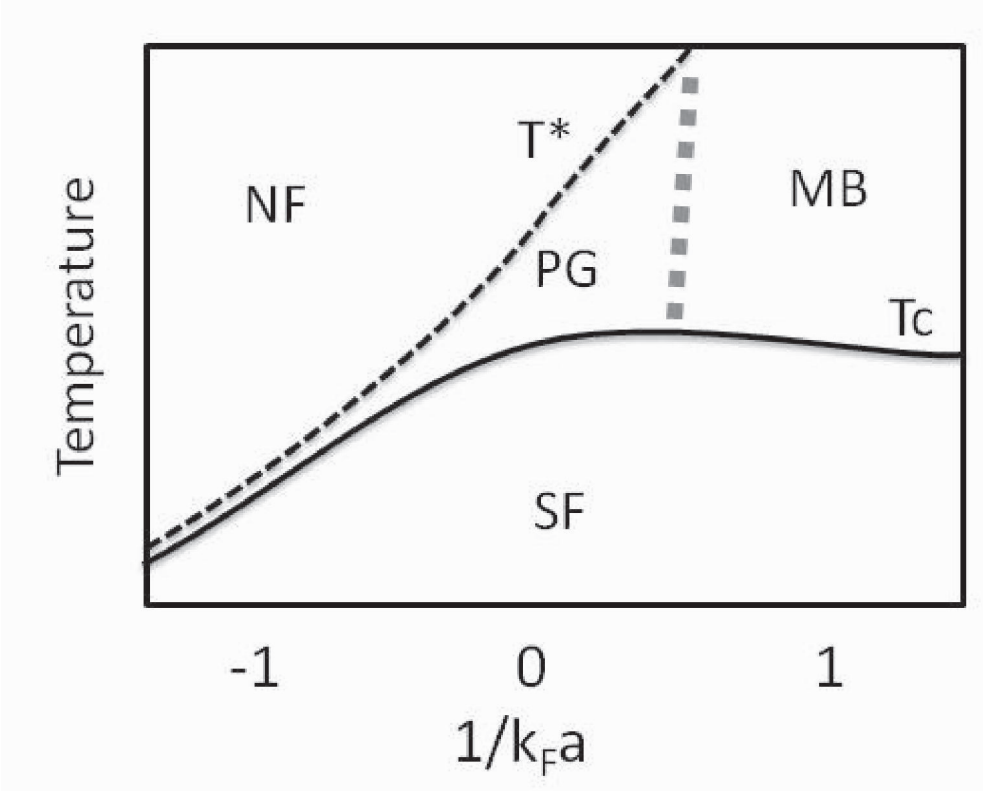

Figure 6.1: **Phase diagram of BCS-BEC crossover** This plot shows a schematic phase diagram of the BCS-BEC crossover as a function of interaction strength, $1/k_F a$ and temperature. The solid line shows the location of the critical temperature for the superfluid fluid phase transition, T_c. The thin dashed line marks the characteristic temperature for pairing T^*, which merges with T_c in the BCS limit. The thick gray dashed line marks the crossover from the pseudogap phase where many-body Cooper pairs exist to the molecular phase where the pairing is expected from the two-body physics. The phases denoted are NF for a normal Fermi liquid, PG for the pseudogap phase, SF for superfluid, and MB for the molecular regime. All of the lines except the solid line marking T_c represent crossovers and not actual phase transitions. This phase diagram is partially adopted from Ref. [11]

regime based on the spectral function [11, 75]. One definition is to look at the density of states, obtained from the spectral function by integrating over the momentum axis. A dip in the density of states near the Fermi surface would indicate the presence of pre-formed pairs and a pseudogap phase. Another definition is to look at whether the EDC at $k = k_L$ has two distinct peaks. If two distinct peaks are present this clearly indicates a pseudogap. These two definitions do not necessarily coincide and, depending on the situation, either one may lead to a higher characteristic pairing temperature T^* (see for example Ref. [11]).

Distinguishing whether the pseudogap state is mainly present in the density of states or also present in a two peaked EDC near the Fermi surface is an interesting question and may help differentiate between various theories of the pseudogap [75]. For example, theories that emphasize pairs in the pseudogap state with predominantly low momentum (extended BCS-Leggett theories) tend to predict well separated quasi-particle branches, while theories that consider pairs with a broad range of momenta (NSR type theories) tend to predict a pseudogap only in the density of states for intermediate temperatures because the large energy widths in the spectral function render the branches indistinguishable near the Fermi surface [75].

The distinction between the pseudogap phase, where many-body pairs exist, and the molecular phase where thermal molecules exist is important. In the pseudogap phase, the fermionic nature of the gas should still be apparent and, in particular, Pauli blocking must play an important role in pair formation, as in the classic Cooper pair case. Pairing in this regime is highly-non-trivial. In the molecular phase, one expects pairs simply based on the existence of a deeply bound two-body state. In this phase, the underlying Fermi statistics would not play an important role and the pairing is a rather trivial phenomenon. The crossover from the pseudogap phase to the molecular phase will be an important topic in the second half of this chapter.

In the prediction of a pseudogap phase, we have a true question about the nature of the single-particle states of the strongly interacting Fermi gas in the BCS-BEC crossover. Are those states similar to a Fermi-liquid or are they paired states? The later case would represent a break with the highly successful Landau Fermi liquid theory that has been so successful at describing

interacting Fermi gases. Either way, it is clear that these basic questions raised in the BCS-BEC crossover are questions we must address in our quest to better understand strongly interacting Fermi systems.

6.2 (Some) History of the pseudogap phase and relation to high temperature superconductors

It is interesting and useful to examine some of the history of the pseudogap phase, both in theory and experiments, and in particular the connections to the high T_c cuprates. This section is not a complete literature review of the subject, but rather a snapshot of a few interesting points.

The term pseudogap originally came from the high T_c cuprates where a number of experiments discovered anomalous properties of the normal state in the underdoped region of the hole-doped cuprate phase diagram (Fig. 6.2). Both tunneling and ARPES experiments that probed the single-particle electron structure found that a superconducting-like gap feature, the pseudogap, persisted above T_c to a much larger temperature T^*. ARPES experiments showed that the pseudogap retained the same d-wave structure as the superfluid gap and transformed smoothly into the superconducting gap [8] as a function of hole-doping. This behavior is not observed in conventional superconductors, where the gap is present only in the superconducting state, as predicted by BCS theory [5].

While no complete microscopic theory of the high-T_c superconductors exists, various phemenological theories have been proposed to explain the pseudogap phase. These theories fall mainly in either the pre-formed pairs category, which would be similar to the situation of the proposed pseudogap phase in the BCS-BEC crossover discussed above, or in the non-pairing or competing order category, where the pseudogap forms due to some other phenomenon.

In order to shed light on whether the pseudogap phase might originate from pairing, experimentalists have looked for evidence of whether the quasi-particle dispersion in the pseudogap phase resembles the BCS-like dispersion of Eq. 6.1 that originates from pairing. Experiments were done indicating that the dispersion was indeed BCS-like; with back-bending occuring near the Fermi

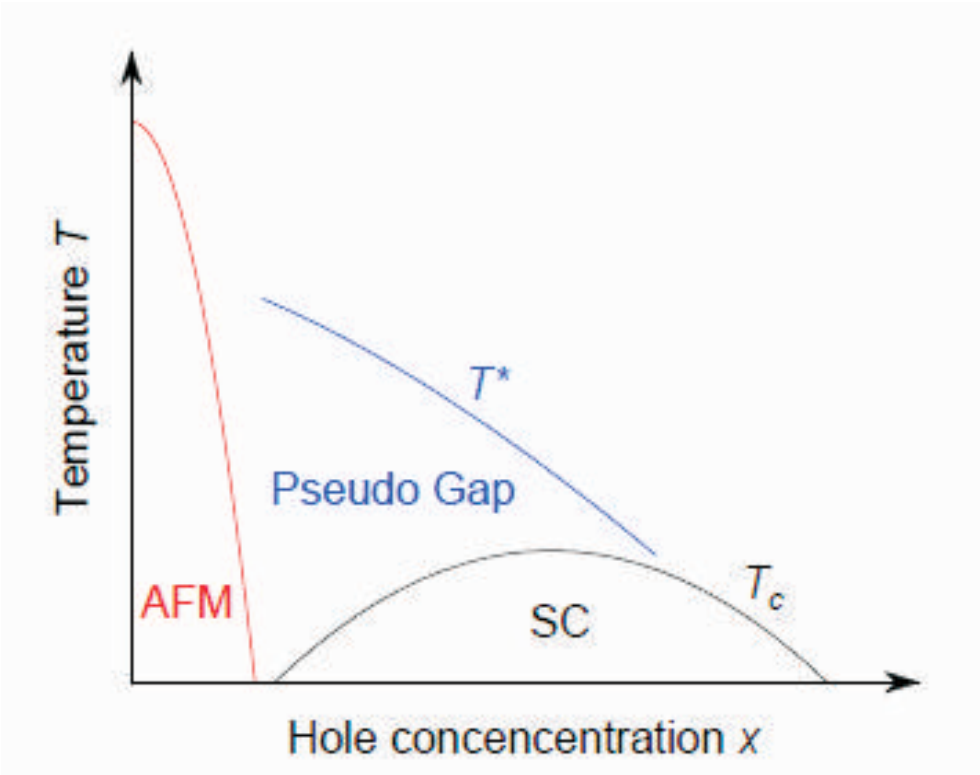

Figure 6.2: **Typical hole-doped high-T_c phase diagram** A typical phase diagram for a high-T_c superconductor as a function of temperature and hole doping. SC stands for the superconducting state and AFM stands for the anti-ferromagnetic insulator state. The superconducting phase exists for a dome-shaped region of finite hole concentration. The hole concentration where T_c is maximal is called optimally doped. The pseudogap phase exists in the temperature region of $T_c < T < T^*$ in the underdoped region of the phase diagram. Theories of the phase diagram based on the BCS-BEC crossover predict that varying hole concentration plays the role of changing interaction strength with smaller hole concentration corresponding to stronger interacting strength (and hence a larger pseudogap region) [12]. This figure is taken from Ref. [12].

surface [76], a symmetric upper branch indicating the particle-hole mixing of the quasi-particles expected from Cooper pairing [77, 78], and a smooth connection to the superconducting gap [79]. However, some of these observations are contradicted in other experiments such as Ref. [80, 81]. Ultimately, this important issue remains unresolved and highly controversial.

For the preformed pairs theory of the pseudogap, there have been many attempts to understand the pseudogap in the BCS-BEC crossover and apply that to qualitatively understand the pseudogap of the high-T_c superconductors, for example Refs. [61, 15, 12]. However, it is clear that to really model the cuprates one should take into account the two-dimensional nature as well as the lattice structure and pairing symmetry [12]. The Fermi-Hubbard model has been proposed to address these issues, however, the doped Fermi-Hubbard model remains unsolved [82].

Nevertheless, if the pseudogap in high-T_c superconductors does arise, at least in part, from pre-formed pairs due to strong pairing correlations, it is reasonable to think that we may gain some insight by studying the pseudogap regime in the strongly correlated BCS-BEC crossover. In particular, experiments of Fermi gases in the BCS-BEC crossover can confirm whether or not a pseudogap state consisting of preformed pairs can arise from strong interactions and whether that state indeed leads to BCS-like features of the spectral function. Perhaps more importantly, experiments with atomic gases in the BCS-BEC crossover can test the validity of theoretical approaches to understand the pseudogap phase in strongly interacting Fermi gases. This approach can lead to a better understanding of strongly interacting fermions and ultimately progress towards the even more difficult problem of developing a microscopic theory of the high-T_c superconductors. It is important to note that in the BCS-BEC crossover realized by atomic gases, the presence of a pseudogap state could be unambiguously attributed to pairing interactions as no other explanations exist, in contrast to the competing explanations of the pseudogap for the high-T_c superconductors.

In atomic Fermi gases, despite a large body of theoretical work on the pseudogap phase [83, 84, 85, 15, 12, 86, 87] (to name a few), there has not been convincing experimental evidence to confirm the presence of the phase in the BCS-BEC crossover, other than the work presented in this thesis. Previous rf spectroscopy experiments claimed to identify pairing above T_c, such as

Ref. [88], but these experiments turned out to be difficult to interpret and ultimately unable to distinguish between a paired and unpaired state [34].

Furthermore, recent measurements at ENS of the equation of state for a Fermi gas at the center of the BCS-BEC crossover ($1/k_F a = 0$) find a linear dependence of the pressure with $(T/\mu)^2$, which they interpret as consistent with a Fermi liquid above the critical temperature [13, 89]. The density of states near the Fermi surface determines how a system will respond to changes in temperature and thus thermodynamic measurements such as the ENS data can indirectly probe this quantity. A model of the pseudogap using a BCS-like dispersion (Eq. 6.1) with no energy width, such that a real gap exists in between the upper and lower quasi-particle branches, can be compared to the ENS data. This comparison shows that the ENS data would only be consistent with a pseudogap smaller than $0.05E_F$ [89]. However, a more realistic model of the spectral function with finite width, such that the pseudogap was partially filled in, would allow the data to be consistent with a larger value for the pseudogap [89]. Indeed, NSR theories of the pseudogap predict that the gap should become significantly filled in at temperatures above the critical temperature as shown in the inset of Fig. 6.3 (see also Refs. [11, 75]). Fig. 6.3 shows that the predicted behavior of the pressure from an NSR theory (black line) is indeed linear and consistent with the ENS data (blue circles). This also explains how the quantum Monte Carlo data from Ref. [90], which predicts a pseudogap phase, is in good agreement with the ENS data [91]. The ENS data, NSR theory, and Quantum Monte Carlo calculations indicate that thermodynamic measurements may be a poor probe of the nature of the single-particle states near the Fermi surface in the strongly interacting Fermi gas due to the large energy widths of those states [92].

6.3 Atom photoemission spectroscopy and the pseudogap phase in the BCS-BEC crossover

The ideal measurement tool for identifying the pseudogap regime would be one that had direct access to the single-particle fermion states, allowing one to directly check the density of states and properties of the spectral function. The technique of atom-photoemission spectroscopy, based on

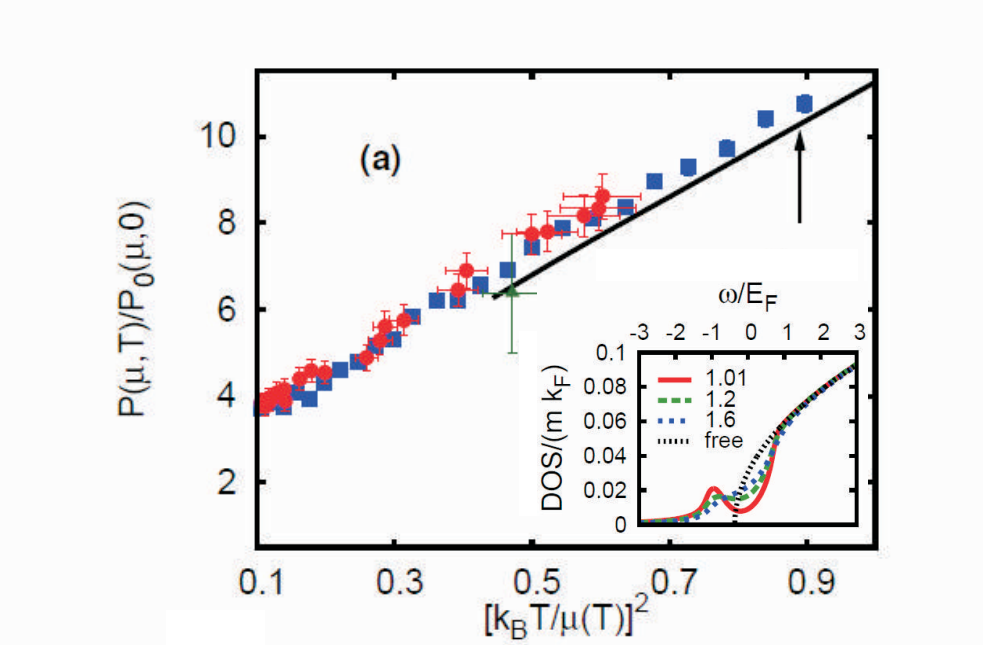

Figure 6.3: **Pressure of a normal unitary Fermi gas** Main Figure) Red circles are experimental measurements of the pressure for a homogeneous Fermi gas at $1/k_F a = 0$, obtained in Ref. [13]. Blue squares show the result of a quantum Monte Carlo calculation obtained in Ref. [14]. The black line is the prediction from a finite temperature NSR theory of the pseudogap [15, 16]. The linear behavior of the pressure in the theory, despite the existence of a pseudogap in the density of states up to temperatures as high at $T/T_c = 1.6$, demonstrates that thermodynamic measurements of Ref. [13] cannot exclude a pseudogap phase. Inset) The inset shows the density of states obtained from the same theory versus the temperature T/T_c. The black dashed curve shows the density of states for a non-interacting Fermi gas. This figure is taken from Ref. [16].

momentum-resolved rf spectroscopy, has the potential to achieve exactly that by directly measuring the single-particle spectral function. There is however one catch. Photoemission spectroscopy measures only the occupied single-particle spectral function as can be seen from the presence of the Fermi function in Eq. 5.7. To measure a gap in the density of states or to resolve the upper branch of the quasi-particle dispersion, one needs to examine the full spectral function. In principal, the full spectral function can be obtained by dividing out the Fermi function from the photoemission data if the temperature and chemical potential are known. However, this would require atom-photoemission data for a homogenous sample. In a trapped sample, as studied in the previous chapter and this chapter, the Fermi-function has a radial dependence and so cannot be divided out from trap-averaged data [16]. I will present progress towards obtaining photoemission data from a homogenous sample in the next chapter.

However, this is not to say that the trap-averaged data cannot help resolve the issue of the presence of the pseudogap in the BCS-BEC crossover. From the occupied spectral function, we will be able to examine the dispersion of the lower quasi-particle branch and look for an indication of a BCS-like dispersion with back-bending near the Fermi surface. We will also be able to compare spectral functions at different temperatures and look for evidence (or lack thereof) of a change from a paired state to a Fermi-liquid state at the critical temperature, as would be predicted by conventional BCS theory. We can also compare the trap averaged photoemission data to theories of the pseudogap state to determine if they are consistent.

In this series of experiments, we prepare an ultracold gas of fermionic ^{40}K in the $|9/2, -9/2\rangle$ and $|9/2, -7/2\rangle$ states near 203.5G as in Ref. [9]. At the end of the evaporation, we increase the interactions adiabatically with a slow magnetic-field ramp to the Feshbach scattering resonance. To vary the temperature of the cloud, we either truncate the evaporation or parametrically heat the cloud by modulating the optical dipole trap strength at twice the trapping frequency. To determine the temperature of the Fermi gas, we expand the weakly interacting gas and fit the momentum distribution to the expected distribution and extract $(T/T_F)_0$, where the subscript indicates a measurement made in the weakly interacting regime, before ramping the magnetic field

to the Feshbach resonance. For the data presented here, we obtain clouds with final temperatures ranging from $(T/T_F)_0 = 0.12$ to 0.43 with $N = 1.0 \times 10^5$ to 1.8×10^5 atoms per spin state. The trap frequencies vary depending on the final intensity of the optical trap and range from 180 to 320 Hz in the radial direction and 18 to 27 Hz in the axial direction. Correspondingly, the Fermi energy, E_F ranges from $h \times 8$ kHz to $h \times 13$ kHz, where h is Planck's constant. The Fermi energy is obtained from N and the geometric mean trap frequency, ν, as $E_F = h\nu(6N)^{1/3}$. We define the Fermi wave-vector as $k_F = \sqrt{2mE_F}/\hbar$ and the Fermi temperature as $T_F = E_F/k_B$. The energy resolution of the experiments is given by the inverse duration of the rf pulse and is equal to 2.15 kHz (rms width) or a range of $0.16 - 0.27E_F$.

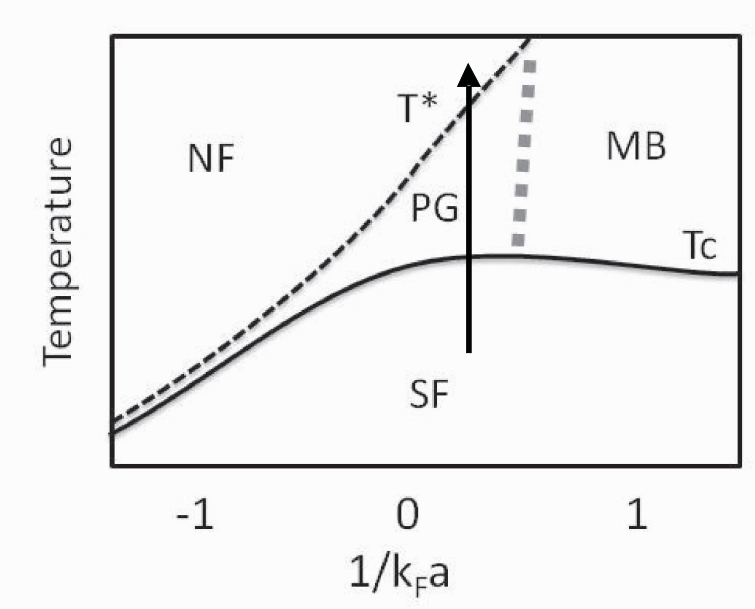

Figure 6.4: **Data in the pseudogap regime** We take data along a vertical cut (arrow) in the phase diagram at $1/k_F a = 0.15 \pm 0.03$ by varying the temperature of the gas.

The dimensionless parameter that characterizes the interaction strength for this data is $1/k_F a = 0.15 \pm 0.03$. At this interaction strength we measure the critical temperature to be $(\frac{T_c}{T_F})_0 = (0.17 \pm 0.02)$ based on the condensate fraction measurement technique [7], see Fig. 6.5. By varying the temperature, we take photoemission data along a vertical line in the phase diagram through the pseudogap region as shown in Fig. 6.4. The photomession data is shown in Fig.

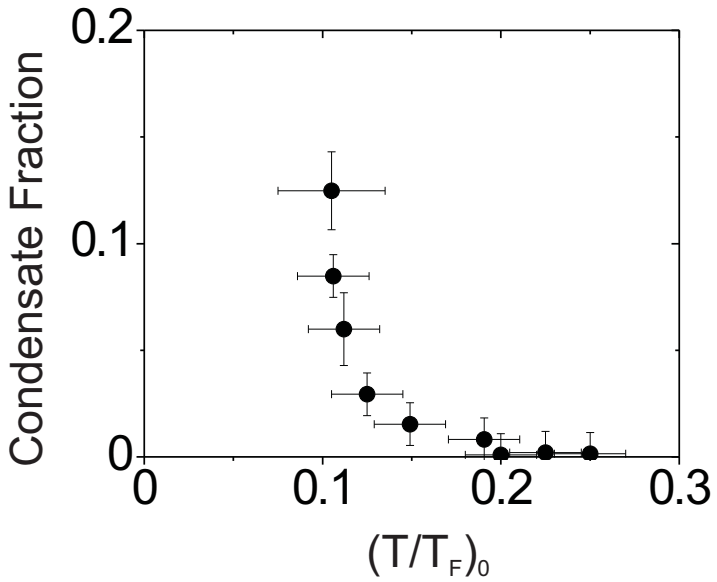

Figure 6.5: **Measuring** T_c Using time-of-flight expansion at $B = 202.1$ G, where our photoemission experiments are performed, we map out the condensate fraction. Temperature is measured in the weakly interacting regime before the adiabatic ramp to strong interactions. We find $(\frac{T_c}{T_F})_0 = 0.17 \pm 0.02$. Note that the density of the trapped cloud decreases with increasing distance from the trap center, and therefore, in a local density picture, even at $\frac{T}{T_F} = 0.17$ only the part of the gas at the very center of the trap is below T_c . The horizontal error bars represent one standard deviation of systematic uncertainty in the temperature and the vertical error bars represent a standard deviation of statistical error in the measurements.

6.6 and Fig. 6.7. In Fig. 6.6, we plot the fraction of out-coupled atoms as a function of their single-particle energy and momentum for temperatures encompassing the pseudogap regime. In the intensity plots, white dots indicate the centers derived from unweighted gaussian fits to each of the energy distribution curves, or EDCs, (vertical trace at a given wave-vector). The energy dispersion mapped out with these fits (white dots) can be contrasted to the expected free particle dispersion for an ideal Fermi gas (black curve) and are also plotted in Fig. 6.8 along with theory curves (solid lines) that are discussed below. In Fig. 6.7 we show the same data plotted as EDCs for wave-vectors ranging from $k/k_F = 0.1$ to $k/k_F = 1.4$. In order to show the evolution of the spectral function from below T_c through the pseudogap regime the data are shown for four temperatures, $(T/T_F)_0 = 0.13, 0.21, 0.25$ and 0.35, corresponding to $(T/T_c) = 0.74, 1.24, 1.47$ and 2.06.

For the data below T_c (Fig. 1a), we see a smooth back-bending that occurs near $k = k_F$, similar to what was found in the data of Fig. 5.7b and Fig. 5.10, which were taken at a slightly higher temperature but the same interaction strength. The white curve in Fig. 1a shows a BCS-like dispersion curve, Eqn. 6.1, obtained by fitting to the white dots for momenta in the range $0 < k < 1.4\,k_F$. While we cannot use this fit to extract the gap and chemical potential in a model-independent way due to the harmonic trapping confinement, the BCS-like fit is consistent with a large pairing gap, on order of E_F, consistent with the data of Fig. 5.10, and as expected for a Fermi gas near the center of the BCS-BEC crossover [6, 4].

In the case of a pairing gap, we expect the spectral function to exhibit a BCS-like dispersion with back-bending at k near k_F. For the three lowest temperatures, we observe this behavior. In fact, we observe no qualitative change from the data at $T/T_c = 0.74$ to the data at $T/T_c = 1.24$. We interpret this as strong evidence in favor of the existence of a pseudogap regime above T_c comprised of uncondensed pairs in the strongly interacting Fermi gas. The data at the highest temperature, $T/T_c = 2.06$, also displays back-bending but in a qualitatively different way. In this data, we observe a sharp kink in the dispersion (obtained from the Gaussian fits to the EDCs) at a momentum of $k = 1.5k_F$. This may seem strange because at high temperature, above T^* where no pairs exist, one naively expects to observe a purely upwardly dispersing feature. However, it turns

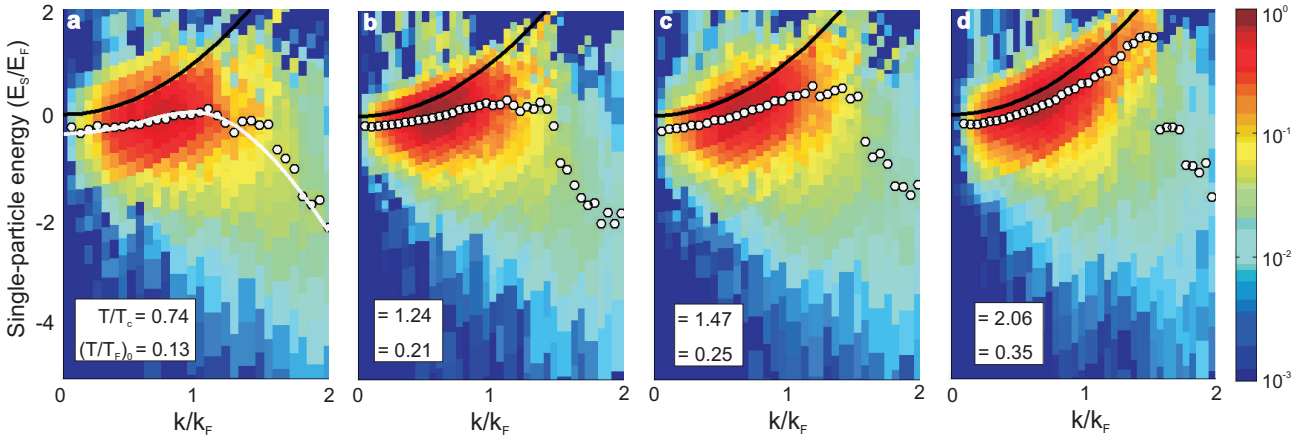

Figure 6.6: **Photoemission spectra across the pseudogap regime.** Spectra are shown for Fermi gases at four different temperatures, each with an interaction strength characterized by $(k_F a)^{-1} \approx 0.15$. The intensity plots show the fraction of out-coupled atoms as a function of their single-particle energy (normalized to E_F) and momentum (normalized to k_F), where $E = 0$ corresponds to a non-interacting particle at rest. The spectra are normalized so that integrating them over momentum and energy gives unity. White dots indicate the centers extracted from gaussian fits to individual energy distribution curves (traces through the data at fixed momentum). The black curve is the quadratic dispersion expected for a free particle. **a** At $T = 0.74\,T_c$, we observe a BCS-like dispersion with back-bending, consistent with previous measurements [9]. The white curve is a fit to a BCS-like dispersion, Eq. 6.1 **b,c** At $T = 1.24\,T_c$ and $T = 1.47\,T_c$, respectively, the dispersion with back-bending persists even though there is no longer any superfluidity. **d** At $T = 2.06\,T_c$, the dispersion does not display back-bending in the range of $0 < k < 1.5\,k_F$. In all the plots there is a negative dispersion for $k/k_F > 1.5$. We attribute this weak feature (note the log scale) to a universal property of the Fermi gas related to short-range correlations.

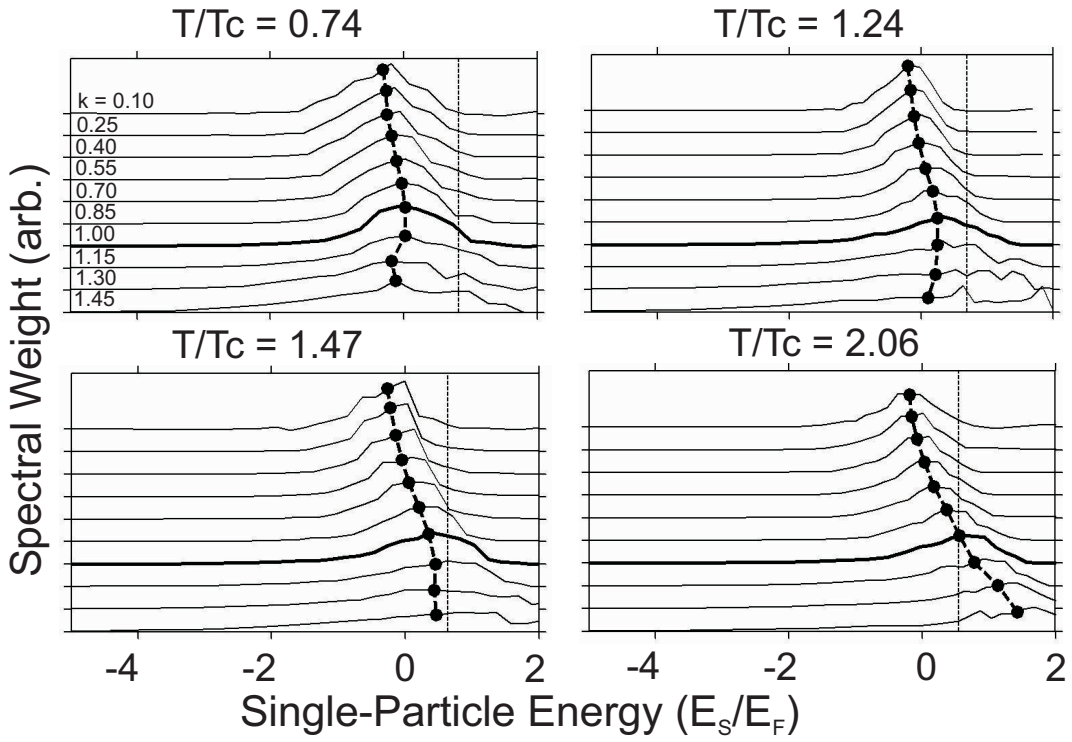

Figure 6.7: **Energy distribution curves (EDCs)** EDCs are obtained by taking vertical traces at fixed k through the photoemission spectra shown in Fig. 1. We show EDCs between $\frac{k}{k_F} = 0.1$ (top) and $\frac{k}{k_F} = 1.4$ (bottom) for the four data sets with T/T_c labeled above each figure. Each plotted EDC is an average of EDCs over a range of approximately $0.15k_F$. The EDC at $\frac{k}{k_F} = 1.0$ is shown in bold. Black dots indicate the centers of the gaussian fits to the EDCs. Each EDC is normalized to have an area of unity. Vertical dotted lines are placed at the local E_F that corresponds to the estimated average density of the gas.

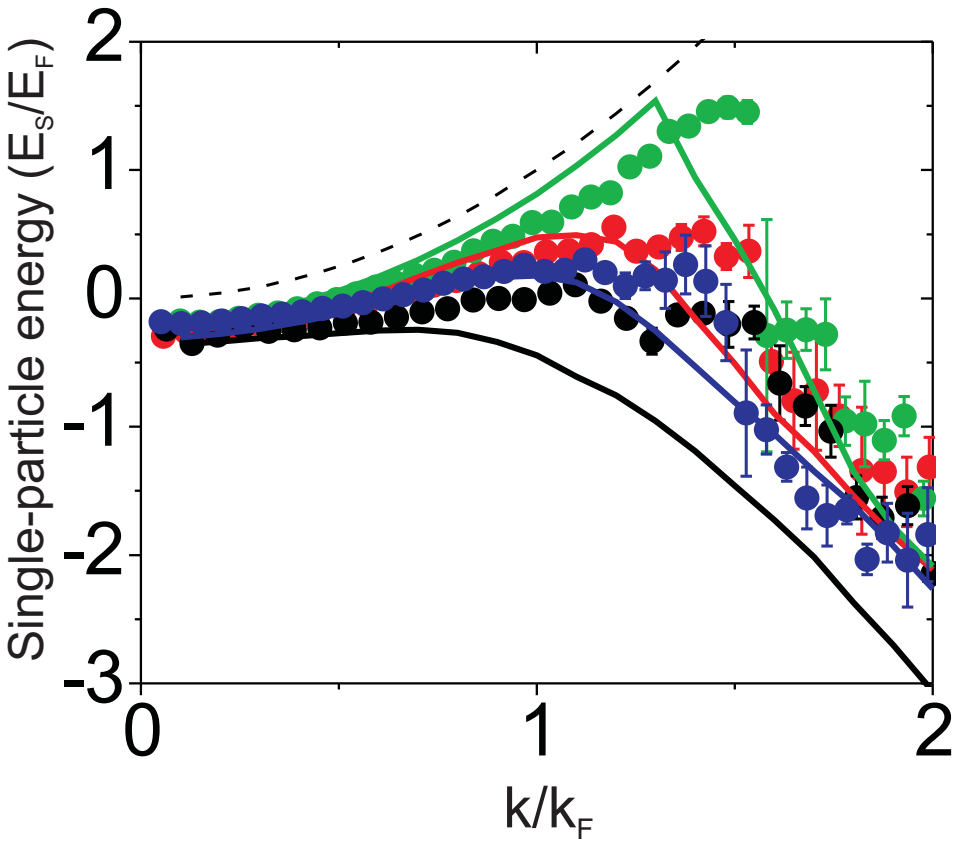

Figure 6.8: **Single-particle dispersion curves** The fits to the EDC centers are shown for the four temperatures in Fig. 6.6 and Fig. 6.7 a,b,c and d, represented by black, blue, red, and green, respectively. We observe a BCS-like dispersion, smooth back-bending near $\frac{k}{k_F} = 1$, for temperatures below and moderately above T_c. For the highest temperature, we observe a quadratic dispersion near $\frac{k}{k_F} = 1$ and a sharp discontinuity near $\frac{k}{k_F} = 1.5$. The lines are theory curves that include effects of the harmonic trap, as described in the text. The error bars on the points represent one standard deviation of uncertainty from our fits.

out that the short-range correlations between the fermions, due to the contact interaction, lead to the existence of a broad, downwardly dispersing feature at high momenta regardless of whether the system is a superfluid, Fermi-liquid, or other state, see Fig. 6.9. It should be noted that the strength of the broad, downwardly dispersing feature is dependent on the state of the system, and, moreover, the strength of the feature can be related to various other quantities in the system, such as the total energy, in a universal way. This is the subject of Chapter 8 and Ref. [10].

If back-bending is possible even in a Fermi liquid system, how can we tell whether the spectral functions in the intermediate temperature regime actually indicate pairing? First of all, as noted in the caption of Fig. 6.9, the back-bending present in a Fermi-liquid is actually the result of two separate features in the spectral function: one upwardly dispersing feature that is eventually cutoff by the Fermi function, and one downwardly dispersing feature. In this situation, one would expect a discontinuity in the fits to the EDC's as the fits jump from the upward feature to the downward feature. This should be evident both in a sharp cusp in the dispersion occurring at $k > k_F$ and a change in the amplitudes of the gaussian fits. A sharp cusp in the dispersion at $T/T_c = 2.06$ is evident in Fig. 6.6 d and Fig. 6.8 (green circles). A sharp drop in the amplitude is evident in Fig. 6.10 (green circles). For the data sets in the intermediate temperature regime, $T/T_c = 1.24$ and 1.47, we do not observe this behavior. In these data sets, the smooth back-bending of the dispersion near k_F is strong evidence for BCS-like pairing.

Furthermore, if the back-bending in the intermediate temperature regime were indeed due solely to the universal feature and not pairing one would expect the maximum energy of the occupied spectral function, E_{max}, to increase approximately proportional to the temperature of the gas as the upwardly dispersing quasi-particle branch became occupied up to higher and higher energy. We do not observe this smooth dependence as shown in Fig. 6.11. Instead, we observe a sharp increase in E_{max} for temperatures above $(T/T_F)_0 = 0.25$, where the spectral function appears to revert to Fermi-liquid like behavior. This is further evidence for a suppression in the density of states in the intermediate temperature range due to a pseudogap phase.

In Fig. 6.8, we compare our atom-photoemission spectra to a BCS-BEC crossover theory

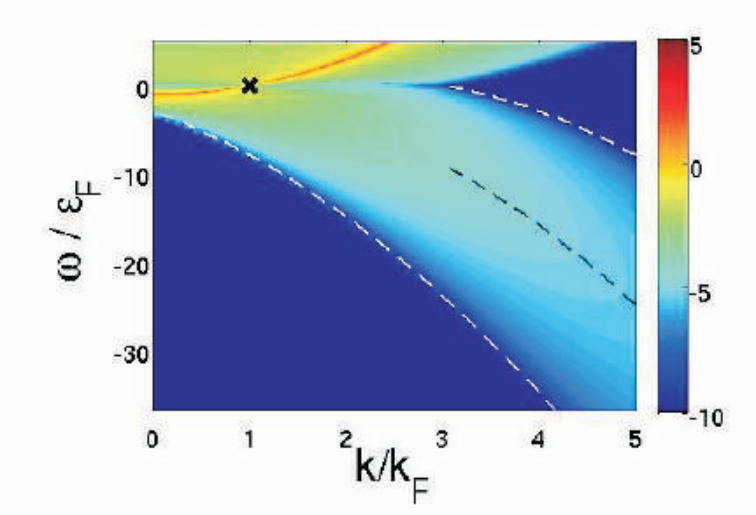

Figure 6.9: **Universal structure of an interacting Fermi liquid** A logarithmic intensity plot of $A(k, w)/(k_F a)^2$ for a Fermi liquid with repulsive interactions ($k_F a = 0.1$) taken from Ref. [17]. This figure shows both a quasi-particle branch dispersing upwards (red line) as well as a comparatively broader and weaker feature that is downwardly dispersing (black dashed line). The downwardly dispersing feature can be associated with short-range correlations due to the contact interaction that are not related to pairing [17]. In photoemission spectroscopy we measure the occupied spectral function, $A(k, w)f(w)$ where $f(w)$ is the Fermi function. The Fermi function serves as a cutoff for signal at high energy which results in the upper quasi-particle feature terminating at some finite momentum. Beyond this momentum only the lower feature will persist and the EDC's will reveal a dispersion that jumps to the downwardly dispersing feature, as seen in Fig. 6.6 d or the green curve in Fig. 6.8.

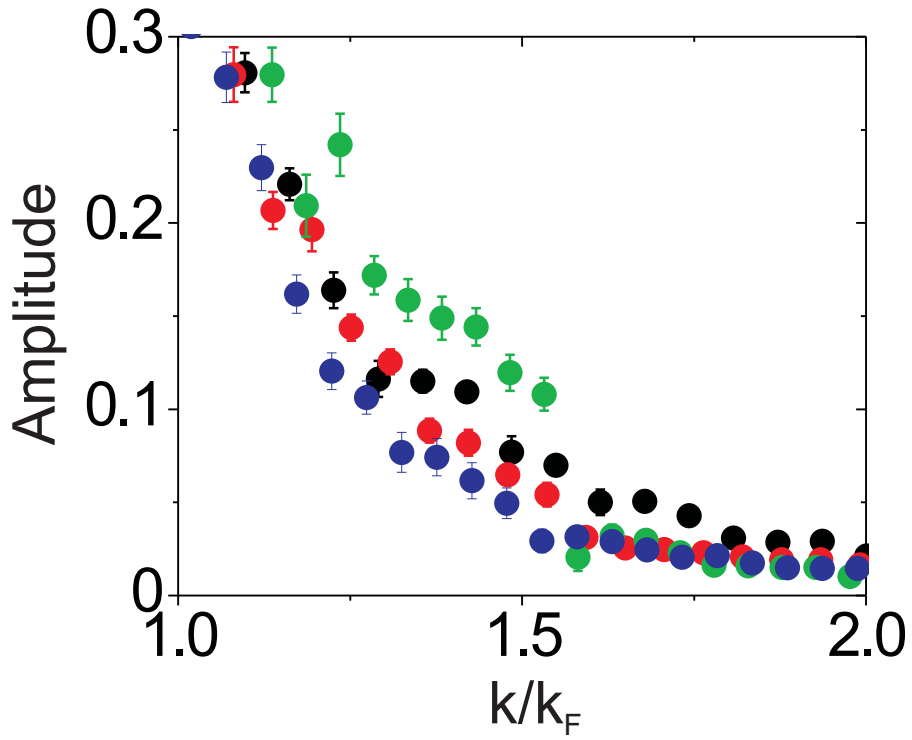

Figure 6.10: **EDC amplitudes** We show the amplitudes from the gaussian fits to the EDCs for the same experimental data as shown in Figs. 6.6,6.7, and 6.8. The fit amplitudes evolve smoothly for the lower temperatures (black, blue, and red circles in order of increasing temperature) but jump discontinuously for the highest temperature gas (green circles).

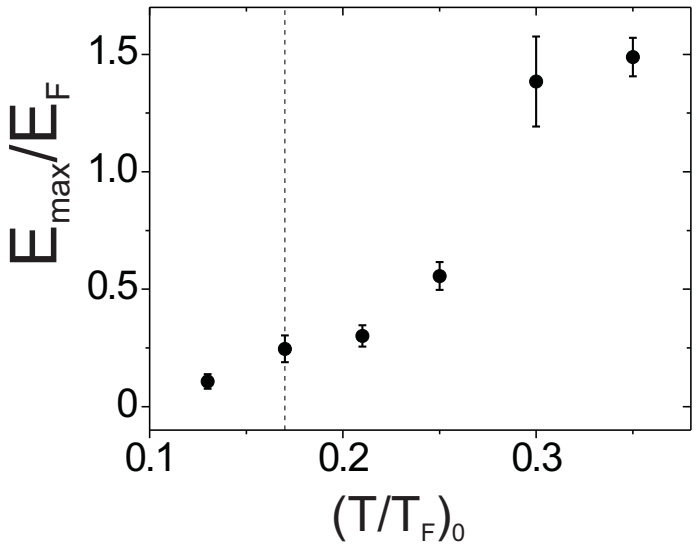

Figure 6.11: **Maximum energy of the dispersion** We show the maximum energy of the dispersion, E_{max}, for temperatures ranging from $(T/T_F)_0 = 0.13$ to $(T/T_F)_0 = 0.35$. E_{max} is the highest energy of the dispersion obtained from the gaussian fits to the EDCs. The vertical dashed line marks the critical temperature, T_c at $(T/T_F)_0 = 0.17$. There is a clear jump that occurs for temperatures above $(T/T_F)_0 = 0.25$ indicating that for temperatures below that value E_{max} is suppressed by an energy gap. In future experiments, it would be interesting to take more points in the region of $(T/T_F)_0 = 0.25$ to 0.35 to map out the sharp increase in E_{max}. From left to right: the first, third, fourth, and sixth points are from the data in Fig. 6.6 published in Ref. [18], the second point is the from the second panel on the top of Fig. 6.13 published in Ref. [16], and the fifth point, at $(T/T_F)_0 = 0.3$ is from an unpublished data set.

that is based on a diagrammatic t-matrix approximation that includes pairing fluctuations and is described in Ref. [15] (also referred to as NSR theory [75]). To compare to the experimental data, we fit theoretical EDCs to single Gaussians to extract the centers; the results are shown as lines in Fig. 6.8. The theory, which predicts the existence of a pseudogap in the density of states for the intermediate temperatures of $(T/T_c)_0 = 1.24$ and 1.47, is in excellent qualitative agreement with the experimental data. In particular, the theory lines show smooth BCS-like back-bending for the lower temperatures and a kinked dispersion for the highest temperature, $(T/T_c)_0 = 2.06$, where a pseudogap state is no longer present. We will compare predictions of the spectral function from theory to experimental data in more detail in the next section of this Chapter. For now, I will simply note that the good agreement of our data above T_c with a theory of the pseudogap is further evidence in support of the existence of a pseudogap state in the strongly interacting Fermi gas. In a similar manner, the theoretical work of Ref. [93] finds that back-bending of the trap averaged photoemission data corresponds to the existence of a pseudogap state in the center of the trap. I should also remark that other theories that have predicted a pseudogap state for the strongly interacting Fermi gas appear to at least qualitatively agree with our data, see for example Refs. [94, 72].

For temperatures below T_c, the theory [15] predicts a dispersion that is shifted to lower energy than the data. This disagreement can be attributed to a sharp variation of the order parameter with temperature close to T_c. This may suggest the theory predicts too high of an order parameter just below T_c.

6.4 Pseudogap to molecular gas crossover

To learn more about the pseudogap phase, I will present, in this section, atom photoemission data for different interaction strengths in the BCS-BEC crossover, ranging from the center of the crossover, at $1/k_F a = 0$, to well into the molecular regime, at $1/k_F a = 1.1$, at temperatures near or just above the critical temperature T_c (see Fig. 6.12). It is important to recall that at $T = T_c$ only the very center of a trapped atom gas is actually at the critical temperature, and the vast majority

of atoms should be considered to have a temperature above the local T_c. Thus, the photoemission data presented here probe the pseudogap regime. Furthermore, by investigating this region of interaction strengths, we will probe the crossover from the pseudogap state, where the underlying fermionic properties of the system remain important, to the molecular regime where the pairing can be considered primarily a two-body effect. We will see that the value of the wave-vector, k_L, (see the pseudogap dispersion 6.1), which determines where the two quasi-particle branches are at their point of closest approach, can characterize whether a gas is in the pseudogap or molecular regime. A value of k_L near k_F will indicate the presence of a remnant Fermi surface, indicating the importance of the fermionic nature of the system. In the molecular regime, k_L approaches 0. I will also show detailed comparisons of the data to the NSR theory of Ref. [15], which predicts this behavior of k_L. The experimental data and theory comparisons are in Ref. [16].

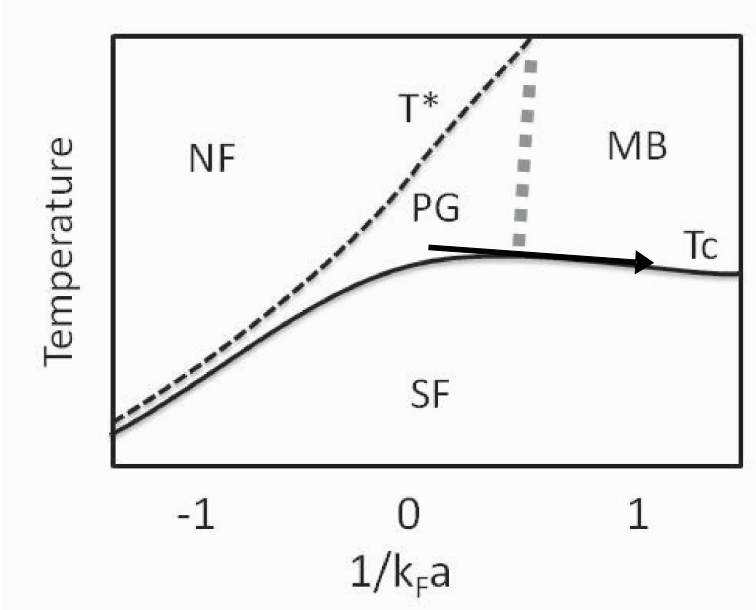

Figure 6.12: **Data taken near T_c in the pseudogap and molecular regime** We take data near T_c for different interaction strengths ranging from $\frac{1}{k_F a} = 0.0$ to 1.1. This region is the heart of the pseudogap phase and the crossover to a molecular phase.

The photoemission data is shown in Fig. 6.13. Some general observations regarding the data can be made immediately. In the data sets at $1/k_F a = 0.45$ and higher, two distinct spectral

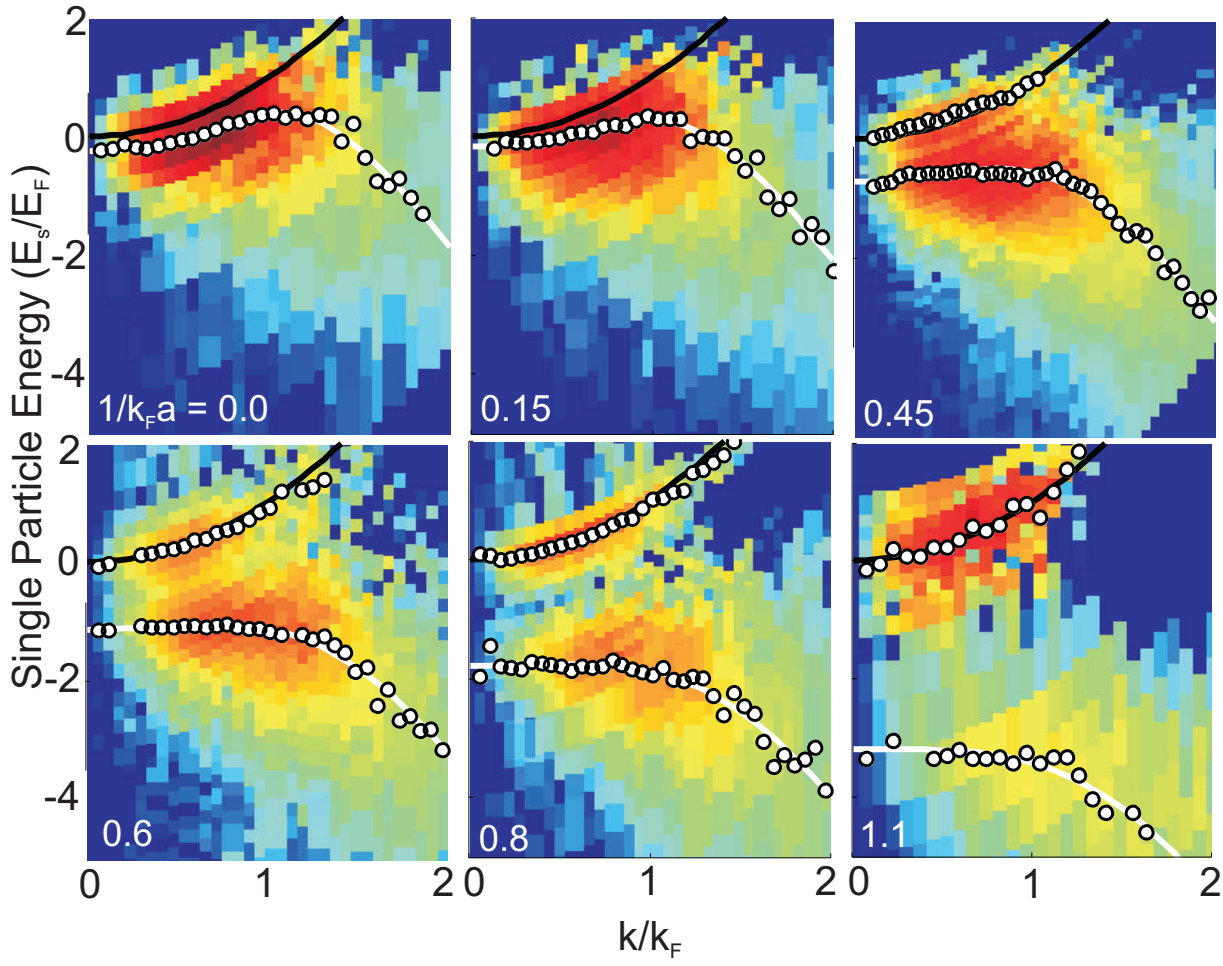

Figure 6.13: **Photoemission spectra near T_c in the pseudogap and molecular regime** The six panels show data taken at different interaction strengths, parameterized by $1/k_Fa$, and $T/T_c = 1.0 \pm 0.1$, (see Fig. 6.12). The interaction strengths span the center of the pseudogap regime to the molecular regime. The black line is the free particle dispersion and the white dots are obtained from Gaussian fits to the EDCs. In the first two data sets ($1/k_Fa = 0.0$ and 0.15) only a single spectral feature is resolved and so the fits are single Gaussians. In the other four data sets ($1/k_Fa = 0.45, 0.6, 0.8$ and 1.1) two spectral features are resolved and the fits are double Gaussians. The white lines are fits to the back-bending spectral features with Eq. 6.1.

features become distinguishable with the higher feature being upwardly dispersing and close to the free-particle dispersion. Furthermore, as the value of $1/k_F a$ is increased, the lower feature shifts downwards and changes shape to become flatter and eventually monotonically decreasing in the molecular limit.

These general features can be interpreted as follows. In the molecular limit, unpaired fermions are weakly interacting and so should have a spectral function identical to a weakly interacting Fermi gas. It has been previously found that in this temperature range, the conversion of atoms to molecules after a magnetic-field sweep from the BCS to BEC limits is only 75% efficient, see Ref. [95]; and so we expect a finite number of unpaired atoms to contribute to the photoemission signal. Because the three-body recombination rate is relatively slow in our gas, these unpaired atoms can be out of chemical equilibrium with the molecules. This explains the upwardly dispersing feature that follows the free-particle dispersion in the data sets closest to the molecular limit ($1/k_F a = 0.8$ and 1.1). As for the data sets closer to the pseudogap regime, such as the spectrum at $1/k_F a = 0.45$ and $1/k_F a = 0.6$, it might seem surprising to observe a spectral feature near the free-particle dispersion, as we expect the atoms in this regime to be strongly interacting. However, it is important to recall that this photoemission data is for a trapped gas and that atoms at the edge of the cloud will be at low density, and hence weakly interacting, regardless of the scattering length. Thus, the spectral feature near the free particle line observed in data sets in the strongly interacting regime are likely due to atoms at the edge of the cloud, see for example Ref. [93].

In the spectra nearest to the center of the crossover, $1/k_F a = 0.0$ and 0.15, only one spectral feature is observed. However, in this situation the lower branch of the spectral function is close enough to the free particle line that the contribution from weakly interacting atoms at the edge of the cloud cannot be clearly resolved. For data sets in the strongly interacting regime, in addition to weakly interacting atoms at the edge of the cloud, one might expect some signal due to unpaired atoms near the center of the cloud, where they would be strongly interacting. These excitations would be similar to the quasi-particles we derived in the BCS theory and would have a dispersion different from the free-particle dispersion, see Fig. 4.3. However, we expect the presence of the

Fermi function in the photoemission signal, Eq. 5.7, to suppress any contributions from quasi-particle excitations. Furthermore, near the Fermi surface, where quasi-particles are most easily excited, the two branches of the spectral function may not be resolved due to the large energy widths of the quasi-particles [75, 16, 11]. The inhomogenous density introduced by the trapping potential and signal from atoms at the edge of the cloud would further serve to obscure any sign of the upper quasi-particle branch. These reasons may also explain why the upper branch of the quasi-particle dispersion is not observed in data taken at higher temperature, (see Fig. 6.6).

The changes in the dispersion of the lower spectral feature that we observe as a function of $1/k_F a$ are important. The shift of the dispersions to lower energy for increasing $1/k_F a$ is due to the increasing binding energy of the pairs as we cross into the molecular regime. Perhaps more interestingly, the shape of the dispersion also changes in the data. Near the center of the crossover, in the data at $1/k_F a = 0.0$ and 0.15, the dispersion is qualitatively similar to the BCS quasi-particle dispersion, Eq. 4.8, with an increasing dispersion at low momenta and back-bending occurring near the Fermi surface $k/k_F = 1$. Back-bending near $k/k_F = 1$ signifies that Fermi statistics still play an important role in the gas and indicates that the back-bending dispersion is caused by many-body Cooper pairs. As we approach the molecular regime with larger values of $1/k_F a$, we observe that the dispersions flatten and eventually become purely downwardly dispersing, as expected for molecules, see Fig. 5.8. Here, Fermi statistics do not play an important role and $k/k_F = 1$ is no longer a special point.

The point where back-bending occurs is determined by the parameter k_L in Eq. 6.1. The value of k_L extracted from BCS fits to the data (white lines in Fig. 6.13) is shown in Fig 6.16. The molecular regime should be marked by a two-body molecular binding energy greater than the temperature, leading to the formation of pairs in the absence of many-body effects. The two-body pair binding energy compared to the Fermi energy is given by $E_b/E_F = 2(k_F a)^2$ (see Eq. 3.9) and this can be compared to the approximate critical temperature of $(T/T_F)_0 = 0.17$, which is given in terms of the temperature of the gas before the adiabatic ramp to strong interactions. We find that $E_B/k_B T_F = 0.0, 0.05, 0.41, 0.72, 1.28$ and 2.42 for the data sets shown in Fig. 6.13.

6.5 Comparisons to a theory of the pseudogap

In this section, we compare the data of Fig. 6.13 to a theory of the pseudogap introduced in Ref. [15]. This theory predicts a pseudogap in the density of states over a wide range of temperature and interaction strength for a gas in the BCS-BEC crossover [75, 15, 11] (see inset of Fig. 6.3). For comparison with the trap-averaged data of Fig. 6.13, EDCs are produced by taking theoretical spectra for homogenous gases and averaging them over predicted density profiles of the gas, which are obtained from the same theory. For details of the theory, I refer the reader to Refs. [15, 16].

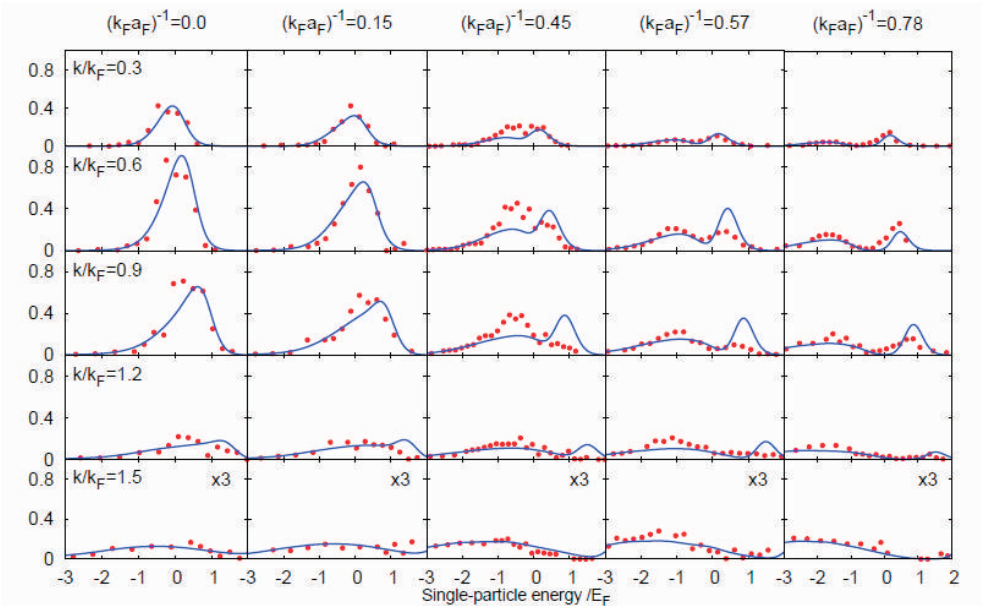

Figure 6.14: **Comparison of experimental and theoretical EDCs** Here we plot experimental EDCs (red circles), obtained from vertical cuts through the first 5 data sets of Fig. 6.13, and the corresponding theoretical EDCs (blue lines) from an NSR theory based on Ref. [15]. This figure is taken from Ref. [16]. See text for discussion.

The comparisons of the EDCs can be seen in Fig. 6.14. The dispersions and energy widths obtained from the EDCs are shown in Fig 6.15. A first remark that can be made regarding Figs. 6.14 and 6.15 is that the theory reproduces the amplitude, center, and energy widths of the experimentally measured EDCs quite well. This suggests that the spectral functions produced by NSR-type theories [75, 15, 11] capture the essential physics of the pseudogap regime in the BCS-

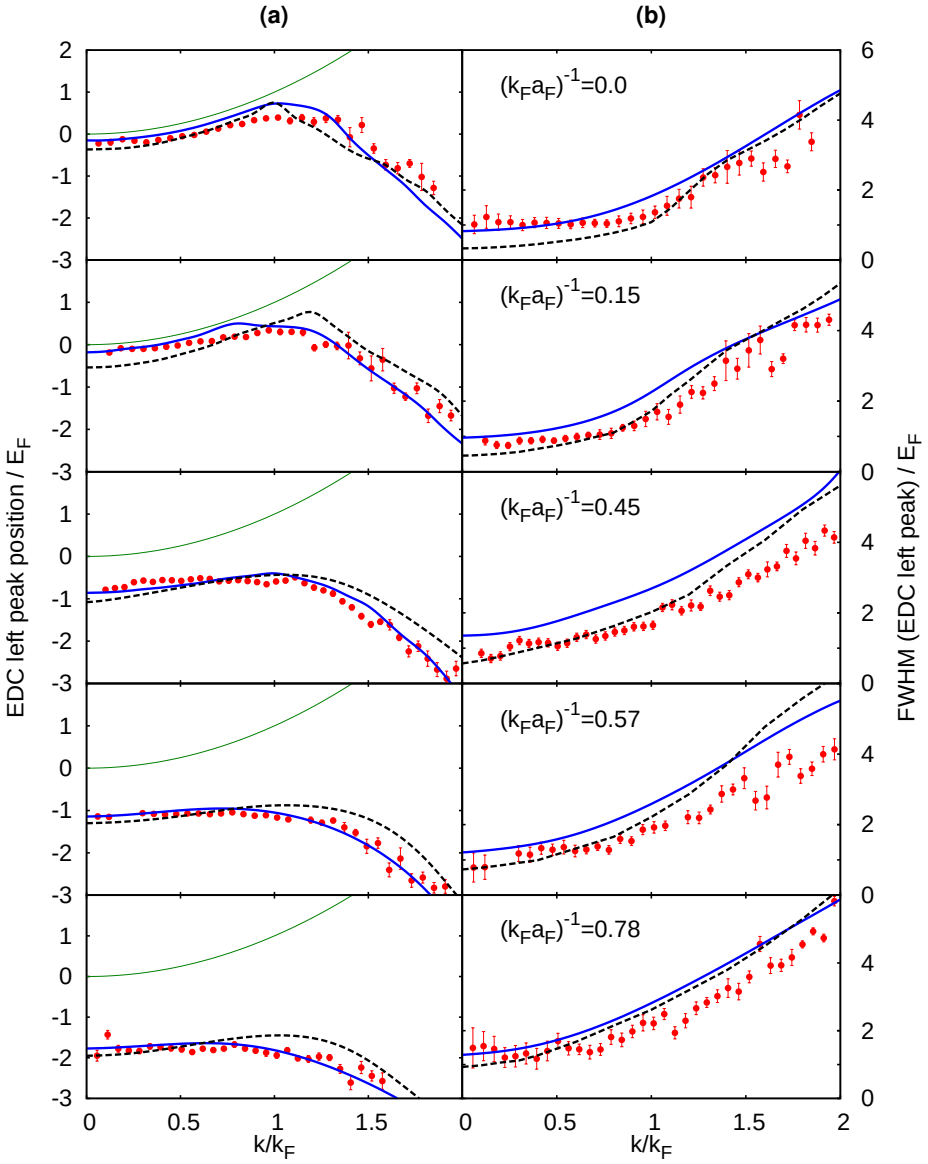

Figure 6.15: **Comparison of experimental and theoretical dispersions and widths** (a) We plot dispersions (red circles) obtained from unweighted Gaussian fits to the EDCs of the backbending feature (left peak) of the data in Fig. 6.13. Solid green lines mark the free-particle dispersion. (b) We plot the widths (full width at half maximum), shown as red circles, that are obtained from unweighted Gaussian fits to the EDCs of the backbending feature (left peak) of the data in Fig. 6.13. Blue lines are obtained from the theoretical spectra, shown in Fig. 6.14, that include the effects of trap averaging. Dashed lines are obtained from theoretical spectra for a homogeneous gas with density equal to the predicted average density of the trapped gas. This figure is taken from Ref. [16]. See text for discussion.

BEC crossover. The theory also confirms that the parameter k_L decreases rapidly in the area of the crossover from the pseudogap regime to the molecular regime and marks the disappearance of a remnant Fermi surface in the strongly interacting gas, as can be seen in Fig. 6.16.

In some of the data sets in Fig. 6.14, it is clear that the theory and experiment disagree on relative weight of the upper and lower peaks. However, this relative weight is very sensitive to the temperature and chemical potential. As such, the discrepancy is not surprising since the theory overestimates T_c by approximately 30% [16].

Given that the theory reproduces the essential features of the data, we can ask the question, what does the theory tell us about the effect of trap averaging? To investigate this, dispersions and energy widths obtained from theoretical EDCs for a homogenous gas with a density equal to the average density of the trapped gas are shown as dashed lines in Fig 6.15. From this we can make a few remarks. Both a homogeneous gas and the the trapped gas show similar qualitative features. In particular, the BCS-like shape of the dispersion with back-bending at the wave-vector k_L is not affected by the trap. Furthermore, Fig. 6.15 shows that the large single-particle excitation energy widths, which are on the order of the Fermi energy, near the Fermi surface, do not appear to be caused by the trapping potential but, according to the NSR theory are actually intrinsic energy widths. This would imply the gas is far from the regime of a Fermi liquid where single-particle excitations at the Fermi surface correspond to narrow energy peaks in the spectral function and can be treated as weakly interacting quasi-particles [68].

Fig. 6.17 shows that, according to this NSR theory, the fact that we can map out a single back-bending dispersion for the entire range of momenta $k/k_F = 0$ to 2.0 is actually due to the suppression of high energy states from the Fermi function in the photoemission signal, Eq. 5.7. In the full spectral function predicted by the theory, the upper and lower branches are only distinguishable at low ($k/k_F < 0.9$) and high ($k/k_F < 1.5$) momenta and the two branches merge into a single broad feature near the Fermi surface (see also Refs. [75, 11]). It is important to note that, along with the existence of two distinguishable branches (with similar spectral weight) at low and high momenta, the spectral functions obtained from NSR theory contain a dip in the density of

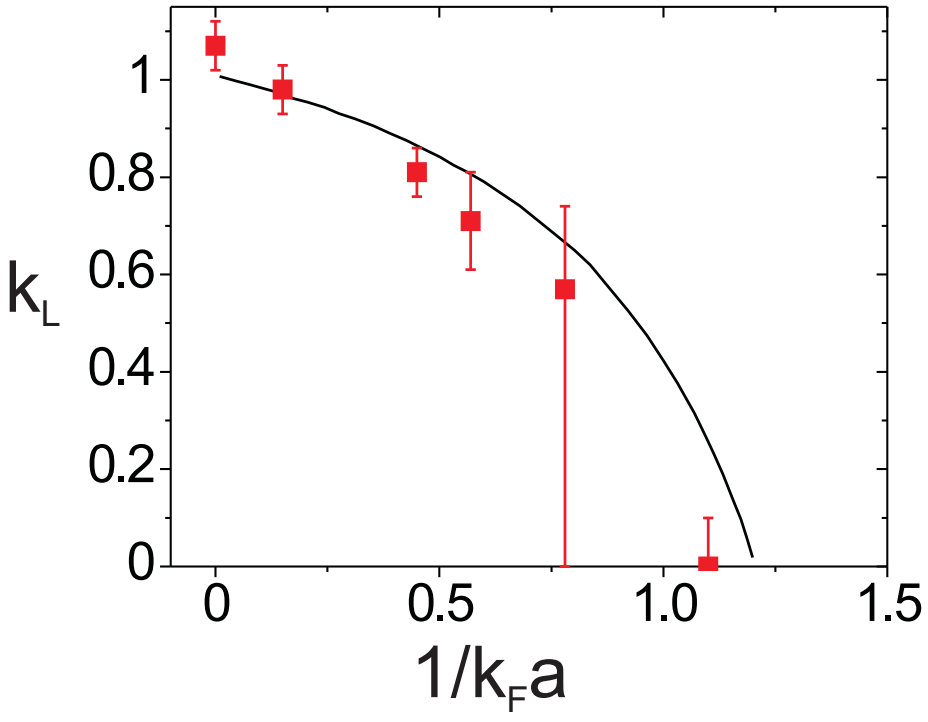

Figure 6.16: **Comparison of experimental and theoretical** k_L The value of k_L (Eq. 6.1) obtained from theoretical dispersions (black line) and from the data (red squares). This figure is taken from Ref. [16]. See text for discussion.

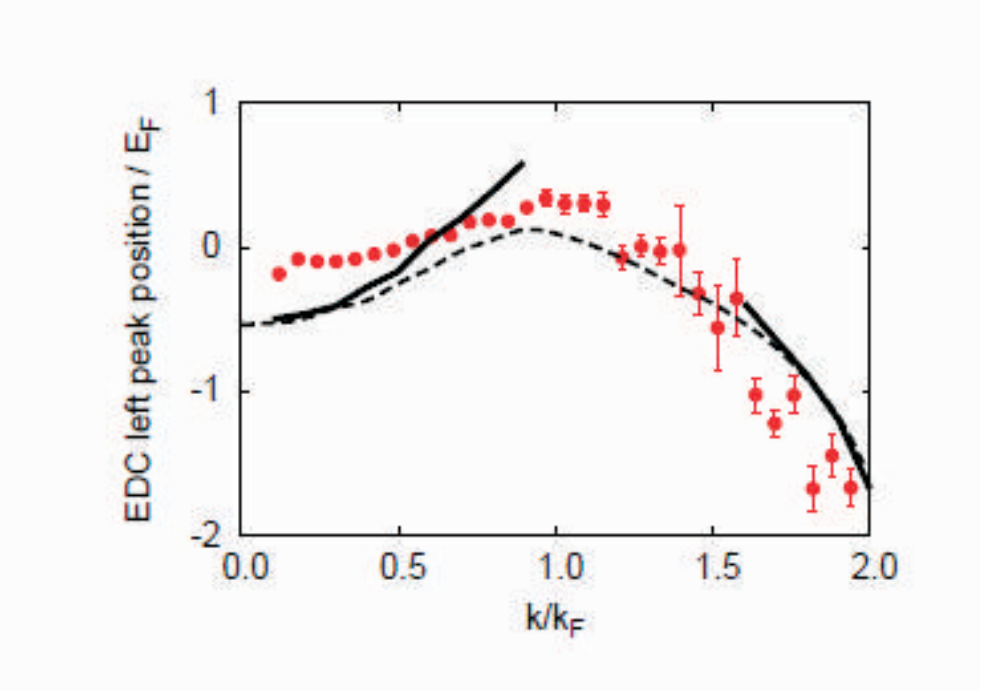

Figure 6.17: **Dispersion with and without Fermi function at** $1/k_F a = 0.15$ The plot shows the experimental dispersion obtained from trap averaged photoemission data at T_c at $1/k_F a = 0.15$ (red circles). The dashed line is obtained from a theoretical prediction for a homogeneous gas with density equal to the predicted average density of the atom cloud. The black line is obtained from the theoretical prediction but without the inclusion of the Fermi function. The black line thus traces out the dispersion of the lower branch in the full spectral function. In the region of $(0.9 < k/k_F < 1.5)$ the two branches of the dispersion cannot be distinguished due to the large energy widths. This figure is taken from Ref. [16].

states at the Fermi surface due to a pseudogap, see Fig. 6.3 inset.

6.6 Extracting information from BCS-fits to the spectral functions

Fits to the experimentally obtained dispersions using the expected pseudogap dispersion, Eq. 6.1, are shown as white lines in Fig. 6.13. The functional form of Eq. 6.1 obviously matches the data very well. However, it is not clear if the best fit values of the parameters are particularly meaningful. After all, the photoemission spectra are obtained for trap-averaged data where the gas does not have a well-defined value for the gap and chemical potential due to the density inhomogeneity. Furthermore, we obtain the dispersions from gaussian fits to the EDCs, but the intrinsic EDCs may have a different functional form and could be asymmetric. Another complication is that any excitations due to finite temperature will tend to pull the gaussian fits of the EDCs to higher energies. For all these reasons, it is difficult to directly extract a value for gap (or pseudogap) and chemical potential from these fits.

However, the fits qualitatively capture three important features in the dispersions that are predicted by theory. As a function of increasing $1/k_F a$, we observe that the wave-vector where back-bending occurs shifts to lower momentum. This is clearly captured by the parameter k_L and is discussed in the previous section. We also observe that the dispersions shift to lower energy with increasing $1/k_F a$. This reflects a decrease in the chemical potential, which gives a constant energy offset in the dispersion given by Eq. 6.1. Also, with increasing $1/k_F a$, the dispersions become flat over a larger range of k near k_L, which gives an increase in $\overline{\Delta}$. The values obtained in the fits are shown as red circles in Fig. 6.18 and both of these features can be observed.

However, the values obtained for μ and $\overline{\Delta}$ are larger than the expected values for a zero temperature homogeneous gas, which are shown as stars in Fig. 6.18 and are obtained from Refs. [20, 19, 21]. This may seem counterintuitive since the density inhomogeneity due to the trap means that most of the cloud will have a lower density and presumably smaller values of the gap and chemical potential. This can be understood by considering the effect that atoms at low density will have on the data. Atoms at low density are weakly interacting and thus contribute spectral signal

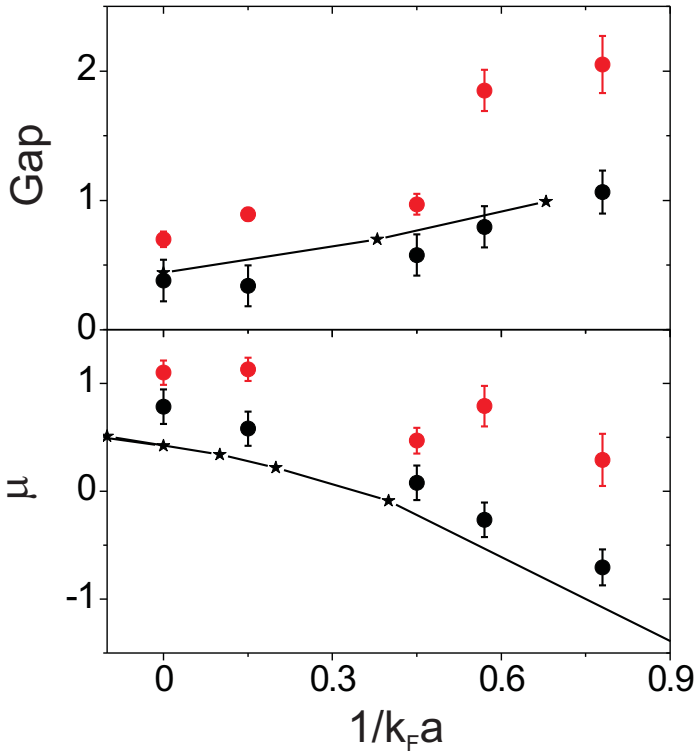

Figure 6.18: **BCS fits** Top) Red circles show the values of $\overline{\Delta}$ obtained from fits to the data in Fig 6.13 using Eq. 6.1. The error bars are due to uncertainty in the fits. Black circles show the value of $\overline{\Delta}$ obtained by taking half the distance between E_{max} and the free-particle line as described in the text and in Fig. 6.19. For these points I have included an additional systematic error due to the uncertainty in E_{max} from error in the calibration of the magnetic field. Both the red and black circles are values of $\overline{\Delta}$ in units of the Fermi energy for the trapped gas, which is obtained from the total number and trap frequency (Eq. 2.4). The stars show the value of the gap for a homogeneous gas at zero temperature, inferred from momentum-integrated rf spectra, in units of the Fermi energy of the homogenous gas (Eq. 2.2) [19]. The line is a guide to the eye. Bottom) Red circles show the values of μ obtained from fits using Eq. 6.1. Black circles show the values given by the midpoint of E_{max} and the free-particle line. The stars show the values of μ for a homogeneous gas at zero temperature obtained from Refs. [20, 21].

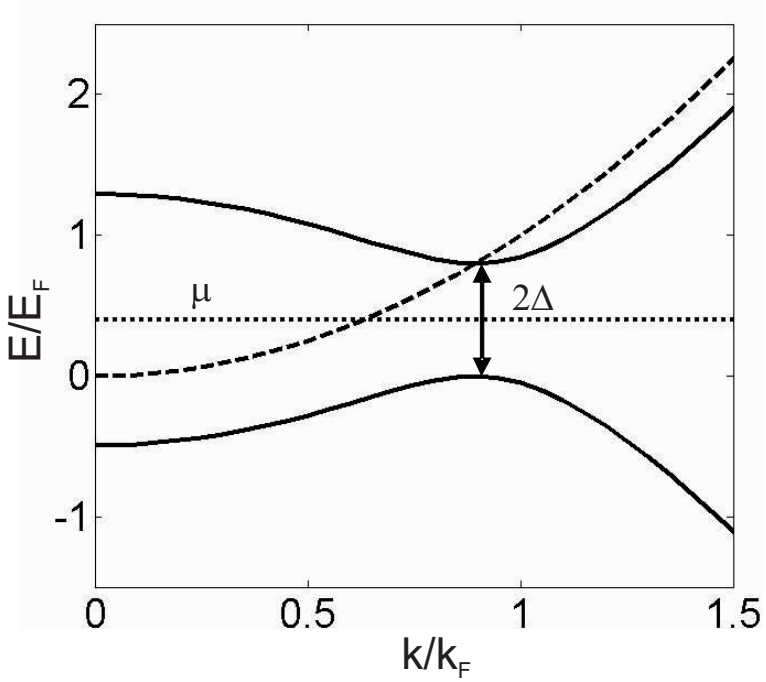

Figure 6.19: **Extracting the gap and chemical potential** In this example, the minimum of the upper quasi-particle branch intersects the free-particle dispersion line $\frac{\hbar^2 k^2}{2m}$. This occurs when $\mu + \Delta \approx k_L^2$. If this case, we can estimate the gap and chemical potential from the maximum energy of the lower quasi-particle dispersion. The gap will be half the distance between this maximum energy and the free-particle line. The chemical potential will be the energy halfway in between the maximum of the lower dispersion and the free-particle line. In this example, values used are $\mu = 0.4$, $\Delta = 0.4$ and $k_L\sqrt{0.8}$, which are very close to the values predicted for a zero temperature gas at $1/k_F a = 0$ [19].

close to the free-particle line. Furthermore, because the local value of k_F is also smaller, atoms at low density contribute signal at low momenta. This has the effect of pulling the trap-averaged dispersions to higher energy for small k/k_F. This shift to higher energy leads to larger values of μ and a flattening of the dispersion that gives larger values of the gap Δ. This at least partly explains why the values obtained from the fits to Eq. 6.1 for μ and $\overline{\Delta}$ are larger than expected.

An alternative approach for extracting μ and Δ from the data is to use information about the position of the upper branch for quasi-particle excitations. The upper and lower branches of the dispersion are symmetric about μ and separated by a minimum energy of $2\overline{\Delta}$ (Fig. 6.19). In the BCS limit, where the chemical potential is equal to the Fermi energy, the minimum of the upper branch is above the free particle line ($\frac{\hbar^2 k^2}{2m}$) by an energy equal to the gap. In the molecular limit, the upper branch is simply the free-particle line, since unpaired atoms are weakly interacting. Interestingly, theoretical predictions and measurements based on rf spectra [20, 96, 19] put the minimum energy of the upper quasi-particle branch at $1/k_F a = 0$ within $0.01E_F$ of the free-particle dispersion. Since both at resonance and in the molecular limit, the minimum of the upper quasi-particle branch touches the free-particle line, it is a reasonable assumption that the minimum of the upper branch is near the free-particle line in the range of interactions strengths examined in this chapter, $0 < 1/k_F a < 1.1$. The gap can then be estimated from half the distance between the measured maximum of the lower branch and the free-particle line, and the chemical potential can be estimated by taking the energy halfway in between that maximum and the free-particle line (Fig. 6.19). The values obtained for μ and $\overline{\Delta}$ using this analysis are shown in Fig. 6.18. While this analysis technique does not resolve the problem of density inhomogeneity, it does appear to lead to a better estimation for μ and $\overline{\Delta}$ than the parameters extracted directly from fits to the data with Eq. 6.1.

The value of the maximum energy of the lower dispersion is best obtained by reparametrizing Eq. 6.1 using $E_{max} = \mu - \overline{\Delta}$ such that $E(k) = E_{max} + \overline{\Delta} - \sqrt{\left(\frac{\hbar^2}{2m}(k^2 - k_L^2)\right)^2 + \overline{\Delta}^2}$. While fits to the data using Eq. 6.1 suffer from a strong correlation between the gap and chemical potential parameters, the values obtained for E_{max} are robust and not strongly correlated with the other fit

parameters; this may reduce systematic errors.

6.7 Conclusions

At this point, we can summarize a few conclusions that can be made from the photoemission experiments presented thus far. The data reveal a BCS-like back-bending dispersion in the normal state over a large range of temperatures ($T/T_c = 1.0 - 1.5$) and interaction strengths ($1/k_F a = 0.0 - 1.1$). At higher temperatures ($T/T_c > 1.5$), we observe a spectral function consistent with theories of a Fermi liquid with short-range interactions (Fig. 6.9). As a function of interaction strength, we observe a crossover from a pseudogap regime where the dispersion back-bends at the Fermi wave-vector ($k_L \approx k_F$), indicating the existence of a remnant Fermi surface, to the molecular regime where $k_L = 0$. The crossover occurs in the range of $1/k_F a \approx 0.45 - 0.8$. A comparison to a finite temperature NSR theory of the BCS-BEC crossover reveals good agreement and provides further evidence for the existence of pseudogap phase. In addition, the theory gives an indication that the presence of a trapping potential does not qualitatively alter the features of the photoemission spectra. In particular, this serves as evidence that the large energy widths of the single-particle excitations that we observe may be intrinsic widths, indicating an absence of quasi-particles in the strongly interacting gas. Finally, while the NSR theory of the pseudogap is consistent with linear behavior observed in recent thermodyanmic measurements [13] (Fig. 6.3), theories based on an extended BCS-Leggett theory, for example Refs. [12, 75], that predict a strong dip in the density of states and relatively narrow energy widths are probably not consistent with the ENS data [89]. The excellent agreement of our data with the NSR theory of the pseudogap serves as further evidence that the spectral function in the pseudogap regime, in the range of interaction strengths investigated here, is likely dominated by single-particle excitations with large energy widths, possibly caused by pairs with large center-of-mass momentum [75], and thus a density of states with a gap that becomes significantly filled in above T_c.

So far our experimental evidence for the pseudogap state is : BCS-like back-bending of the trap-averaged occupied spectral function (Figs. 6.6 and 6.13), the non-linear behavior of E_{max} (Fig.

6.11) and the strong agreement with a theory of the pseudogap phase in the BCS-BEC crossover (Fig. 6.14). The inhomogenous density of the atomic gas, which is a consequence of the trapping potential, prevents us from directly measuring the pseudogap by dividing out the Fermi function in the photoemission data. In the next chapter, I will present progress towards photoemission spectroscopy of a homogenous sample. This data provides further evidence for the existence of a pseudogap regime and single-particle exctitaions with anomalously large energy widths.

Chapter 7

Towards atom-photoemission spectroscopy of a homogeneous gas

In the previous chapters, I have presented atom-photoemission data for a trapped gas, which necessarily has a spatially inhomogeneous density. This inhomogeneity can lead to broadening of spectral features and makes it impossible to divide out the Fermi function from the photoemission data. Spatial inhomogeneity can also be an issue for ARPES experiments on electronic materials containing impurities, non-uniform doping, or a non-uniform chemical potential. However, there is one major advantage of the trapped gas compared to an ARPES experiment with a non-uniform material, which is that the density profile of the gas is smooth and can be predicted and measured. This means we can still compare to theories, via a local density approximation. We can also predict some of the general features we expect to arise due to the inhomogeneity, such as an increased spectral weight near the free-particle dispersion due to weakly interacting atoms near the edge of the gas. Also, importantly, every trap-averaged sample we study is identical, as opposed to different material samples.

In the last chapter, I showed that we can obtain a significant amount of information about the spectral function in the BCS-BEC crossover from trap-averaged photoemission data. Here, we examined qualitative features of the data and also compared to a theory of the crossover. However, it is clear that photoemission spectra of a homogeneous atomic gas would be very useful. In particular, one would like to measure the energy widths for the homogeneous gas, and the dispersion of the quasi-particles. In addition, for data on a homogeneous gas, one could divide out the Fermi function and measure the gap or pseudogap in the density of states. Ultimately,

photoemission data obtained from a homogeneous sample would allow for more sensitive tests of theories of the crossover and advance our goals of developing a better understanding of strongly interacting Fermi gases.

In this chapter, I will present progress towards photoemission spectroscopy of a homogeneous cloud. Unfortunately, the obvious solution of creating a uniform trapping potential, or box trap, instead of a harmonic trap, turns out to be technically very difficult. In particular, it would be difficult to make a box trap small enough to achieve the same atom densities obtained in the harmonic trap. Instead, we tried a different approach, which would allow us to keep the harmonic trap, but remove photoemission signal arising from atoms at the edges of the cloud. We refer to this approach as the hollow light beam method (or, around the lab, as the donut beam method). The data provide further evidence that the energy widths of quasi-particles near the Fermi surface are a significant fraction of the Fermi energy as well as show what the effect of the inhomogeneous density is on the quasi-particle dispersions. The work presented in this chapter will be the subject of forthcoming publications.

It should be noted that other experiments have shown it is possible to obtain momentum-integrated rf-spectra for a homogeneous Fermi gas by imaging the atoms transferred by the rf field in-situ, without a time-of-flight expansion [97]. However, it is not possible to use this technique for photoemission spectroscopy, which requires momentum information that can only be obtained by time-of-flight imaging. Rather, we needed a technique that would give both spatial selectivity and momentum information for the atomic gas.

7.1 Focusing on the center of the cloud

The method of using hollow light beams to investigate effects of density inhomogeneity is based on the idea that removing atoms at low density leaves behind a sample that is more homogeneous. This can be seen from Fig. 7.1, which shows the atom density as a function of scaled radius from the cloud center (a), and the number of atoms in the cloud as a function of scaled atom density (b) for a zero temperature Fermi gas in a harmonic trap. If we can remove atoms at low density,

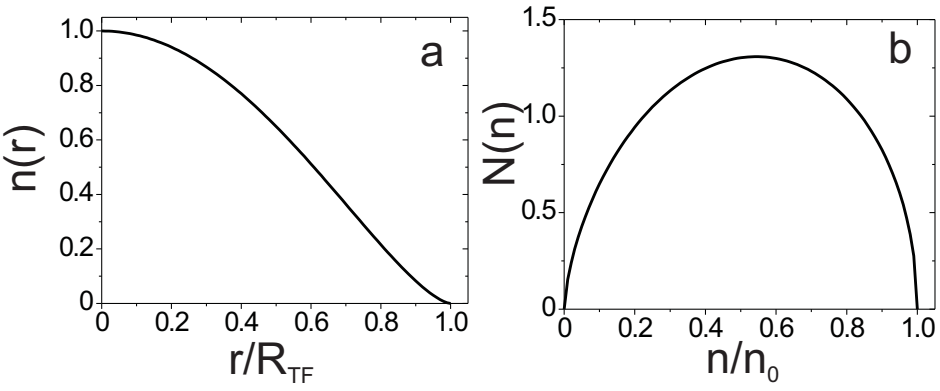

Figure 7.1: **Atom density distribution of a trapped Fermi gas** a) The radial density profile of a $T = 0$, harmonically trapped Fermi gas. r/R_{TF} is the scaled radius, where each component (x,y,z) is divided by the Thomas Fermi radius in that direction. The total number of atoms at a given radius is $4\pi n(r)r^2dr$. b) The number of atoms in the cloud at a given density n/n_0 is plotted, where n_0 is the density at the center of the cloud. There are, of course, 0 atoms at $n/n_0 = 0$ and also 0 atoms at density $n/n_0 = 1$, because this corresponds to a singular point at the center of the cloud. The average density of atoms is approximately $n_{avg}/n_0 = 0.51$ and the median density is 0.54.

we will be left with a distribution of atoms that has a higher average density and less variation in density. This can be done by removing atoms at large radius. In the limit where one removes all the atoms except just those at $r = 0$, the remaining gas would be completely homogeneous with a density equal to the peak density of the original atom cloud. Unfortunately, there would also be no atoms left. Instead, we use the hollow light beams to remove $30 - 70\%$ of the total atoms, and thereby significantly decrease the number of atoms at low density.

The hollow light beams remove atoms by optically pumping them to another spin state that interacts only weakly with the atoms in the spin states we are interested in. When we take a picture of the gas, only the atoms that have not been optically pumped will show up. The hollow light beam is dark in the center, and focused onto the cloud, and so will have no effect on atoms at the center of the cloud. We require two (cylindrical) intersecting hollow light beams in order to remove atoms at the edges of the three-dimensional cloud. Laguerre-Gaussian beams, with a profile in the far-field given by

$$I(r) = I_0 r^{2l} e^{\frac{-r^2}{2w^2}} \tag{7.1}$$

where l is the order of the beam and w is the waist, are obtained using absorption masks patterned with a forked diffraction grating with l dislocations, see for example Ref. [98].

The atom cloud is cylindrically symmetric with a Thomas Fermi radii (given by $R_{TF} = \frac{1}{\omega}\sqrt{\frac{2E_F}{m}}$) of approximately 10 μm and 125 μm in the radial and axial directions, respectively. For these experiments, we use a hollow light beam with $l = 1$ and $w = 11$ μm propagating along the axial direction to remove atoms in the radial directions and a beam with $l = 2$ and $w = 90$ μm propagating perpendicular to the axial direction to remove atoms in the axial direction. Fig. 7.2 shows the atom removal probability as a function of scaled radius.

7.1.1 Optical pumping

Because we are interested in measuring the momenta of the remaining atoms, it is necessary for the optical pumping to be highly efficient. If an atom absorbs a photon from a hollow light beam and then returns to the initial state, instead of being optically pumped out, it will have an

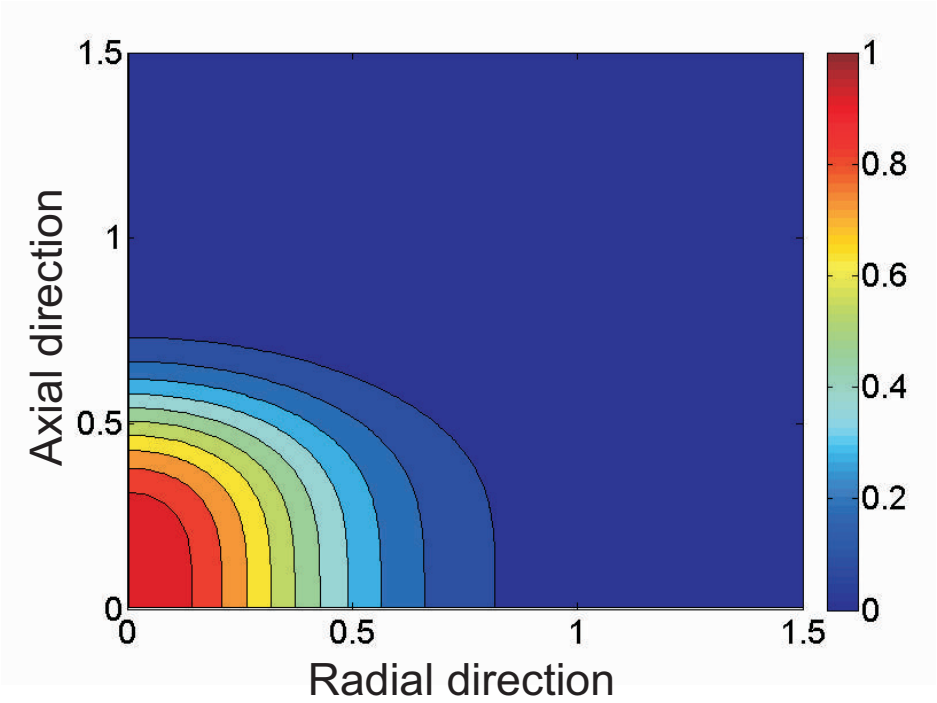

Figure 7.2: **Atom removal probability** The surface plot shows the probability for atoms to remain after optical pumping with the hollow light beams as a function of scaled radius in the radial direction and in the axial direction. The radii are scaled to the Thomas Fermi radii in those directions. The color map shows the probability to remain, with red corresponding to high probability to remain and blue corresponding to high probability to be optically pumped and removed from the imaging. Integrating over all radii, approximately 65% of the atoms in a degenerate Fermi gas would be optically pumped.

increased momentum due to the photon recoil. To make matters worse, the photon recoil, $\hbar k$ where $k = \frac{2\pi}{\lambda}$, is approximately equal to a typical Fermi momentum $\hbar k_F$ in our experiments. In order to minimize this, we choose the hollow light beams to be resonant with transitions to excited states that have small branching ratios to decay back into the initial state.

In this work, we have tried two different transitions, both resonant with the $|9/2, -5/2\rangle$ ground state that we use for the atom photoemission experiments. One transition uses the $|9/2, -7/2\rangle$ electronically excited state. This state has a 0.02 probability to decay back to the $|9/2, -5/2\rangle$ ground state, or in other words, only a 1 in 50 chance. The downside for this transition is that 3 MHz away there is a π transition ($\Delta m_F = 0$) to the $|9/2, -5/2\rangle$ excited state, which has a 0.6 branching ratio for decay back to the $|9/2, -5/2\rangle$ ground state. The higher branching ratio also means the π transition is stronger and easier to excite. As a result, a small error in the polarization of the hollow light beam can cause significant excitations with the π transition, and this results in poor optical pumping. The second transition we tried is to the $|5/2, -3/2\rangle$ excited state. This state has a slightly larger branching ratio back to the original state (0.095), however, there are no other nearby transitions that can be off-resonantly excited.

With either transition, we still have to worry about a small number of atoms that absorb a photon from one of the hollow light beams and then fall back into the $|9/2, -5/2\rangle$ ground state with an increased momentum. Increasing the power of the hollow light beam does not help with this issue because the center of the beam is dark, and so there will always be a region where the intensity of the beam is such that atoms will only absorb a single photon on average (the probability that an atom will absorb two photons and still remain in the same state is negligible for both transitions). The size of this region can be made smaller by using beams parameterized by larger values of l. However, the limited resolution of our optics delivery system prevents us from effectively using a beam with $l > 1$ for the beam with the 11 μm waist.

The number of atoms that will absorb a photon and fall back into the same state with a changed momentum can be modeled using the radial profiles of the atom cloud and light beams. We find that these atoms typically correspond to $5 - 10\%$ of the total number of atoms that remain

(see Fig. 7.3, or Appendix B for details). These atoms are an undesirable background signal. To subtract out the background, we model the momentum distribution of these atoms by convoluting the momentum distribution of the atoms that absorbed light from the hollow light beams with a spherical shell of momentum of momentum $\hbar k$, where k is the amplitude of the photon wave-vector. We find the measured size of the background signal is approximately equal for both possible transitions, despite the difference in branching ratios.

7.2 Application to a weakly interacting Fermi gas

As a first application of the hollow light beams, we can measure the momentum distribution of atoms at the center of a quantum degenerate, weakly interacting trapped Fermi gas. The momentum distribution of weakly interacting fermions is described by the Fermi-Dirac distribution (remember all the way back in Chapter 2 Eq. 2.3). The hallmark of the Fermi-Dirac distribution is a sharp Fermi surface at wave-vector k_F. At zero temperature, the distribution is characterized by the full occupation of momentum states below k_F and zero occupation above. At finite temperature, the distribution near the Fermi surface becomes smeared over a region of k-states spanning an energy width on order of $k_b T$. However, in a trapped Fermi gas, the Fermi surface is not apparent in the momentum distribution. This can be understood from a local density approximation. The wave-vector marking the Fermi surface of a homogeneous Fermi gas (Eq. 2.1) depends on the fermion density, which in a trapped gas varies as a function of distance from the trap center. A trapped gas can be thought of as a collection of Fermi gases, each described by a different value of k_F. When we measure the momentum distribution of all the atoms in the trap, we average together Fermi-Dirac distributions parameterized by values of k_F ranging from 0 (corresponding to atoms at the edge of the trap) to the maximum value of k_F (corresponding to atoms at the center of the trap). In fact, the shape of the momentum distribution is identical to the density distribution [33] (this is a special feature of harmonically trapped gases) and looks like Fig. 7.1 a) with the x-axis as atom momentum.

If we could measure the momentum distribution of a select group of atoms in the trap, ones

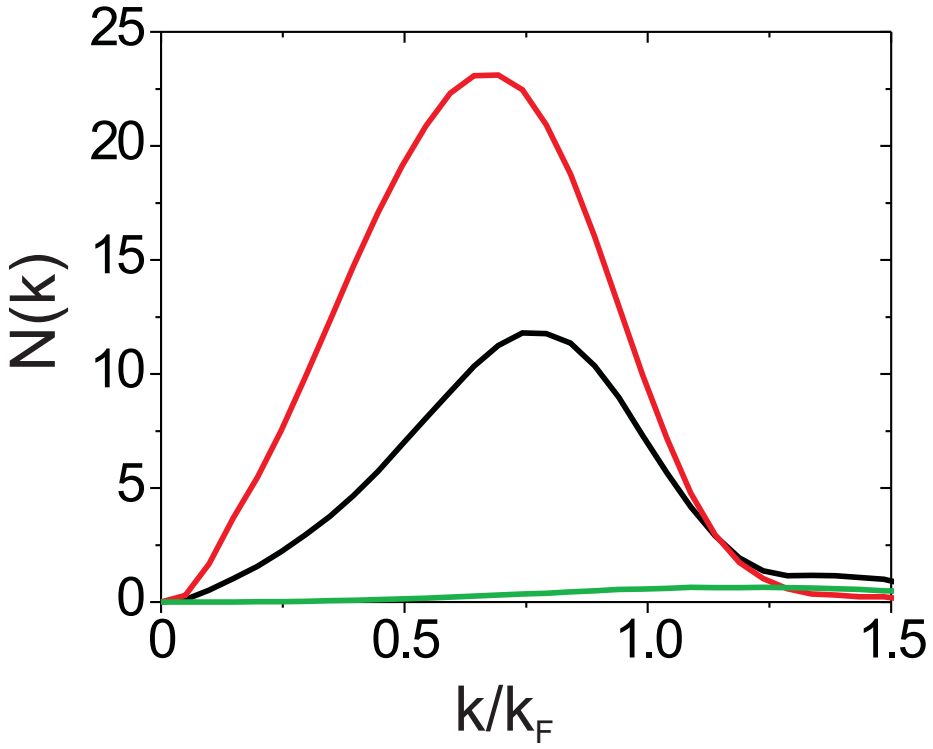

Figure 7.3: **Background signal** The measured number of atoms, as a function of k/k_F, where $N \propto n(k)k^2$, is shown with (black line) and without (red line) hollow light beams. The experimental data with the hollow light beams contain a contribution from the background signal (green line), which is calculated from a model. It is clear a background signal is present in the measured density distribution because the data with atoms removed by hollow light beams actually has higher signal for $k > 1.15k/k_F$ than the data where no optical pumping occurs. The data here have been smoothed to better show the difference between the curves at large k/k_F.

with nearly constant density, then we could actually observe a sharp Fermi surface. The hollow light beams allow us to accomplish exactly this. In this experiment, we cool an equal mixture of atoms in the $|9/2, -7/2\rangle$ and $|9/2, -9/2\rangle$ ground states to a temperature of $T/T_F = 0.10 \pm 0.02$ at a magnetic field of approximately 203.5 G. Then, we ramp the magnetic-field strength to a value in the range of $205 - 209$ G, corresponding to scattering lengths of -285 to -15 Bohr radii, where the Fermi gas can be considered to be weakly interacting. We then use an rf π-pulse to transfer all of the atoms in the $|9/2, -7/2\rangle$ state to the $|9/2, -5/2\rangle$ state where they will be resonant with the hollow light beams. After the rf pulse, the trapping potential is turned off and the hollow light beams are turned on for 40 μs (this is a short enough duration that the expansion and movement of the cloud due to gravity are negligible). The intensities of the hollow light beams are adjusted to control the total number of atoms optically pumped away. The momentum distributions for clouds where 0% and 60% of the atoms are removed is shown in Fig. 7.4. The momentum distributions for the cloud with 60% of the atoms removed clearly shows a sharp Fermi surface. To parameterize the sharpness of the Fermi surface we can fit the clouds to Fermi-Dirac distributions. In these fits, we let the temperature and value of k_F vary, as well as an overall scaling factor. For the cloud with 60% of the atoms removed, the fit gives $T/T_F = 0.19 \pm 0.04$, which is much lower than the trap averaged cloud, which fits to $T/T_F = 0.6 \pm 0.1$.

In Fig. 7.5, we show the value of T/T_F obtained from a fit to the momentum distribution versus the fraction of atoms remaining after optical pumping with the hollow light beams. The fraction is varied by varying the intensity of the beams. The line is an expected value obtained from a Monte Carlo simulation using the Fermi Dirac distribution and calculated atom removal probability (Fig. 7.2). In the limit of blasting away all of the atoms, we would expect $T/T_F = 0.1$, which corresponds to the degeneracy of atoms at the center of the trap.

The fact that the hollow light beams allow us to observe a Fermi surface confirms that the technique works as we expect and demonstrates the potential to uncover properties of a homogeneous Fermi gas from a trapped gas. The technique is ideally suited for observing a Fermi surface, in part because of the favorable dependence of k_F on the density ($k_F \propto n^{1/3}$). As an example,

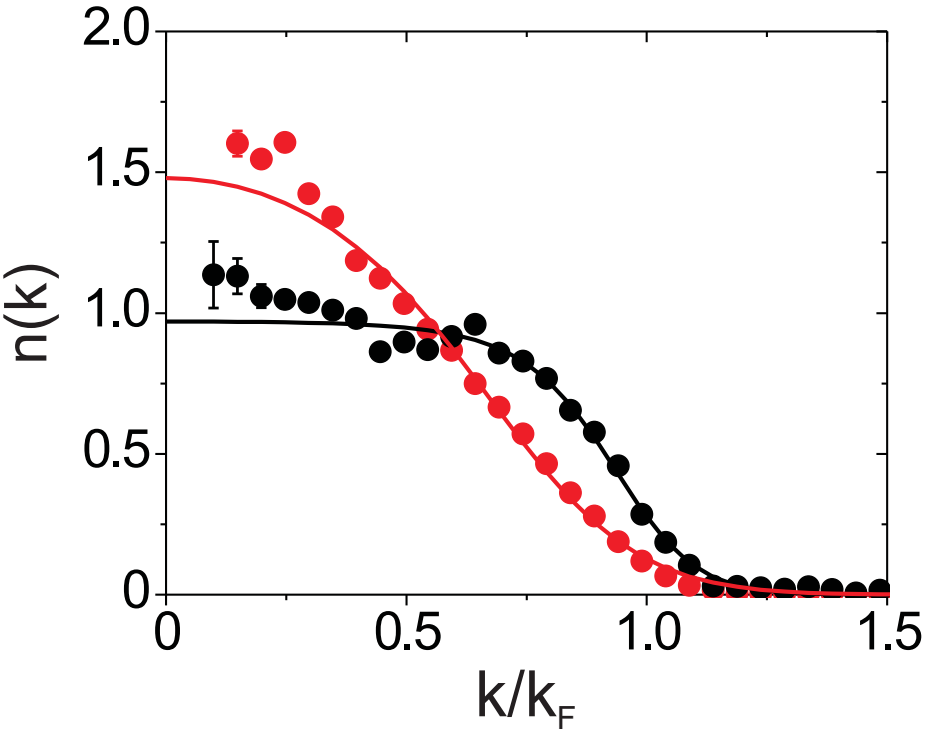

Figure 7.4: **Observing a Fermi surface** The fermion momentum distribution, $n(k)$ with (black circles) and without (red circles) optical pumping from the hollow light beams. The distributions are separately normalized to have an area of 1. Fits to the data with a Fermi-Dirac distribution for a homogeneous gas are shown (black and red lines). The fit to the data with optical pumping gives $T/T_F = 0.19 \pm 0.04$ and the fit to the data with no optical pumping gives $T/T_F = 0.58 \pm 0.14$. The optical pumping intensity was set to remove approximately 60% of the atoms. The error bars shown are statistical error; there may be residual systematic errors due to imperfections in the imaging system.

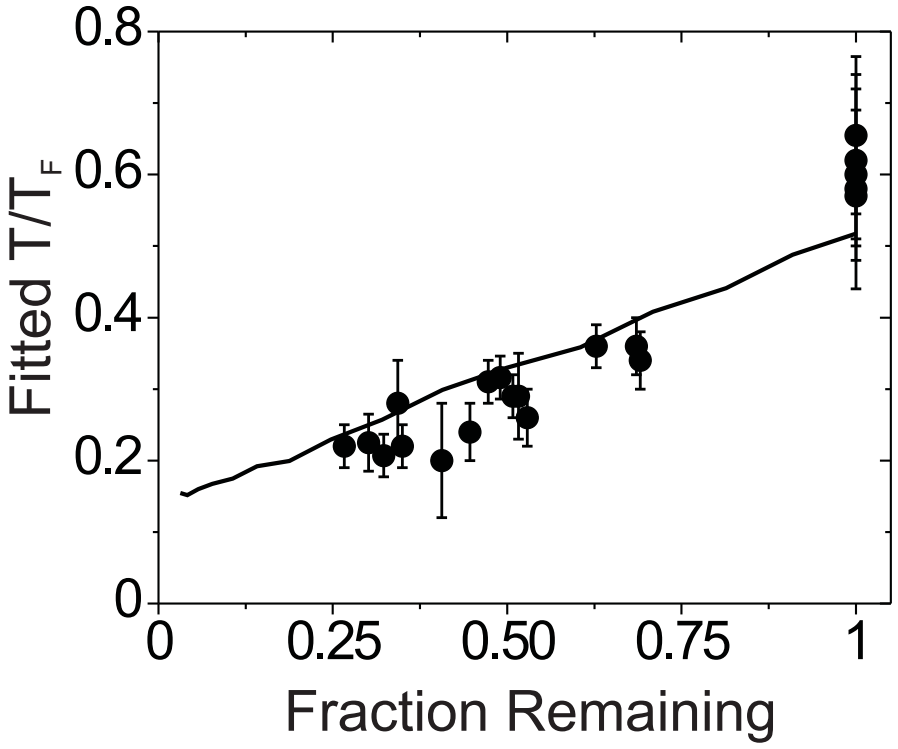

Figure 7.5: **Varying optical pumping intensity** The value of T/T_F obtained from fits to the momentum distribution of atoms after optical pumping with hollow light beams versus the fraction of atoms remaining after the optical pumping. The black line is a prediction from a model, which is described in the text. The temperature of the trapped gas before blasting is $0.11 \pm 0.02 T_F$. The power ratio of the two beams was set by measuring the number of atoms optically pumpbed by each beam on its own. The number of atoms optically pumped by the beam propagating along the axial direction was approximately twice the number of atoms optically pumped by the other beam.

this means that if we eliminate all the atoms from regions with a density less than half the peak density, the total variation in k_F would only be 20%.

7.3 Studying the effect of the trapping potential on atom-photoemission spectroscopy

We can now apply the hollow light beam technique to atom photoemission spectroscopy and begin to answer some questions regarding the effect of the trapping potential on the photoemission data. In particular, I will address the effect of the trapping potential on the shape of the single-particle dispersion and the energy widths of the quasi-particles. The first issue is important because BCS-like fits to the trap-averaged dispersions produce significantly larger values for the gap and chemical potential than what has been predicted by theory (see Fig. 6.18). While it is obvious that the trap confinement can affect the shape of the dispersion, and thus the values of fit parameters, we would like to investigate this effect experimentally and see if the data is consistent with theoretical predictions of the quasi-particle dispersion of a homogeneous gas.

The second issue is also very interesting. In the trap-averaged photoemission data, we measured energy widths near the Fermi surface that were a significant fraction of the Fermi energy (see Fig. 6.15). Answering the question of whether or not the widths are due to averaging over the density inhomogeneity, or are reflective of large intrinsic energy widths is a critical issue. The quasi-particle energy widths are an important component of understanding the nature of the strongly interacting gas in the pseudogap region and large widths would indicate a departure from typical Fermi-liquid behavior.

The comparisons to theoretical predictions presented in the previous chapter suggest answers to both of these questions. In the case of the shape of the dispersions, the theory, which predicts reasonable values for the gap and chemical potential of a homogeneous Fermi gas [99, 100], agrees with our trap averaged data after using a local density approximation. This suggests the trap averaged data are consistent with theoretically predicted dispersions for a homogenous gas. The theory also predicts that, while the energy widths of trap-averaged data are somewhat broadened

by the density inhomogeneity, they are also reflective of large intrinsic quasi-particle energy widths. It is the goal of this chapter to provide further experimental evidence for these claims by using the method of hollow light beams to obtain photoemission signal from the center of the Fermi gas.

In these experiments, the trap is parameterized by a radial trap frequency of $\omega_r = 2\pi \cdot 210$ Hz and an axial trap frequency of $\omega_z = 2\pi \cdot 16$ Hz. We obtain a 50/50 mixture of atoms in the the $|9/2, -9/2\rangle$ and $|9/2, -7/2\rangle$ spin states. Our final stage of evaporation occurs at a magnetic field of 203.5 G. At the end of the evaporation, we have 1.2×10^5 atoms per spin state at a normalized temperature $\frac{T}{T_F} = 0.13 \pm 0.02$.

After the evaporation, we increase the interaction strength adiabatically with a slow magnetic-field ramp to either 202.17G or 202.10G near the center of the Feshbach scattering resonance. Here, the interaction strengths can be characterized by the parameter $\frac{1}{k_F a} = 0.05 \pm 0.05$ and 0.20 ± 0.05 where k_F is the Fermi wavevector given by $\sqrt{2mE_F}/\hbar$. Using our previous measurements of the the size of an interacting Fermi gas [30], we estimate the peak and average density of the interacting cloud for the interaction strengths of $(0.05, 0.20)$ to be given by $(1.44, 1.51) \pm 0.1 n_0$ and $(0.70, 0.73) \pm 0.05 n_0$ where n_0 is the density of a homogenous gas with a Fermi energy of E_F and is given by Eq. 2.2.

For the photoemission experiments, the strongly interacting atomic gas is probed with an rf pulse to transfer a small fraction of the atoms in the $|9/2, -7/2\rangle$ state to the $|9/2, -5/2\rangle$ state. Immediately after the transfer, the trapping potential is switched off, so the atoms in the $|9/2, -5/2\rangle$ state can ballistically expand and be imaged to obtain their momentum distribution. To perform photoemission spectroscopy on the core of the gas, we use the technique of crossed hollow light beams to optically pump away $|9/2, -5/2\rangle$ atoms in the low density regions at the edges of the atom gas. The hollow light beams are pulsed on for 40 μs immediately after the trap is switched off (and thus, immediately after the rf pulse). The intensity of the beams is such that the integrated photoemission signal is reduced by approximately 60%. As in the case of a weakly interacting gas (Fig. 7.3), the optical pumping from the hollow light beams leaves a small number of atoms in the $|9/2, -5/2\rangle$ with increased momentum, creating a small high-momentum background in the

photoemission signal. We model this background and subtract it out as described in Fig. 7.3 and the Appendix B. The rf pulse amplitude envelope is gaussian, with a full width, $1/e^4$ amplitude duration ranging from 300 μs to 100 μs. A duration of 300 μs is used for rf frequencies near the free-particle dispersion, and shorter durations are used for larger detunings of the rf frequency, because the atoms outcoupled at those frequencies have large momenta and the hollow light beams must be pulsed on before the positions of the atoms can significantly change.

The results of photoemission experiments at two magnetic-field strengths with (b,d) and without (a,c) the hollow light beam are shown in Fig. 7.6. The white circles in Fig. 7.6 are the centers obtained from Gaussian fits to vertical cuts at constant k in the spectra and map out the dispersion for the occupied single-particle states. From Fig. 7.6, it is clear that removing atoms from the edge of the trap does not qualitatively change the spectra. For both $\frac{1}{k_F a} = 0.05$ and 0.20, we observe a BCS-like dispersion with back-bending near the Fermi wavevector k_F for the trap center data.

To quantitatively compare the spectra taken with and without the hollow light beam, we show in Fig. 7.7 the results of Gaussian fits to the EDCs for both the trap-averaged spectra (black circles), and the trap center spectra obtained with the hollow light beams (red squares). In the top panel, we plot the centers obtained from the fits. For $\frac{k}{k_F} < 0.75$ the trap center data is clearly shifted to lower energy compared to the trap averaged data. This is expected because atoms near the edge of the trap are at low density where the local $1/k_F a$ is large and the gas is weakly interacting. Therefore, these atoms contribute signal near the free particle line at low $\frac{k}{k_F}$. In fact, in comparing the two sets of spectra in Fig. 7.6, it is clear that the main effect of the hollow light beams is to decrease intensity near the free-particle line at $k < k_F$. This can also be seen in the momentum distributions, which are plotted in Fig. 7.8. Here, the trap center data has lower signal at low momenta.

To compare the trap center data obtained with the hollow light beams to theory for the limit of a homogeneous cloud, we show in Fig. 7.7 a dashed line corresponding to the expected dispersion for atoms at the center of the trap, Eq. 6.1. We use theoretical values for a homogeneous $T = 0$

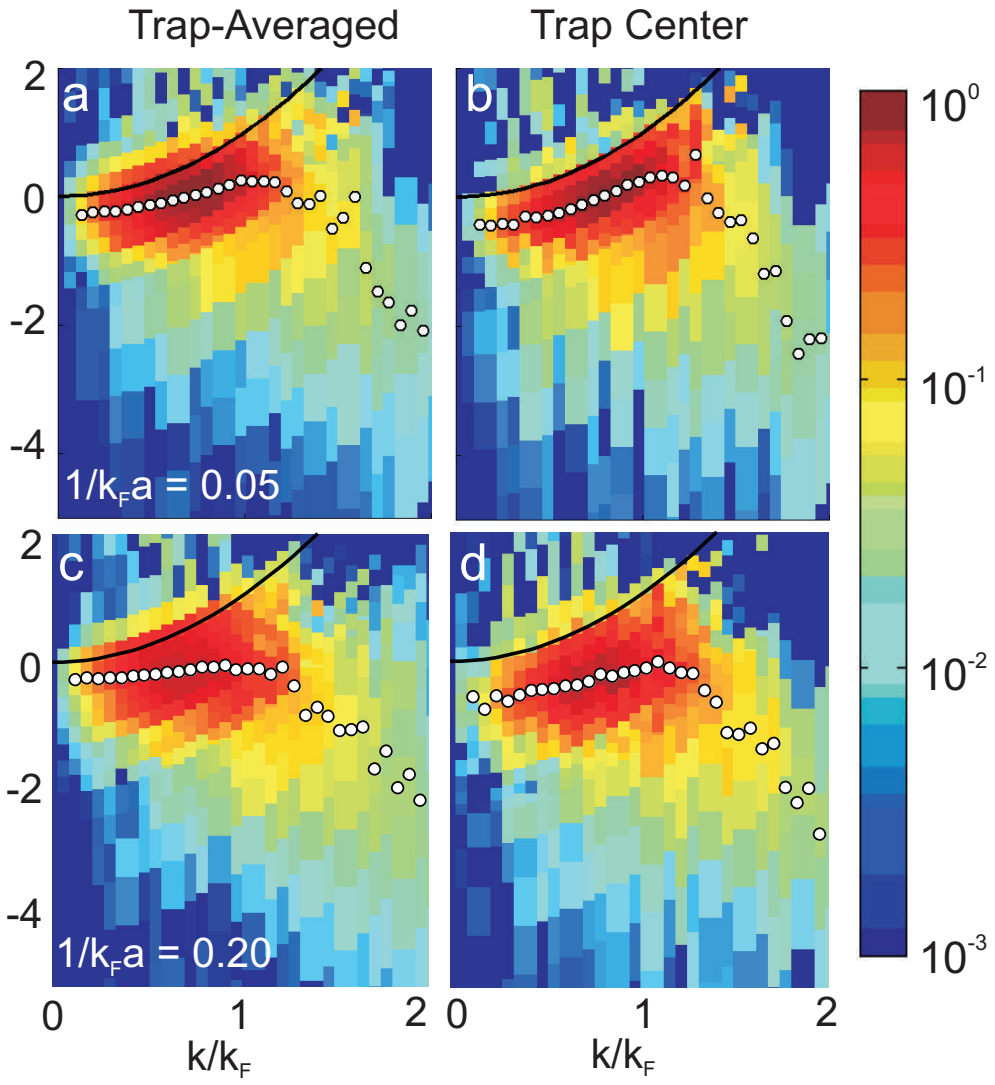

Figure 7.6: **Photoemission data with and without hollow light beams** (a) Trap averaged photoemission data for a gas at $\frac{1}{k_F a} = 0.05$ at $\frac{T}{T_F} = 0.13$. (b) Trap center photoemission data for the same gas obtained by removing 60% of the atoms using the intersecting hollow light beams. c) Trap-averaged data at $\frac{1}{k_F a} = 0.20$. d) Trap center data at $\frac{1}{k_F a} = 0.20$. White dots show the centers of gaussian fits to the EDCs of each data set. While the spectra are qualitatively similar, and both show BCS-like backbending of the dispersion, the intensity at low momenta near the free-particle dispersion (black line) is decreased in both of the trap center data sets. This shifts the centers of the EDCs to lower energy.

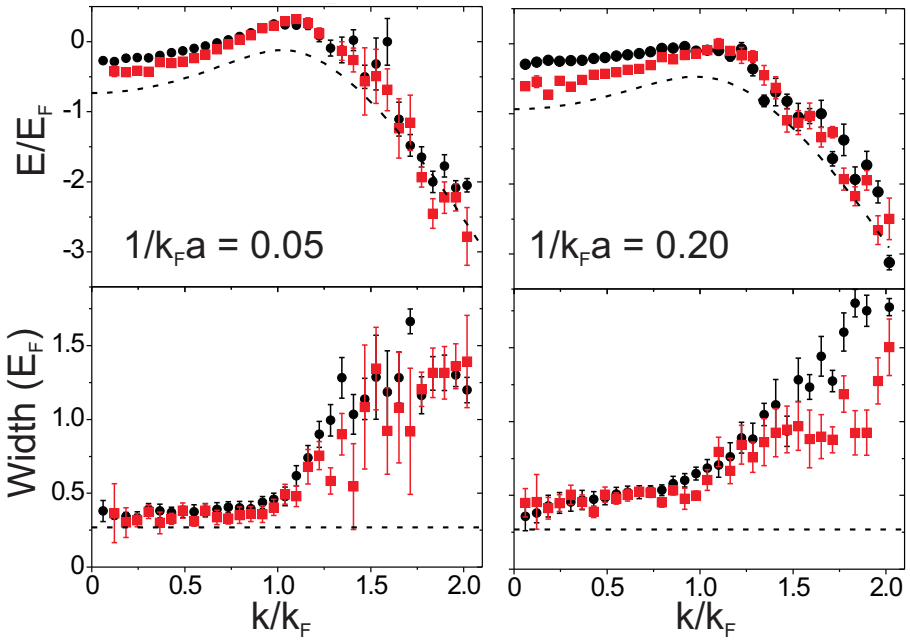

Figure 7.7: **EDC fit results** We show the centers (top) and rms widths (bottom) from gaussian fits to the EDCs of the spectra shown in Fig. 7.6. The left side is data for a gas at $\frac{1}{k_F a} = 0.05$ and the right side is for a gas at $\frac{1}{k_F a} = 0.20$. Trap averaged data is shown as black circles and trap center data is shown as red squares. The dashed lines in the top panels are the expected $T = 0$ dispersion for atoms at the center of the cloud obtained using our estimate of the peak density and the values reported in Refs. [19, 20]. In the lower panels, the horizontal dashed lines are placed at the experimental energy resolution due to the finite duration of the rf pulse. The resolution is approximately $0.25 E_F$.

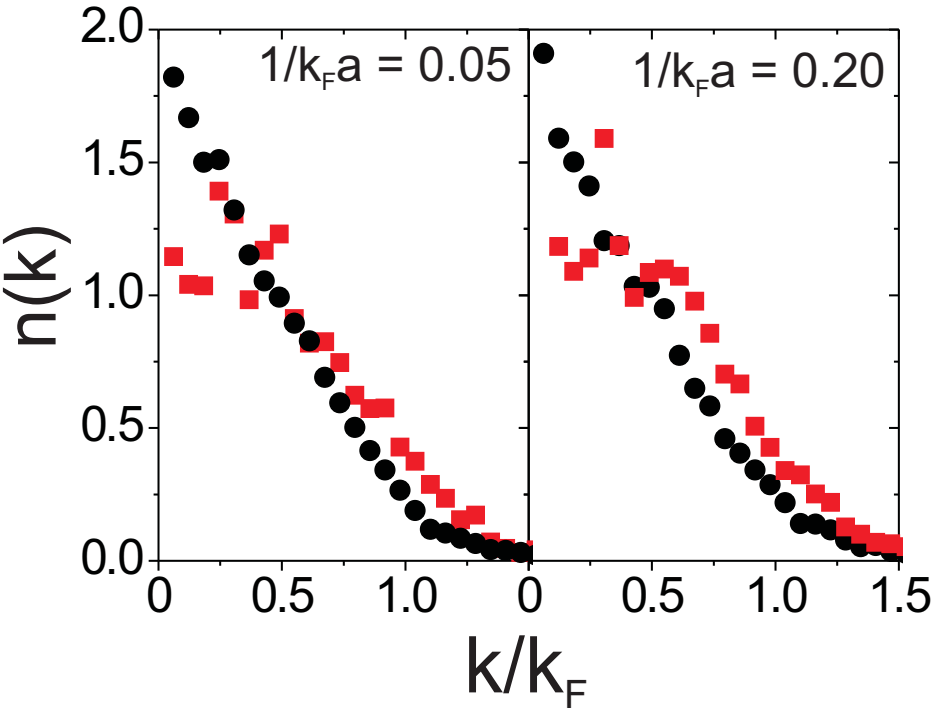

Figure 7.8: **Momentum distributions** Single-particle momentum distributions with (red squares) and without (black circles) hollow light beams for the data at $\frac{1}{k_F a} = 0.05$ (left) and the data at $\frac{1}{k_F a} = 0.20$ (right) at $T/T_F = 0.13 \pm 0.02$. The effect of the hollow light beams is to remove fermions with low momenta. The distributions are normalized to have an area of 1. The distributions are obtained by integrating over the energy axis of the photoemission data of Fig. 7.6.

gas for μ of $0.38E_F$ and $0.22E_F$ for $1/k_Fa = 0.05$ and 0.20 respectively, from Ref. [20]. For the values of Δ, we use $0.47E_F$ and $0.58E_F$ and for k_L we use 0.91 and 0.85 for $1/k_Fa = 0.05$ and 0.20 respectively, measured for a low temperature gas in Ref. [19]. When values for the exact coupling strength were not available, we used a linear extrapolation between the closest points. These values where then scaled using our estimate for the peak density in the trapped gas given above. For low momenta ($k < 0.75k_F$), the dispersions obtained from the data with the hollow light beams can be seen to be approaching this limit. For larger momenta ($k > 0.75k_F$), the data with and without hollow light beams appear to be similar. This indicates that atoms near the edge of the cloud may not contribute much signal at large momenta. In order to see the data approach the expected dispersion for the trap center at momenta near $k/k_F = 1$, it is likely that a more homogenous sample is necessary. It should be noted that, because the data is at finite temperature, even if we could only measure atoms at the exact trap center, the dispersion would not fully approach the theoretical dispersion, which is obtained in the zero temperature limit. Rather, we expect the maximum energy of the dispersion curve to move to higher energies at finite temperature, due to the closing of the gap and presence of signal from excitations.

Fitting the modified BCS dispersion to the trap averaged and trap center data we obtain values of (μ,Δ,k_L) in terms of E_F and k_F shown in table 7.1.

Table 7.1: BCS Fit Results

Parameter	$\frac{1}{k_Fa} = 0.05$		$\frac{1}{k_Fa} = 0.20$	
	Trap average	Trap center	Trap average	Trap center
μ	0.85 ± 0.14	0.54 ± 0.12	0.93 ± 0.18	0.47 ± 0.12
Δ	0.59 ± 0.15	0.16 ± 0.16	0.98 ± 0.19	0.54 ± 0.11
k_L	1.01 ± 0.03	1.03 ± 0.03	0.87 ± 0.04	1.00 ± 0.04

The trap averaged values are on the left and the trap center values are on the right. From this data, we can conclude that when fitting the dispersion obtained from trap-averaged data one obtains larger values of μ and Δ than for trap center data. This is because signal from atoms at low density near the trap edge shift the centers of the EDCs at low momenta to higher energy.

As expected, the size of the gap is larger for the data at $1/k_F a = 0.20$ compared to the data at $1/k_F a = 0.05$ and the value of k_L is smaller (the expected trends are shown in Fig. 6.18). One would also expect the chemical potential to be slightly smaller at $1/k_F a = 0.20$, however, the error in μ is too large to determine the trend. Interestingly, the value of the maximum energy of the dispersion appears robust against removing atoms from the edge of the cloud. This may explain why our estimates of the gap and chemical potential based on this value for the trap-averaged data in Chapter 6 appear more reasonable than the values obtained directly from the BCS fit (Fig. 6.18). However, it is not clear if this value would change if the gas were made more homogeneous. Furthermore, it should be mentioned that the EDC centers in the region $k_F < k < 1.4k_F$ for the trap-center data can be affected by the background subtraction (discussed in Fig. 7.3 and Appendix B).

The lower panels in Fig. 7.7 shows the widths of the gaussian fits to the EDCs of the trap-averaged and trap-center data. Surprisingly, there is little change in the EDC widths, indicating that the widths may come from large intrinsic energy widths. This is particularly clear in the data taken at $\frac{1}{k_F a} = 0.20$. This suggests that the gas is far from the limit of a Fermi-liquid where the EDC energy widths should become small near the Fermi surface. In fact, it is not surprising that sharp quasi-particles are absent if one looks at the momentum distribution Fig. 7.8. Here $n(k)$ is obtained by summing over the energy axis in the data of Fig. 7.6 and dividing out the $(\frac{k}{k_F})^2$ phase-space factor. Unlike the data for a weakly interacting gas shown in Fig. 7.4, the trap center momentum distribution for the strongly interacting gas does not show a sharp Fermi surface. However, a sharp Fermi surface is required for application of Fermi liquid theory [68].

In summary, using two intersecting hollow light beams, we can measure the momentum distribution of atoms at the center of a trapped Fermi gas by optically pumping atoms at large radius to another spin state. Using the hollow light beams, we can observe a sharp Fermi surface in a weakly interacting Fermi gas. We can also use the hollow light beams to obtain atom-photoemission spectra for strongly interacting atoms at the center of the gas. These spectra allow us to study the effect of the trapping potential on atom-photoemission spectroscopy. We find that the trap center

data is qualitatively similar to the trap-averaged data, but with less signal at low k/k_F near the free-particle dispersion. The widths of the EDCs near the Fermi surface remain large, and no sharp Fermi surface is observed. These observations indicate the gas is far from the regime of a normal Fermi liquid. One consequence of the large energy widths is that it may be difficult to understand transport phenomena in terms of standard Fermi-liquid theory, which assumes quasi-particles, and strongly interacting Fermi gases are a novel system for research of dynamics in strongly interacting systems [101].

Chapter 8

Universal relations and the contact

8.1 The contact

A typical treatment of a weakly interacting Fermi gas with short-range interactions involves perturbation theory in the small parameter $1/k_F a$. However, it is obvious that the short-range potential will have certain non-perturbative effects on the wave-functions of particles at short distances. For example, a strongly repulsive short-range potential of range r_0 will preclude the wave-functions of any two particles from overlapping at distances smaller than r_0. This implies a strong correlation between the particles that is clearly not captured at a mean-field level approximation, which nevertheless generally predicts the correct behavior of the system in other respects. For example, in the Hartree-Fock approximation for a homogeneous Fermi gas, one takes the many-body wave-function to be a Slater determinant of plane-wave states [56], yet the approximation scheme is accurate for calculating the total energy of the system in the limit of small $1/k_F a$. It is clear that this short-range behavior is not important for most properties of the system (except in that it controls the value of the scattering length) as long as the physical interaction occurs at length scales much smaller than other length scales in the problem.

However, a new set of relations, referred to as the Tan relations, demonstrate that the short-range behavior of the wave-functions can actually be linked to several macroscopic properties of the gas, such as the total energy, in a **universal way, valid for all scattering lengths and phases of the gas** [102, 103, 104]. This amazing revelation is at first quite difficult to believe.

For particles interacting via a contact interaction, the wave-function describing two particles

at small inter-particle separation, r, must behave as

$$\lim_{r\to 0} \Phi(r) = (1/r - 1/a)A \tag{8.1}$$

where r is the internuclear distance, a is the scattering length [104, 36], and A is a constant that depends on the problem. A quantity called the contact C, can be defined by

$$\mathcal{C}(\vec{R}) = \lim_{s\to 0}(4/s^4)N_{pair}(\vec{R}, s) \tag{8.2}$$

where $\mathcal{C}(\vec{R})$ is the contact density at position $\vec{R}$ and $N_{pair}(\vec{R}, s)$ is the probability of finding two particles of opposite spin inside a sphere of radius s centered at position $\vec{R}$. The contact, C is obtained from the contact density by $C = \int d^3R\mathcal{C}(\vec{R})$. The s^4 behavior of $N_{pair}(\vec{R}, s)$ can be obtained from Eq. 8.1 by noting that the probability to find the first atom simply scales as the volume, $\frac{4}{3}\pi s^3$, and the probability of finding the second atom can be obtained from $4\pi \int_0^s \Phi(r)^2 r^2 dr$, which is proportional to s in the limit $s \ll a$. Thus, $N_{pair}(R, s) \propto s^4$. If the positions of the particles were not correlated, $N_{pair}(\vec{R}, s)$ would go as s^6, and then we would find $\mathcal{C}(\vec{R}) = 0$. If the short-range potential has an effective range r_0, the relation holds for s smaller than other length scales in the system but larger than r_0.

In a gas with only short-range interactions, the interaction energy is determined by the probability for particles to be close to each other and this is parameterized by C. If one tunes the scattering length, the change in the energy of the system that this produces should be proportional to the number of fermions that are close enough together to be interacting. A formal proof, first given by Shina Tan, showed that this relation, called the adiabatic sweep theorem can be written

$$2\pi \frac{dE}{d(-1/(k_F a))} = C \tag{8.3}$$

where E is the total energy in units of the E_F and C is the contact in units of k_F [102].

This amazing relation links the short distance properties of the particle wave-functions to the total energy of the system. Tan's derivation does not make any assumptions about the phase of the gas (superfluid, normal, ect.), temperature, size, interaction strength, or even quantum statistics of the particles and so is universally valid for all Fermi and Bose gases that can be characterized

by short-range 2-body interactions [102, 103, 104, 105]. Although the contact may seem like a quantity purely governed by two-body physics, it is linked to the many-body properties of the system through the overall normalization of the wave-function that determines the constant A in Eq. 8.1, and actually encapsulates all of the many-body physics of the system, see for example Ref. [106].

While we do not have a good experimental method for measuring C based on Eq. 8.2, an alternative definition involving the momentum distribution is easily derived. The momentum distribution $n(k)$ can be obtained by squaring the Fourier transform of Eq. 8.1, and the $1/r$ term leads to a $1/k^4$ tail for large momenta. The amplitude of this $1/k^4$ is equal to C, with

$$C = \lim_{k\to\infty} k^4 n(k) \tag{8.4}$$

where the limit is understood to mean in the limit where k is larger than other momenta in the system, but less than $1/r_0$.

The momentum distribution is a natural quantity to experimentally measure in atomic gases with time- of-flight expansion. It can also be directly obtained from the occupied spectral function measured by photoemission experiments. Indeed, a high momentum feature in the spectral function is predicted to be a universal feature in the spectral function of Fermi gases (see Ref. [17] and Fig. 6.9).

Besides Eq. 8.3, a number of other relations (the set of relations involving the contact are termed the Tan relations) have been derived by Tan and others [103, 105, 22, 107, 101]. These relations link the contact to a large number of experimentally measurable quantities that are listed in the recent review of the subject in Ref. [108] and include: the pressure, rf spectra, photoassociation rates, closed channel molecule fraction, static structure factor, and viscosity. In particular, a generalized viral theorem for a harmonically trapped gas has also been derived [103], and I will present an experimental verification of the relation in the next section. The generalized virial theorem is given by

$$E - 2V = T + I - V = -\frac{C}{4\pi k_F a} \tag{8.5}$$

where E is the total energy and can be broken up into three terms T, I, and V, [103] where T is the kinetic energy, I is the interaction energy, and V is the potential energy due to a harmonic trapping potential.

Before moving on to the experimental measurement of the contact and verification of the Tan relations, I would like to discus one more important point. The reader may have noted that a momentum distribution that falls off as $1/k^4$ produces a divergent kinetic energy. While, the issue of an obviously unphysical infinite energy is resolved by the finite range cutoff, this still leaves the question of what happens to the extremely large but finite kinetic energy of the gas (large compared to say the Fermi energy). The answer to this question, resolved by Tan, is that there is an equally large (or divergent, in the case of $r_0 = 0$) but negative interaction energy that comes from the $1/r$ behavior of the wave-function at short distance [104]. Thus, while the individual terms in the energy, T and I, diverge for a zero-range potential, the sum $T + I$ is finite. This again demonstrates how a basic perturbation theory can miss the short-range and large-momentum physics of the contact interaction but nevertheless get the total energy correct.

8.2 Measuring the contact

A couple of recent works have measured the contact for a Fermi gas and compared results to theoretical predictions, which are obtained by inserting calculations of the energy from Monte Carlo simulations into Eq. 8.3. Specifically, photoassociation measurements to determine the closed-channel fraction [109, 22], and inelastic Bragg scattering [107] were used to extract the contact and compare to theory. The recent measurements of the pressure and energy of a Fermi gas in the BCS-BEC crossover can also be used to extract the contact [13, 110, 89]. The work I present in this chapter was published in Ref. [10] and was undertaken after the photoassociation experiments, and concurrently with the Bragg and equation-of-state measurements. Our work is unique in that we measured the contact using several techniques, including rf spectroscopy, the momentum distribution, the release energy, and the potential energy and applied these measurements to directly verify the adiabatic theorem and the generalized virial theorem in a model-independent way. In

particular, to my knowledge, no other work has extracted the contact from rf spectroscopy or measurements of the momentum distribution and no other work has directly tested the generalized virial theorem.

Our measurements are done in an ultra cold gas of fermionic ^{40}K atoms confined in a harmonic trapping potential with a 50/50 mixture of atoms in two spin states the $|9/2, -9/2\rangle$ and $|9/2, -7/2\rangle$ spin states. The trap is parameterized by a radial trap frequency, which varies for these data from $\omega_r = 2\pi \cdot 230$ to $2\pi \cdot 260$ Hz and an axial trap frequency, which varies from $\omega_z = 2\pi \cdot 17$ to $2\pi \cdot 21$ Hz. Our final stage of evaporation occurs at a magnetic field of 203.5 G, where the s-wave scattering length, a, that characterizes the interactions between atoms in the $|9/2, -9/2\rangle$ and $|9/2, -7/2\rangle$ states is approximately 800 a_0, where a_0 is the Bohr radius. At the end of the evaporation, we have 10^5 atoms per spin state at a normalized temperature $\frac{T}{T_F} = 0.11 \pm 0.02$, where the Fermi temperature T_F corresponds to the Fermi energy, $E_F = k_b T_F = \hbar\omega(6N)^{1/3}$. Here, N is the atom number in one spin state, ω is the geometric mean trap frequency given by $\omega = (\omega_r^2 \omega_z)^{1/3}$, and k_b is the Boltzmann constant. After the evaporation, we increase the interaction strength adiabatically with a slow magnetic-field sweep to a Feshbach scattering resonance.

To measure the contact, we obtain $n(k)$ using ballistic expansion of the trapped gas, where we turn off the interactions for the expansion. We accomplish this by rapidly sweeping the magnetic field to 209.2 G where a vanishes, and then immediately turning off the external trapping potential [67] and taking an absorption image of the cloud after 6 ms of expansion. The probe light for the imaging propagates along the axial direction of the trap and thus we measure the radial momentum distribution. Assuming the momentum distribution is spherically symmetric, we obtain $n(k)$ with an inverse Abel transform. We normalize $n(k)$ for a 50/50 spin mixture such that

$$\int \frac{n(k)}{(2\pi)^3} d^3k = 0.5. \tag{8.6}$$

Fig. 8.1a shows an example $n(k)$ measured for a strongly interacting gas with a dimensionless interaction strength $(k_F a)^{-1}$ of -0.08 ± 0.04. The measured $n(k)$ exhibits a $1/k^4$ tail at large k and we extract the contact C from the average value of $k^4 n(k)$ for $k > k_C$, where we use $k_C = 1.85$ for

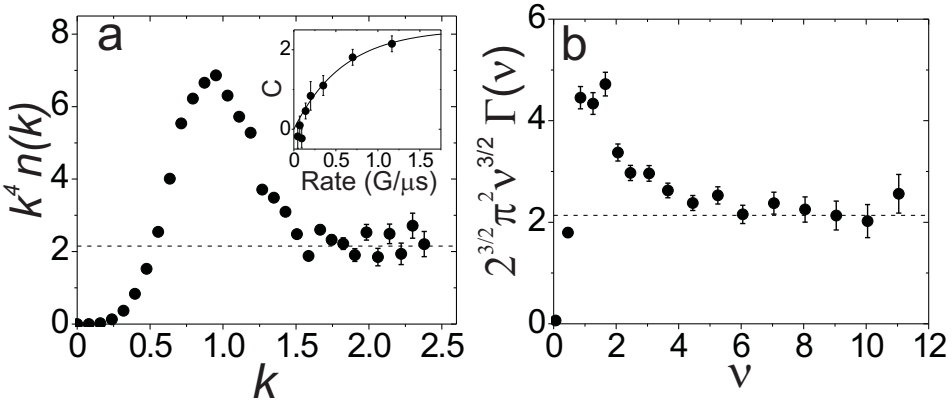

Figure 8.1: **Extracting the contact from the momentum distribution and rf lineshape** (a) Measured momentum distribution for a Fermi gas at $\frac{1}{k_F a} = -0.08 \pm 0.04$. Here, the wave number k is given in units of k_F, and we plot the normalized $n(k)$ multiplied by k^4. The dashed line corresponds to 2.2, which is obtained by averaging $k^4 n(k)$ for $k > 1.85$. (Inset) The measured value for C depends on the rate of the magnetic-field sweep that turns off the interactions before time-of-flight expansion. (b) RF lineshape measured for a Fermi gas at $\frac{1}{k_F a} = -0.03 \pm 0.04$. Here, ν is the rf detuning from the single-particle Zeeman resonance, given in units of E_F/h. We plot the normalized rf lineshape multiplied by $2^{3/2}\pi^2\nu^{3/2}$, which is predicted to asymptote to C for large ν. Here, the dashed line corresponds to 2.1, from an average of the data for $\nu > 5$.

$(k_F a)^{-1} > -0.5$ and $k_C = 1.55$ for $(k_F a)^{-1} < -0.5$. These values for k_C are chosen empirically such that for $k \geq k_C$ the momentum distributions are in the asymptotic limit to within our statistical measurement uncertainties. One issue for this measurement is whether or not the interactions are switched off sufficiently quickly to accurately measure the high-k part of $n(k)$. The data in Fig. 8.1a were taken using a magnetic-field sweep rate of $1.2\frac{G}{\mu s}$ to turn off the interactions for the expansion. In the inset to Fig. 8.1a, we show the dependence of the measured C on the magnetic-field sweep rate. Using an empirical exponential fit (line in Fig. 8.1a inset), we estimate that for our typical sweep rates of 1.2 to $1.4\frac{G}{\mu s}$, C is systematically low by about 10%. We have therefore scaled C measured with this method by 1.1.

The contact is also manifest in rf spectroscopy, where one applies a pulsed rf field and counts the number of atoms that are transferred from one of the two original spin states into a third, previously unoccupied, spin state [39]. We transfer atoms from the $|9/2, -7/2\rangle$ state to the $|9/2, -5/2\rangle$ state. It is predicted that the number of atoms transferred as a function of the rf frequency, ν, scales as $\nu^{-3/2}$ for large ν, and that the amplitude of this high frequency tail is given by [111, 112, 113]

$$\lim_{\nu \to \infty} \Gamma(\nu) = \frac{C}{2^{3/2}\pi^2} \nu^{-3/2}. \tag{8.7}$$

Here, $\nu = 0$ is the single-particle spin-flip resonance, and ν is given in units of E_F/h. This prediction requires that atoms transferred to the third spin-state have only weak interactions with the other atoms, so that "final-state effects" are small [113, 74, 114, 115, 116, 117, 118, 119], as is the case for ^{40}K atoms. In Fig. 8.1b, we plot a measured rf spectrum multiplied by $2^{3/2}\pi^2\nu^{3/2}$. The rf spectrum, $\Gamma(\nu)$, is normalized so that the integral over the rf lineshape equals 0.5. We observe the predicted $1/\nu^{3/2}$ behavior for large ν, and obtain the contact by averaging $2^{3/2}\pi^2\nu^{3/2}\Gamma(\nu)$ for $\nu > \nu_C$, where we use $\nu_C = 5$ for $(k_F a)^{-1} > -0.5$ and $\nu_C = 3$ for $(k_F a)^{-1} < -0.5$. These values for ν_C are chosen empirically such that for $\nu \geq \nu_C$ the rf spectrum is in its asymptotic limit.

The connection between the rf spectrum and the high-k tail of the momentum distribution can be seen in the Fermi spectral function, which can be probed using photoemission spectroscopy

for ultra cold atoms [9]. Recent photoemission spectroscopy results on a strongly interacting Fermi gas [18] revealed a weak, negatively dispersing feature at high k that persists to temperatures well above T_F. This feature was attributed to the effect of interactions, or the contact, consistent with a recent prediction [17]. Atom photoemission spectroscopy, which is based upon momentum-resolved rf spectroscopy, also provides a method for measuring $n(k)$. By integrating over the energy axis, or equivalently, summing data taken for different rf frequencies, we obtain $n(k)$. This alternative method for measuring $n(k)$ yields results similar to the ballistic expansion technique, but avoids the issue of magnetic-field sweep rates.

In Fig. 8.2 we show the measured contact for different values of $1/k_F a$. The contact is shown in units of the Fermi momentum k_F. Our data do not extend to larger values of $1/k_F a$ where we find that our magnetic-field sweeps are no longer fully adiabatic [44]. Fig. 8.2 shows the contact extracted using the three different techniques described above to probe two distinct microscopic quantities, namely $n(k)$ and $\Gamma(\nu)$. We find that the amplitude of the $1/k^4$ tail of $n(k)$ and the coefficient of the $1/\nu^{3/2}$ tail of $\Gamma(\nu)$ yield consistent values for C. The error bars shown in Fig. 8.2 include both statistical and estimated systematic uncertainties, which are roughly equal in magnitude. In extracting the contact from the rf measurements, the largest source of systematic error comes from residual interactions with atoms in third spin state [113]. For the ballistic expansion measurements, the systematic uncertainty is dominated by the effect of the finite magnetic-field sweep rate. For comparison with the data, the solid line in Fig. 8.2 shows a prediction for the contact that was reported in Fig. 1 of Ref. [22]. This zero temperature prediction consists of the BCS limit, interpolation of Monte Carlo data near unitarity, and the BEC limit for a trapped gas and uses a local density approximation.

8.3 Testing the Tan relations

In the preceding section, I presented three techniques for measuring the contact that probe the small-length scale physics of the gas through measurements of the momentum distribution and rf lineshape. Now, we would like to test whether those measurements can indeed be used to make

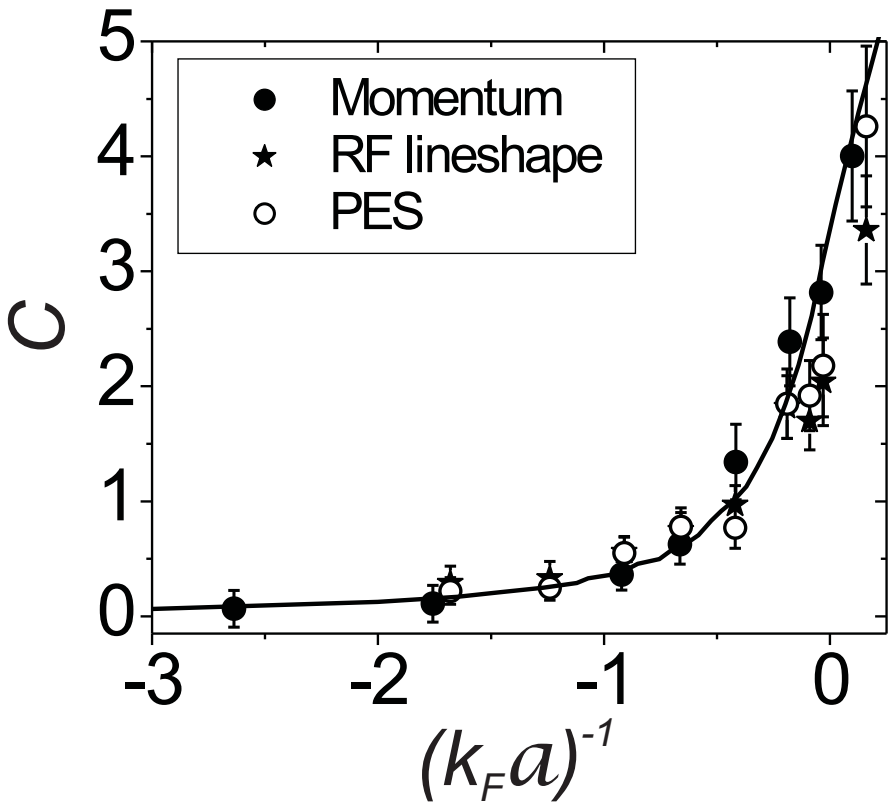

Figure 8.2: **The contact** We measure the contact, C, as a function of $(k_F a)^{-1}$ using three different methods. Filled circles correspond to direct measurements of the fermion momentum distribution $n(k)$ using a ballistic expansion, in which a fast magnetic-field sweep projects the many-body state onto a non-interacting state. Open circles correspond to $n(k)$ obtained using atom photoemission spectroscopy measurements. Stars correspond to the contact obtained from rf spectroscopy. The values obtained with these different methods show good agreement. The contact is nearly zero for a weakly interacting Fermi gas with attractive interactions (left hand side of plot) and then increases as the interaction strength increases to the unitarity regime where $(k_F a)^{-1} = 0$. The line is a theory curve obtained from Ref. [22].

predictions about macroscopic properties of the gas, such as the total energy. As mentioned above, the total energy can be split into two well-behaved parts, the potential energy to the harmonic trap, V, and the release energy $T + I$, which is the sum of the kinetic and interaction energy. We use measurements of both of these quantities to test the adiabatic sweep theorem, Eq. 8.3, and the generalized virial theorem, Eq. 8.5.

We measure V by imaging the spatial distribution of the atom cloud [30]. We allow the cloud to expand for 1.6 ms to lower the optical density and then image along one of the radial directions in order to see the density distribution in the axial direction. Because the expansion time is 40 times shorter than the axial trap period, the density distribution in the axial direction reflects the in-trap density distribution. The potential energy per particle, in units of E_F, is then $V = \frac{3}{E_F}\frac{1}{2}m\omega_z^2\langle z^2\rangle$, where $\langle z^2\rangle$ is the mean squared width of the cloud in the axial direction and we have assumed that the potential energy is distributed equally in x, y, and z.

To measure $T + I$ we turn off the trap suddenly and let the cloud expand for $t = 16$ ms (with interactions) before imaging along one of the radial directions; this is similar to measurements reported in Ref. [120]. The total release energy is the sum of the release energy in the two radial directions and the release energy in the axial direction. For the radial direction, the release energy per particle, in units of E_F, is simply $T_r + I_r = \frac{2}{E_F}\frac{1}{2}m\frac{\langle y^2\rangle}{t^2}$ where t is the expansion time and $\langle y^2\rangle$ is the mean squared width of the expanded cloud in the radial direction. For the axial direction, the expansion is slower and the expanded cloud may not be much larger than the in-trap density distribution. This is especially true near the Feshbach resonance where the cloud expands hydrodynamically [121]. Accounting for this, the axial release energy is $T_z + I_z = \frac{1}{E_F}\frac{1}{2}m\frac{\langle z^2\rangle - z_0^2}{t^2}$, where z_0^2 is mean squared axial width of the in-trap density distribution.

We extract the mean squared cloud widths from surface fits to the images, where we fit to a finite temperature Fermi-Dirac distribution. Rather than being theoretically motivated, we simply find empirically that this functional form fits well to our images. In order to get the best estimate of the energy in the clouds, we perform a weighted fit where each point in the image is weighted by the square of the distance from the center of the cloud. To eliminate systematic

error due to uncertainty in the trap frequencies and imaging magnification, we measure the release energy and potential energy of a very weakly interacting Fermi gas at $\frac{T}{T_F} = 0.11$, where we expect $T + I = V = 0.40E_F$. We then use the ratio of $0.40E_F$ to our measured values as a multiplicative correction factor that we apply to the data. This correction is within 5% of unity. For the point with $\frac{1}{k_F a} > 0$ we add the binding energy of the molecules, $-1/(k_F a)^2$, to the release energy $T + I$. We show our data for the V and $T + I$ versus $(k_F a)^{-1}$ in the inset of Fig. 8.3. The error bars shown in Fig. 8.3 include both statistical and systematic sources of uncertainty, which are roughly equal in magnitude.

We can now test the predicted universal relations connecting the $1/k^4$ tail of the momentum distribution with the thermodynamics of the trapped Fermi gas. We first consider the adiabatic sweep theorem. The inset to Fig. 8.3 shows E obtained by summing the measured values for $T + I$ and V. To test the adiabatic sweep theorem, we find the derivative, $\frac{dE}{d(-1/(k_F a))}$, simply by calculating the slope for pairs of neighboring points in the inset of Fig. 8.3. In the main part of Fig. 8.4, we compare this point-by-point derivative, multiplied by 2π, to C obtained from the weighted averages of the the data shown in Fig. 8.2($\circ$). Comparing these measurements of the left and right sides of Eqn. 8.3, we find good agreement and thus verify the adiabatic sweep theorem for our strongly interacting Fermi gas.

To test Eq. 8.5, in Fig. 8.4 we plot the measured difference $T + I - V$ versus $(k_F a)^{-1}$ along with $\frac{C}{4\pi k_F a}$, where we use our direct measurements of C. We find that these independent measurements of the left and the right sides of Eqn. 8.5 agree to within the error bars, which include both statistical and systematic sources of uncertainty. It is interesting to note that the measured energy difference $T + I - V$ is small (in units of E_F), so that even a Fermi gas with a strongly attractive contact interaction nearly obeys the non-interacting virial equation.

In conclusion, we have measured the integrated contact for a strongly interacting Fermi gas and demonstrated the connection between the $1/k^4$ tail of the momentum distribution and the high frequency tail of rf spectra. Combining a measurement of C vs $(k_F a)^{-1}$ with measurements of the potential energy and the release energy of the trapped gas, we verify two universal relationships

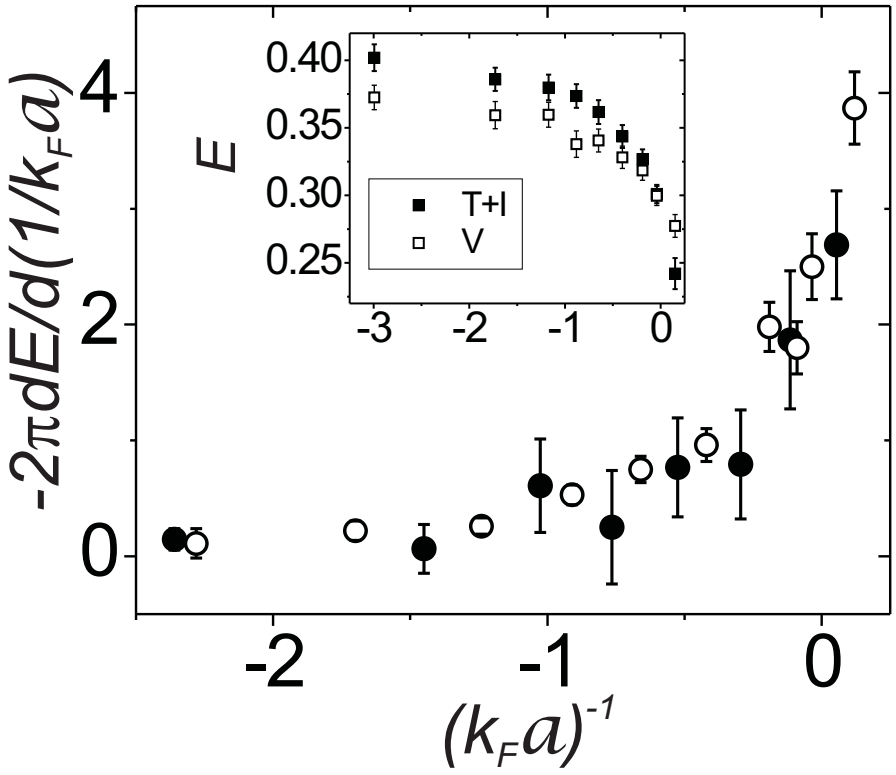

Figure 8.3: **Testing the adiabatic sweep theorem** (Inset) The measured potential energy, V, and release energy, $T + I$, per particle in units of E_F are shown as a function of $1/k_F a$. (Main) Taking a discrete derivative of the data shown in the inset, we find that $2\pi \frac{dE}{d(-1/(k_F a))}$ (•) agrees well with the average value of the contact C obtained from the measurements shown in Fig. 8.2 (◦).

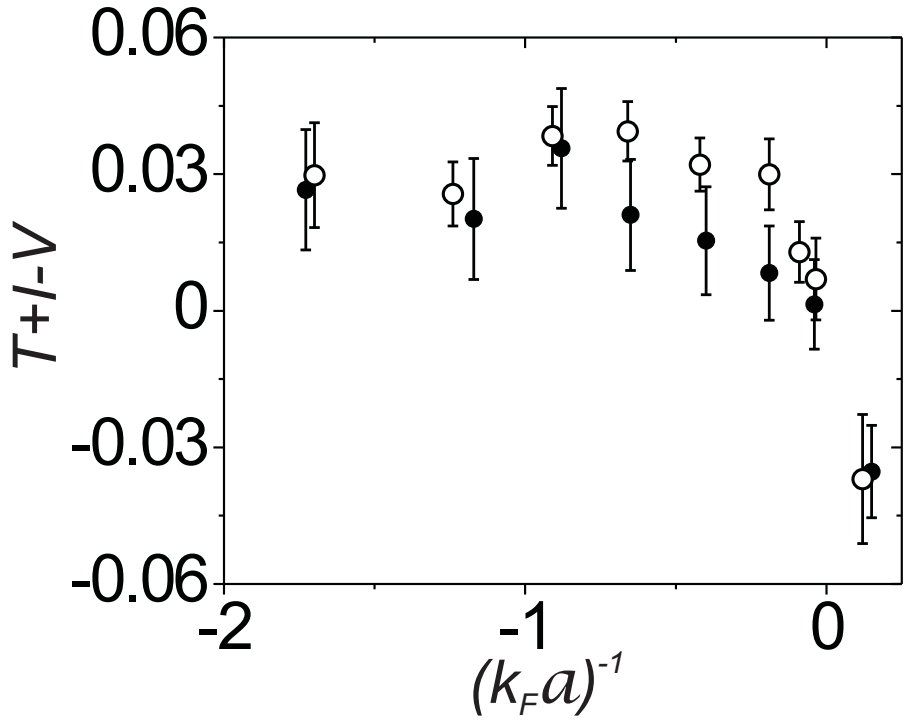

Figure 8.4: **Testing the generalized virial theorem** The difference between the measured release energy and potential energy per particle $T + I - V$ is shown as filled circles. This corresponds to the left hand side of Eq. 8.5. Open circles show the right hand side of Eq. 8.5 obtained from the average values of the contact shown in Fig. 8.2. The two quantities are equal to within the measurement uncertainty.

[103, 104], namely the adiabatic sweep theorem and the generalized virial theorem. These universal relations represent a significant advance in the understanding of many-body quantum systems with strong short-range interactions. Furthermore, these relations could be exploited to develop novel experimental probes of the many-body physics of strongly interacting quantum gases.

Chapter 9

Conclusion and Outlook

9.1 Summary

In this thesis, I presented ultracold atomic Fermi gases as an ideal system for studying the effects of strong interactions in quantum systems. Feshbach resonances are the key tool that allow us to vary the interaction strength between atoms in the gas and enter into the regime of the BCS-BEC crossover. In the crossover, strong interactions cause the fermions to form pairs with a typical pair size on order of the interparticle spacing. This pair size puts the system well beyond the reach of the standard BCS theory of pairing but not yet to the limit where the pairs can be understood as two-body molecules. Instead, the gas is a strongly correlated manybody system.

I introduced an atom photoemission spectroscopy technique, which is based on momentum-resolved rf spectroscopy, to probe the strongly interacting Fermi gas in the BCS-BEC crossover. This technique allows one to directly measure the energy and momentum of the occupied single-particle states in the strongly interacting system. This information can be used to construct the occupied spectral function and compare directly to many-body theories.

Using this method, we obtained atom photoemission data as a function of temperature and interaction strength in the crossover. This data shows many of the unusual features of the gas, including a pairing gap on order of the Fermi energy, large energy widths of the single-particle states, and the disappearance of the Fermi surface on the BEC side of the crossover. Perhaps the most unusual behavior of the gas revealed by the data is the persistence of a BCS-like dispersion above the superfluid transition temperature. This is strong evidence for the existence of a pseudogap

phase, consisting of incoherent pairs of fermions.

In order to understand the effect of the confinement trap on the photoemission data, I introduced a measurement technique to obtain spatially resolved momentum information in a trapped atomic gas. We demonstrated that this technique allows for the direct observation of the Fermi surface in a weakly interacting Fermi gas. We then applied this technique to study the effects of the harmonic trapping potential for the Fermi gas on the photoemission data.

Finally, I presented measurements of the amplitude of the large-momentum tail of the fermion momentum distribution, termed the contact. I showed how this quantity could be linked to a number of other measurable quantities in the system, such as the rf spectrum, total energy, and virial theorem. The relations involving the contact are known as the Tan relations and are valid for all interaction strengths and phases of the system (normal, superfluid, ect.). As such, they represent an important new development in the study of strongly interacting systems with short-range interactions.

9.2 Outlook

In the short-to-medium term, I believe there are some interesting research opportunities related to the issues presented in the last two chapters of this thesis. As far as photoemission spectroscopy in the BCS-BEC crossover goes, I think obtaining a spectrum for a homogeneous gas is a worthy goal. In Chapter 7, we were able to see some of the effects of the trapping potential on the data. However, the hollow light beam technique by itself is inadequate to obtain a spectrum for a gas with density profile homogeneous enough to divide out the Fermi function from the photoemission data. The spectral function of a homogeneous gas would be a great help in comparing directly to theories of the pseudogap and developing a better understanding of the properties of this strongly correlated system. For example, it would allow one to directly measure the gap in the density of states. In order to improve upon the current results, it may be necessary to consider modifying the trapping potential to be flatter in the center. The most difficult part of making a box trap is obtaining sharp edges at the boundaries. However, the hollow light beam

technique is excellent for removing atoms at the edge of the cloud. Thus, a box trap is not necessary. For example, a quartic trapping potential ($V(r) \propto r^4$) might prove adequate. Other experiments in our field have demonstrated the kind of beam shaping control necessary to achieve this. Without data for a homogeneous gas, I fear that some questions regarding the pseudogap phase could go unresolved, such as the energy widths of the single-particle states near the Fermi surface and the magnitude and temperature dependence of the pseudogap in the density of states. Of course, other measurement techniques could also shed light on the pseudogap phase, such as measurements of the spin susceptibility [92].

Our work in Chapter 8 on the contact shows that measurements of this quantity can be a useful tool for probing a strongly interacting gas. As with photoemission spectroscopy, measurements of the contact for a homogeneous gas would be desirable. For example, the same theory we have compared to our photoemission data also predicts a sharp increase in the contact near the T_c [122]. However, it is predicted that this increase cannot be seen in a trapped gas with inhomogeneous density [122]. Luckily, measuring the contact for a homogeneous gas is significantly easier than photoemission spectroscopy for a homogeneous gas. This is because the contact can be obtained directly from momentum integrated rf spectra. In fact, spatially resolved rf spectroscopy has already been demonstrated in Ref. [97]. However, in Ref. [97] the fermion studied was ^{6}Li, where rf spectroscopy is complicated by the absence of a weakly interacting third spin state [40]. Thus our experiment with ^{40}K would have a distinct advantage. Measurements of the contact for a homogeneous gas as a function of temperature and interaction strength would be an important benchmark for theories and could help us develop a better understanding of the crossover. Furthermore, the behavior of the contact near T_c could give information about the pseudogap state and the nature of the superfluid transition.

The medium-to-long term outlook is, obviously, more difficult to predict. It seems already that the projects we deem most promising, even in the short term, can completely change on a dime when interesting results are presented by other experimental and theoretical groups. As such, the most likely thing to happen is there will be new predictions and observations regarding strongly

interacting fermions that our experiment will be well suited to study. One recent development that appears to remain an open question is the potential observation of a ferromagnetic state for strongly repulsive fermions [57]. It would also be interesting to study Fermi liquid behavior in a low temperature repulsive Fermi gas using photoemission spectroscopy or other means. Non-equilibrium and dynamic behavior of strongly interacting quantum gases is a rich field with many open questions. The ability to quickly change the magnetic field and thus the interaction strength means we can excite dynamic behavior. For example, measuring the time-dependence of the contact after a magnetic field jump could be interesting, possibly using time-resolved photoemission spectroscopy. Also, it has been pointed out that the value of the contact can be related to the shear viscosity of a strongly interacting Fermi gas, which may itself may be approaching a lower limit predicted by string theory [101].

Eventually, one can consider adding a degree of complexity to our system. Reducing the dimensionality via an optical lattice is an obvious possibility. The lower dimension could suppress superfluidity and allow one to study the normal state down to lower temperature [12], perhaps also sheading light on the physics of the pseudogap phase. The two-dimensional Fermi-Hubbard model still remains the holy grail of atomic Fermi gas experiments and there are promising proposals for reducing the entropy enough to observe magnetic behavior and map out the low-temperature phase diagram [123].

Regardless, as experimenters develop new techniques and more sophisticated measurements to test theoretical predictions and study many-body quantum phenomena there is sure to be dramatic and exciting progress in this field over the next several years. I look forward to following those developments.

Bibliography

[1] C. A. Regal and D. S. Jin, Measurement of positive and negative scattering lengths in a Fermi gas of atoms, *Phys. Rev. Lett.* **90**, 230404 (2003).

[2] J. P. Gaebler, J. T. Stewart, J. L. Bohn, and D. S. Jin, p-wave Feshbach molecules, *Phys. Rev. Lett.* **98**, 200403 (2007).

[3] D. S. Jin, J. P. Gaebler, and J. T. Stewart, in *Proceedings of the International Conference on Laser Spectroscopy, Telluride 2007*, edited by L. Hollberg, J. Berquist, and M. Kasevich (World Scientific, 2008).

[4] W. Ketterle and M. W. Zwierlein, in *Proceedings of the International School of Physics "Enrico Fermi", Course CLXIV*, edited by M. Inguscio, W. Ketterle, and C. Salomon (OS PressAmsterdam, 2008).

[5] J. R. Schrieffer, in *Theory of Superconductivity*, edited by D. Pines (Addison-Wesley Publishing Company, Inc., 1964).

[6] C. A. Regal, Experimental realization of BCS-BEC crossover physics with a Fermi gas of atoms, Ph.D. thesis, University of Colorado, 2006.

[7] C. A. Regal, M. Greiner, and D. S. Jin, Observation of resonance condensation of fermionic atom pairs, *Phys. Rev. Lett.* **92**, 040403 (2004).

[8] A. Damascelli, Z. Hussain, and Z. Shen, Angle-resolved photoemission studies of the cuprate superconductors, *Reivews of Modern Physics* **75**, 473 (2003).

[9] J. T. Stewart, J. P. Gaebler, and D. S. Jin, Using photoemission spectroscopy to probe a strongly interacting Fermi gas, *Nature* **454**, 744 (2008).

[10] J. T. Stewart, J. P. Gaebler, T. E. Drake, and D. S. Jin, Verification of universal relations in a strongly interacting Fermi gas, *Phys. Rev. Lett.* **104**, 235301 (2010).

[11] S. Tsuchiya, R. Watanabe, and Y. Ohashi, Single-particle properties and pseudogap effects in the BCS-BEC crossover regime of an ultracold Fermi gas above T_c, *Phys. Rev. A* **80**, 033613 (2009).

[12] Q. Chen, J. Stajic, and K. Levin, Applying BCS-BEC crossover theory to high temperature superconductors and ultracoldatomic Fermi gases, *Low Temp. Phys.* **32**, 406 (2006).

[13] S. Nascimbene, N. Navon, K. Jiang, F. Chevy, and C. Salomon, Exploring the thermodynamics of a universal Fermi gas, *Nature* **463**, 1057 (2010).

[14] A. Bulgac, J. E. Drut, and P. Magierski, Spin 1/2 fermions in the unitary regime: a superfluid of a new type, *Phys. Rev. Lett.* **96**, 090404 (2006).

[15] A. Perali, P. Pieri, G. C. Strinati, and C. Castellani, Pseudogap and spectral function from superconducting fluctuations to the bosonic limit, *Phys. Rev. B* **66**, 024510 (2002).

[16] A. Perali, P. Pieri, P. F., G. C. Strinati, J. T. Stewart, J. P. Gaebler, T. E. Drake, and D. S. Jin, Pseudogap phase and remnant Fermi surface in ultracold Fermi Gases, , arXiv: 1006.3406.

[17] W. Schneider and M. Randeria, Universal short-distance structure of the single-particle spectral function of dilute Fermi gases, *Phys. Rev. A* **81**, 021601 (2010).

[18] J. P. Gaebler, J. T. Stewart, T. E. Drake, D. S. Jin, A. Perali, P. Pieri, and G. C. Strinati, Observation of pseudogap behavior in a strongly interacting Fermi gas, *Nature Physics* **6**, 569 (2010).

[19] A. Schirotzek, Y. il Shin, C. H. Schunck, and W. Ketterle, Determination of the superfluid gap in atomic Fermi gases by quasiparticle spectroscopy, *Phys. Rev. Lett.* **101**, 140403 (2008).

[20] A. Bulgac, J. E. Drut, and P. Magierski, Quantum Monte Carlo simulations of the BCS-BEC crossover at finite temperature, *Phys. Rev. A* **78**, 023625 (2008).

[21] G. E. Astrakharchik, J. Boronat, J. Casulleras, and S. Giorgini, Equation of state of a Fermi gas in the BEC-BCS crossover: A quantum Monte Carlo study, *Phys. Rev. Lett.* **93**, 200404 (2004).

[22] F. Werner, L. Tarruel, and Y. Castin, Number of closed-channel molecules in the BEC-BCS crossover, *Eur. Phys. J. B* **68**, 401 (2009).

[23] M. H. Anderson, J. R. Ensher, M. R. Matthews, C. E. Wiemand, and E. A. Cornell, Observation of Bose-Einstein condensate in a dilute atomic vapor, *Science* **269**, 198 (1995).

[24] C. C. Bradley, C. A. Sackett, J. J. Tollett, and R. G. Hulet, Evidence of Bose-Einstein condensation in an atomic gas with attractive interactions, *Phys. Rev. Lett.* **75**, 1687 (1995).

[25] K. B. Davis, M. O. Mewes, M. R. Andrews, N. J. van Druten, D. S. Durfee, D. M. Kurn, and W. Ketterle, Bose-Einstein condensation in a gas of sodium atoms, *Phys. Rev. Lett.* **75**, 3696 (1995).

[26] W. Ketterle, in *Nobel Prizes 2001* (Nobel Foundation, 2001).

[27] P. W. Anderson, More Is Different, *Science* **177**, 4047 (1972).

[28] in *Open Problems in Strongly Correlated Electron Systems*, Proceedings of the NATO Advanced Research Workshop in Bled, Slovenia, 26-30 April 2000, edited by J. Bonca, P. Prelovsek, R. A., and S. Sarkar (NATO Sicence Series II: Mathematics, Physics and Chemistry, Vol. 15, 2001).

[29] H. Heiselberg, Fermi systems with long scattering lengths, *Phys. Rev. A* **63**, 043606 (2001).

[30] J. T. Stewart, J. P. Gaebler, C. A. Regal, and D. S. Jin, Potential energy of a ^{40}K Fermi gas in the BCS-BEC crossover, *Phys. Rev. Lett.* **97**, 220406 (2006).

[31] E. Shuryak, Strongly coupled quark-gluon plasma: the status report, *Prog. Part. Nucl. Phys.* **53**, 273 (2004).

[32] G. A. Baker, Neutron matter model, *Phys. Rev. C* **60**, 054311 (1999).

[33] B. DeMarco, Quantum behavior of an atomic Fermi gas, Ph.D. thesis, University of Colorado, 2001.

[34] J. T. Stewart, Probing a strongly interacting Fermi gas, Ph.D. thesis, University of Colorado, 2009.

[35] V. Gurarie and L. Radzihovsky, Resonantly-paired fermionic superfluids, *Annals of Physics* **322**, 2 (2007).

[36] J. J. Sakurai, in *Modern Quantum Mechanics*, edited by S. F. Tuan (Addison-Wesley Publishing Company, Inc., 1985).

[37] R. B. Diener and T.-L. Ho, The condition for universality at resonance and direct measurement of pair wavefunctions using rf spectroscopy, (2004), arXiv:cond-mat/0405174v2.

[38] C. Ticknor, C. A. Regal, D. S. Jin, and J. L. Bohn, Multiplet structure of Feshbach resonances in non-zero partial waves, *Phys. Rev. A* **69**, 042712 (2004).

[39] C. A. Regal, C. Ticknor, J. L. Bohn, and D. S. Jin, Creation of ultracold molecules from a Fermi gas of atoms, *Nature* **424**, 47 (2003).

[40] C. H. Schunck, Y. i. Shin, A. Schirotzek, and W. Ketterle, Determination of the fermion pair size in a resonantly interacting superfluid, *Nature* **454**, 739 (2008).

[41] T. Loftus, C. A. Regal, C. Ticknor, J. L. Bohn, and D. S. Jin, Resonant control of elastic collisions in an optically trapped Fermi gas of atoms, *Phys. Rev. Lett.* **88**, 173201 (2002).

[42] M. Greiner, C. A. Regal, and D. S. Jin, Probing the excitation spectrum of a Fermi gas in the BCS-BEC crossover regime, *Phys. Rev. Lett.* **94**, 070403 (2005).

[43] C. A. Regal, C. Ticknor, J. L. Bohn, and D. S. Jin, Tuning p-wave interactions in an ultracold Fermi gas of atoms, *Phys. Rev. Lett.* **90**, 053201 (2003).

[44] C. A. Regal, M. Greiner, and D. S. Jin, Lifetime of molecule-atom mixtures near a Feshbach resonance in 40K, *Phys. Rev. Lett.* **92**, 083201 (2004).

[45] S. Durr, V. T., and G. Rempe, Dissociation of ultracold molecules with Feshbach resonances, *Phys. Rev. A* **70**, 031601(R) (2004).

[46] Y. Inada, M. Horikoshi, S. Nakajima, M. K. Kuwata-Gonokami, M. Ueda, and T. Mukaiyama, Collisional properties of p-wave Feshbach molecules, *Phys. Rev. Lett.* **101**, 100401 (2008).

[47] J. Fuchs, C. Ticknor, P. Dyke, G. Veeravalli, E. Kuhnle, W. Rowlands, P. Hannaford, and C. J. Vale, Binding energies of ^6Li p-wave Feshbach molecules, *Phys. Rev. A* **77**, 053616 (2008).

[48] J. Levinson, N. R. Cooper, and V. Gurarie, Stability of fermionic gases close to a p-wave Feshbach resonance, *Phys. Rev. A* **78**, 063616 (2008).

[49] V. Gurarie, L. Radzihovsky, and A. V. Andreev, Quantum phase transitions across p-wave Feshbach resonance, *Phys. Rev. Lett.* **94**, 230403 (2005).

[50] C.-H. Cheng and S.-K. Yip, Anisotropic Fermi superfluid via p-wave Feshbach resonance, *Phys. Rev. Lett.* **95**, 070404 (2005).

[51] Y. Ohashi, BCS-BEC crossover in a gas of Fermi atoms with a p-wave Feshbach resonance, *Phys. Rev. Lett.* **94**, 050403 (2005).

[52] S. S. Botelho and C. A. R. S. de Melo, Quantum phase transition in the BCS-to-BEC evolution of p-wave Fermi gases, *J. Low Temp. Phys.* **140**, 409 (2005).

[53] N. Read and D. Green, Paired states of fermions in two dimensions with breaking of parity and time-reversal symmetries, and the fractional quantum Hall effect, *Phys. Rev. B* **61**, 10267 (2000).

[54] R. A. W. Maier, C. Marzok, and C. Zimmermann, Radio-frequency spectroscopy of ^6Li p-wave molecules: Towards photoemission spectroscopy of a p-wave superfluid, *Phys. Rev. A* **81**, 064701 (2010).

[55] Y. J. Han, C. Y. H., A. J. Daley, S. Diehl, P. Zoller, and L. M. Duan, Stabilitzation of the p-wave superfluid state in an optical lattice, *Phys. Rev. Lett.* **103**, 070404 (2009).

[56] A. L. Fetter and J. D. Walecka, *Quantum Theory of Many-Particle Systems* (Dover PublicationsMineola, New York, 1971).

[57] G. B. Jo, Y. Lee, J. H. Choi, C. A. Christensen, T. H. Kim, J. H. Thywissen, D. E. Pritchard, and W. Ketterle, Itinerant gerromagnetism in a Fermi gas of ultracold atoms, *Science* **325**, 1521 (2009).

[58] L. N. Cooper, Bound electron pairs in a degenerate Fermi gases, *Phys. Rev.* **104**, 1159 (1956).

[59] A. J. Leggett, Cooper pairing in spin-polarized Fermi systems., *J. Phys. C (Paris)* **41**, C7 (1980).

[60] P. Nozieres and S. Schmitt-Rink, Bose condensation in an attractive fermion gas: from weak to strong coupling superconductivity, *J. of Low Temp. Phys.* **59**, 195211 (1985).

[61] M. Randeria, J. M. Duan, and L. Y. Shieh, Superconductivity in two-dimensional Fermi gas: Evolution form Cooper pairing to Bose condensation, *Phys. Rev. B* **41**, 327 (1990).

[62] M. W. Zwierlein, J. R. Abo-Shaeer, A. Schirotzek, C. H. Schunck, and W. Ketterle, Vortices and superfluidity in a strongly interacting Fermi gas, *Nature* **435**, 1047 (2005).

[63] J. Kinast, A. Turlapov, J. E. Thomas, Q. Chen, J. Stajic, and K. Levin, Heat capacity of astronglyinteracting Fermi gas, *Science* **307**, 1296 (2005).

[64] J. Kinast, S. L. Hemmer, M. E. Gehm, A. Turlapov, and J. E. Thomas, Evidence for superfluidity in a resonantly interacting Fermi gas, *Phys. Rev. Lett.* **92**, 150402 (2004).

[65] M. Bartenstein, A. Altmeyer, S. Riedl, S. Jochim, C. Chin, J. H. Denschlag, and R. Grimm, Collective excitations of a degenerate gas at the BEC-BCS crossover, *Phys. Rev. Lett* **92**, 203201 (2004).

[66] Q. Chen, J. Stajic, and K. Levin, Thermodynamics of Interacting Fermions in Atomic Traps, *Phys. Rev. Lett.* **95**, 260405 (2005).

[67] C. A. Regal, M. Greiner, S. Giorgini, M. Holland, and D. S. Jin, Momentum distribution of a Fermi gas of atoms in the BCS-BEC crossover, *Phys. Rev. Lett.* **95**, 250404 (2005).

[68] P. Nozieres, in *Theory of Interacting Fermi Systems*, edited by D. Pines (Addison-Wesley Publishing Company, Inc., 1964).

[69] P. Noziéres and D. Pines, *The Theory of Quantum Liquids, Vol. I Normal Fermi Liquids* (Addison-WesleyCambridge, Massachusetts, 1966).

[70] R. Haussmann, M. Punk, and W. Zwerger, Spectral functions and rf response of ultracold fermionic atoms, *Phys. Rev. A* **80**, 063612 (2009).

[71] P. Massignan, G. M. Bruun, and H. T. C. Stoof, Twin peaks in rf spectra of Fermi gases at unitarity, *Phys. Rev. A* **77**, 031601(R) (2008).

[72] Q. Chen and K. Levin, Probing the spectral function using momentum resolved radio frequency spectroscopy in trapped Fermi gases, *Phys. Rev. Lett.* **102**, 190402 (2009).

[73] This interaction strength is calculated using the Feshbach resonance calibration of Chap. 3 and so is different that what is reported in [9].

[74] C. Chin and P. S. Julienne, Radio-frequency transitions on weakly bound ultracold molecules., *Phys. Rev. A* **71**, 012713 (2005).

[75] C. Chien, H. Guo, Y. He, and K. Levin, Comparative study of BCS-BEC crossover theories above T_c: the nature of the pseudogap in ultra-cold atomic Fermi gases, *Phys. Rev. A* **81**, 023622 (2010).

[76] A. Kanigel, C. U., M. Randeria, M. R. Norman, G. Koren, K. Kadowaki, and J. C. Campuzano, Evidence for pairing above T_c from the dispersion in the pseudogap phase of cuprates, *Phys. Rev. Lett* **101**, 137002 (2008).

[77] M. Shi. *et al.*, Spectroscopic evidence for preformed Cooper pairs in the pseudogap phase of cuprates, *EPL* **88**, 27008 (2009).

[78] H. B. Yang, J. D. Rameau, P. D. Johnson, T. Valla, A. Tsvelik, and G. D. Gu, Emergence of preformed Cooper pairs from the doped Mott insulating state in $Bi_2Sr_2CaCu_2O_{8+\delta}$, *Nature* **456**, 6 (2008).

[79] K. Nakayama, T. Sato, Y. Sekiba, K. Terashima, P. Richard, T. Takahashi, K. Kudo, N. Okumura, T. Sasaki, and N. Kobayashi, Evolution of a pairing-induced pseudogap from the superconducting gap of $(Bi,Pb)_2Sr_2CuO_6$, *Phys. Rev. Lett.* **102**, 227006 (2009).

[80] M. Hashimoto *et al.*, Particle-hole symmetry breaking in the pseudogap state of Bi2201, *Nature Physics* **6**, 414 (2010).

[81] T. Kondo, R. Khasanov, T. Takeuchi, J. Schmalian, and A. Kaminski, Competition between the pseudogap and superconductivity in the high-Tc copper oxides, *Nature* **457**, 296 (2009).

[82] *Handbook of High-Temperature Superconductivity*, edited by J. R. Schrieffer and J. S. Brooks (Springer, 2007).

[83] M. Randeria, N. Trivedi, A. Moreo, and R. T. Scalettar, Pairing and spin gap in the normal state of short coherence length superconductors, *Phys. Rev. Lett.* **69**, 2001 (1992).

[84] C. A. R. Sá de Melo, M. Randeria, and J. R. Engelbrecht, Crossover from BCS to Bose superconductivity: Transition temperature and time-dependent Ginzburg-Landau theory, *Phys. Rev. Lett.* **71**, 3202 (1993).

[85] B. Janko, J. Maly, and K. Levin, Pseudogap effects induced by resonant pair scattering, *Phys. Rev. B* **56**, R11407 (1997).

[86] G. M. Bruun and G. Baym, Bragg spectroscopy of cold atomic Fermi gases, *Phys. Rev. A* **74**, 033623 (2006).

[87] P. Magierski, G. Wlazlowski, A. Bulgac, and J. E. Drut, The finite temperature pairing gap of a unitary Fermi gas by quantum Monte Carlo, *Phys. Rev. Lett.* **103**, 210403 (2009).

[88] C. Chin, M. Bartenstein, A. Altmeyer, S. Riedl, S. Jochim, J. H. Denschlag, and R. Grimm, Observation of the pairing gap in a strongly interacting Fermi gas, *Science* **305**, 1128 (2004).

[89] S. Nascimbene, Thermodynamics of ultracold Fermi gases, Ph.D. thesis, ENS, 2010.

[90] A. Bulgac, J. E. Drut, and P. Magierski, Thermodynamics of a trapped unitary Fermi gas, *Phys. Rev. Lett.* **99**, 120401 (2007).

[91] A. Bulgac, M. M. Forbes, and P. Magierski, in *BCS-BEC crossover and the unitary Fermi gas*, edited by W. Zwerger (Springer, 2011), Chap. The unitary Fermi gas: From Monte Carlo to density functionals.

[92] C. Chien and K. Levin, Fermi liquid theory of ultra-cold trapped Fermi gases: Implications for pseudogap physics and other strongly correlated phases, *Phys. Rev. A* **82**, 013603 (2010).

[93] S. Tsuchiya, R. Watanabe, and Y. Ohashi, Photoemission spectrum and effect of inhomogeneous pairing fluctuations in the BCS-BEC crossover regime of an ultracold Fermi gas:, *Phys. Rev. A* **82**, 033629 (2010).

[94] H. H., X.-J. Liu, P. D. Drummond, and H. Dong, Pseudo-gap pairing in ultracold Fermi atoms, *Phys. Rev. Lett.* **104**, 240407 (2010).

[95] E. Hodby, S. T. Thompson, C. A. Regal, M. Greiner, A. C. Wilson, D. S. Jin, E. A. Cornell, and C. E. Wieman, Production efficiency of ultra-cold Feshbach molecules in bosonic and fermionic systems, *Phys. Rev. Lett.* **94**, 120402 (2005).

[96] J. Carlson and S. Reddy, Superfluid pairing gap in strong coupling, *Phys. Rev. Lett.* **100**, 150403 (2008).

[97] Y. Shin, C. H. Schunck, A. Schirotzek, and W. Ketterle, Tomographic rf spectroscopy of a trapped Fermi gas at unitarity., *Phys. Rev. Lett.* **99**, 090403 (2007).

[98] N. R. Heckenberg, R. McDuff, C. P. Smith, H. Rubinsztein-Dunlop, and J. Wegener, Laser beams with phase singularities, *Optical and Quantum Electronics* **24**, S951 (1992).

[99] A. Perali, P. Pieri, and G. C. Strinati, Quantitaive comparison between theoretical predictions and experimental results for the BCS-BEC crossover, *Phys. Rev. Lett.* **93**, 100404 (2004).

[100] P. Pieri, L. Pisani, and G. C. Strinati, Comparison between a diagrammatic theory for the BCS-BEC crossover and quantum Monte Carlo results, *Phys. Rev. B* **72**, 012506 (2005).

[101] E. Taylor and M. Randeria, Viscosity of strongly interacting quantum fluids: spectral functions and sum rules, *Phys. Rev. A* **81**, 053610 (2010).

[102] S. Tan, Large momentum part of a strongly correlated Fermi gas, *Ann. Phys.* **323**, 2971 (2008).

[103] S. Tan, Generalized Virial Theorem and Pressure Relation for a strongly correlated Fermi gas, *Ann. Phys.* **323**, 2987 (2008).

[104] S. Tan, Energetics of a strongly correlated Fermi gas, *Ann. Phys.* **323**, 2952 (2008).

[105] E. Braaten, D. Kang, and L. Platter, Exact relations for a strongly-interacting Fermi gas from the operator product expansion, *Phys. Rev. Lett.* **100**, 205301 (2008).

[106] S. Zhang and A. J. Leggett, Universal properties of the ultracold Fermi gas, *Phys. Rev. A* **79**, 023601 (2009).

[107] E. D. Kuhnle, H. Hu, X.-J. Liu, P. Dyke, M. Mark, P. D. Drummond, P. Hannaford, and C. J. Vale, Universal behavior of pair correlations in a strongly interacting Fermi gas, *Phys. Rev. Lett.* **105**, 070402 (2010).

[108] E. Braaten, in *Universal relations for Fermions with large scattering length*, edited by W. Zwerger (Springer, 2011).

[109] G. B. Partridge, K. E. Strecker, R. I. Kamar, M. W. Jack, and R. G. Hulet, Molecular probe of pairing in the BEC-BCS crossover, *Phys. Rev. Lett.* **95**, 020404 (2005).

[110] N. Navon, S. Nascimbene, F. Chevy, and C. Salomon, The equation of state of a low-temperature Fermi gas with tunable interactions, *Science* **328**, 5979 (2010).

[111] P. Pieri, A. Perali, and G. C. Strinati, Enhanced paraconductivity-like fluctuations in the radio frequency spectra of ultracold Fermi atoms, *Nat. Phys.* **5**, 736 (2009).

[112] W. Schneider, V. B. Shenoy, and M. Randeria, Theory of Radio Frequency Spectroscopy of Polarized Fermi Gases, arXiv:0903.3006v1 (unpublished).

[113] E. Braaten, D. Kang, and L. Platter, Short-time operator product expansion for rf spectroscopy of a strongly interacting Fermi gas, *Phys. Rev. Lett.* **104**, 223004 (2010).

[114] Z. Yu and G. Baym, Spin-correlation functions in ultracold paired atomic-fermion systems: Sum rules, self-consistent approximations, and mean fields., *Phys. Rev. A* **73**, 063601 (2006).

[115] M. Punk and W. Zwerger, Theory of rf-spectrscopy of strongly interacting fermions., *Phys. Rev. Lett.* **99**, 170404 (2007).

[116] S. Basu and E. J. Mueller, Final-state effects in the radio frequency spectrum of strongly interacting fermions, *Phys. Rev. Lett.* **101**, 060405 (2008).

[117] A. Perali, P. Pieri, and G. C. Strinati, Competition between final-state and pairing gap effects in the radio-frequency spectra of ultracold Fermi atoms., *Phys. Rev. Lett.* **100**, 010402 (2008).

[118] M. Veillette, E. G. Moon, A. Lamacraft, L. Radzihovsky, S. Sachdev, and D. E. Sheehy, Radio frequency spectroscopy of a strongly imbalanced Feshbach-resonant Fermi gas, *Phys. Rev. A* **78**, 033614 (2008).

[119] Y. He, C. C. Chien, Q. Chen, and K. Levin, Radio frequency spectroscopy of trapped Fermi gases with population imbalance, *Phys. Rev. A* **77**, 011602 (2008).

[120] T. Bourdel, J. Cubizolles, L. Khaykovich, K. M. F. Magalhães, S. J. J. M. F. Kokkelmans, G. V. Shlyapnikov, and C. Salomon, Measurement of the interaction energy near a Feshbach resonance in a ^{6}Li Fermi gas, *Phys. Rev. Lett.* **91**, 020402 (2003).

[121] K. M. O'Hara, S. L. Hemmer, M. E. Gehm, S. R. Granade, and J. E. Thomas, Observation of a strongly interacting degenerate Fermi gas of atoms, *Science* **298**, 2179 (2002).

[122] F. Palestini, A. Perali, P. Pieri, and G. C. Strinati, Temperature and coupling dependence of the universal contact intensity for an ultracold Fermi gas, *Phys. Rev. A* **82**, 021605(R) (2010).

[123] T.-L. Ho and Q. Zhou, Universal colling scheme for quantum simulation, arXiv:0911.5506v1 (unpublished).

[124] A. Corney, *Atomic Laser Spectroscopy* (Clarendon Press, Oxford, 1977).

[125] E. Arimondo, M. Inguscio, and P. Violino, Experimental determinations of the hyperfine strucutre in the alkali atoms, *Rev. Mod. Phys.* **49**, 31 (1977).

[126] R. Jördens *et al.*, Quantitative determination of temperature in the approach to magnetic order of ultracold fermions in an optical lattice, *Phys. Rev. Lett.* **104**, 180401 (2010).

Appendix A

^{40}K Transitions

In a number of places in this thesis I discuss various optical transitions ^{40}K atoms in a magnetic field. In this section, I explain how the energy and branching ratios for these transitions are calculated and list all the transitions for ^{40}K atoms that are relevant for this thesis. The references for this section are the book on laser spectroscopy, Ref. [124], and the review article containing measurements of the hyperfine structure in alkali atoms, Ref. [125]. Also, when I wrote the MATLAB program for this, I borrowed from a Mathematic code written by Jayson Stewart that was a final project for his graduate atomic physics class. A ^{40}K atom has nuclear spin $I = 4$ and electronic spin $S = 1/2$. In the ground state ($4S_{1/2}$), where the orbital angular momentum L is zero, we have $J = L + S = 1/2$. The total angular momentum $F = J + I$ can be either $9/2$ or $7/2$. The $F = 9/2$ hyperfine state is the lower energy state that we use for experiments. The relevant electronic transitions are to states with $L = 1$ and $J = 3/2$ ($4P_{3/2}$), which are called $D2$ transitions. The electronically excited state can have $F' = 11/2, 9/2, 7/2, 5/2$, where the prime signifies we are talking about the excited state.

To compute the Zeeman shifts of the hyperfine states, one needs to diagonalize the Hamiltonian $H_{HFS}(B) = H_{HFS} + H_Z$. The hyperfine Hamiltonian H_{HFS} can be written

$$H_{HFS} = \frac{1}{2}hA_JK + hB_J\frac{\frac{3}{2}K(K+1) - 2I(I+1)J(J+1)}{2I(2I-1)2J(2J-1)} \tag{A.1}$$

where $K = 2I \cdot J = F(F+1) - I(I+1) - J(J+1)$, A_J is the magnetic hyperfine structure constant, and B_J is the electric quadrupole interaction constant. For a magnetic field of strength B along

the z axis, the interaction with the magnetic field is described by H_Z and can be written

$$H_Z = \mu_B B(g_j m_j + g_i \frac{\mu_N}{\mu_B} m_i) \tag{A.2}$$

where m_j and m_i are the projections of J and I along the z-axis, μ_B is the bohr magneton, μ_N is the nuclear magneton, and g_j and g_i are the g-factors for the electron and nuclear magnetic moments. The Lande g-factor, g_j depends on the g-factor for the electron, g, and can be written $g_j = \frac{g}{2}(1 + \frac{J(J+1)+S(S+1)-L(L+1)}{2J(J+1)})$.

J,I,L,S and the total spin projection, m_F, are all good quantum numbers at any field, while F is also a good quantum number at $B = 0$. We label all the states by F and m_F, where F then refers to the value for that state at $B = 0$.

The physical constants necessary are $g = 2.002319$, $g_I = -0.3245$, $\mu_B = 1.3996$ MHz/G, $\mu_N/\mu_B = 0.000544617$. For the ground state, $A_J = -285.7308$ and $B_J = 0$. For the excited state, $A_J = -7.59$ and $B_J = -3.5$.

Figures A.1,A.2, and A.3, show all the $D2$ transitions from the three lowest energy Zeeman levels in the $F = 9/2$ ground state at 202.2 G. Next to each excited state, the detuning (in MHz), and transition strength are shown for the transition indicated. The values are calculated for a magnetic-field strength of $B = 202.2$ G (the location of the s-wave Feshbach resonance). The detuning is calculated from the difference in energies obtained for the states after diagonalizing the Hamiltonian $H = H_{HFS} + H_Z$. The transition strength is obtained by calculating the transition matrix element between the new eigen-states. The probability that an atom in one of the excited states will spontaneously decay into a particular ground state is equal to the transition strength (i.e. a transition strength of 0.02 implies a 1 in 50 chance to decay to that state).

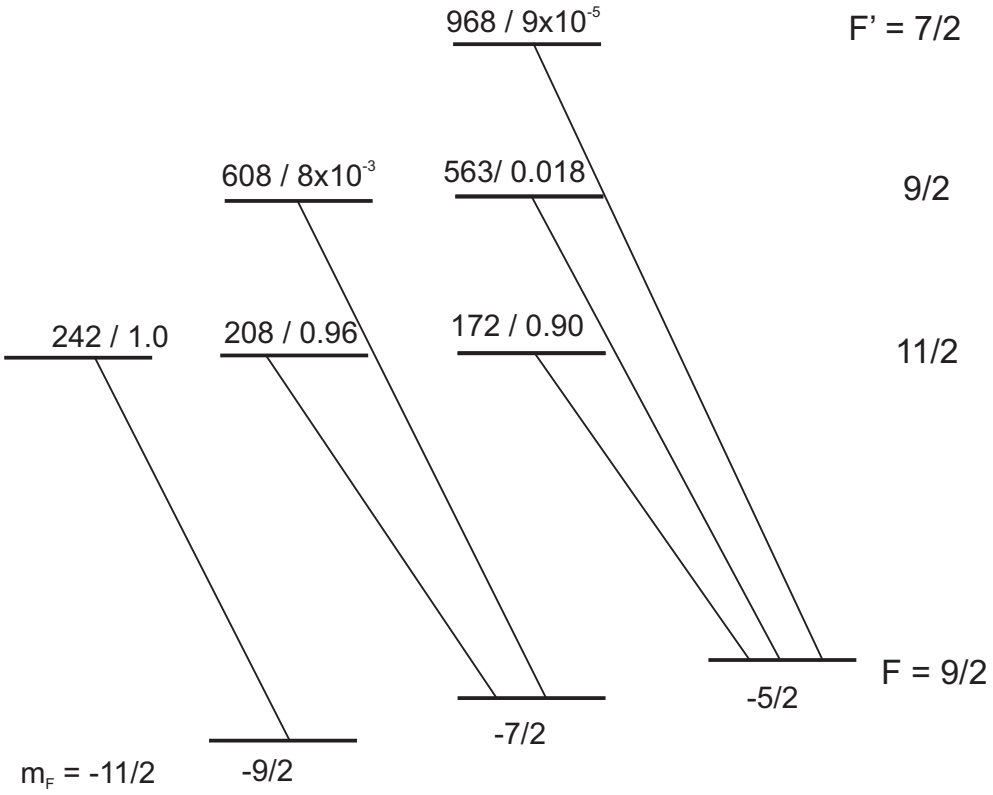

Figure A.1: $\sigma-$ **Transitions**.

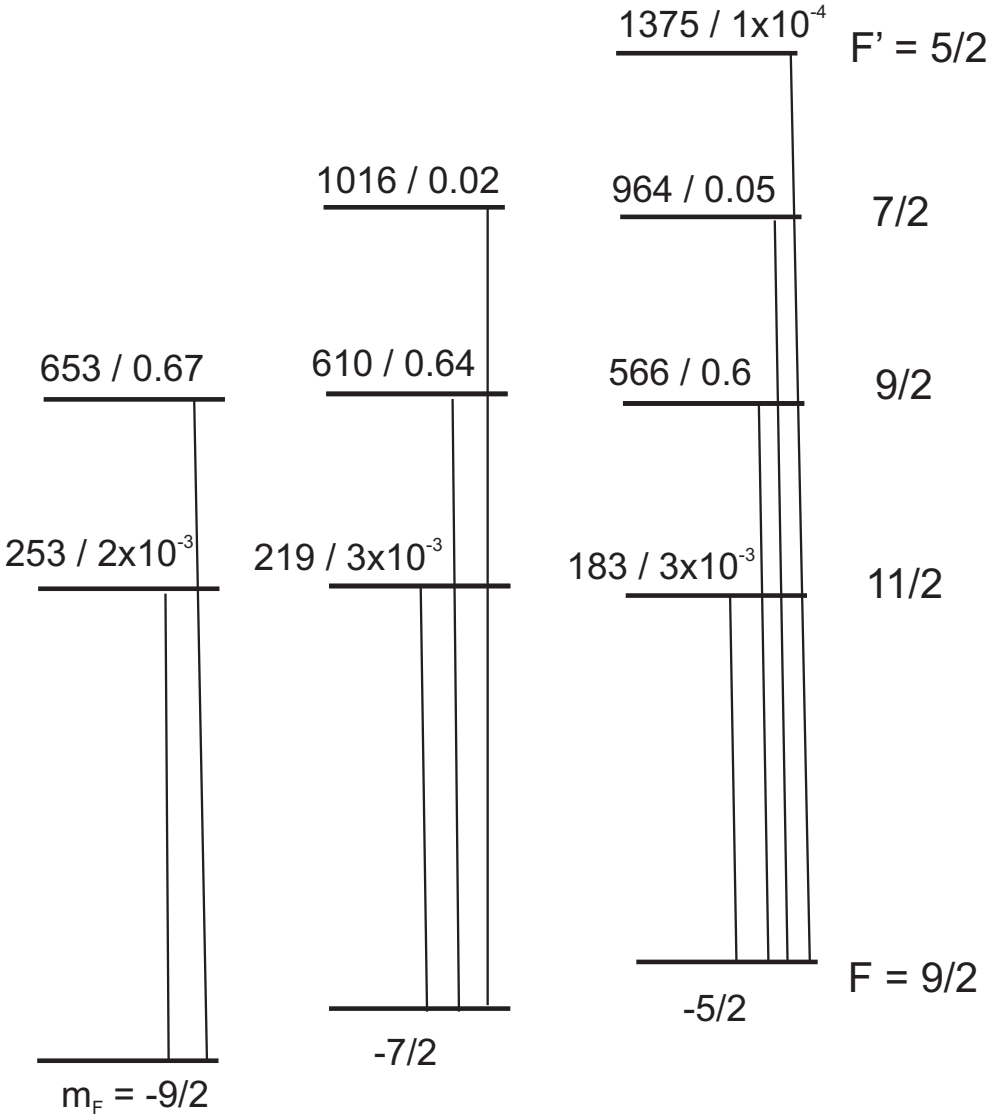

Figure A.2: π **Transitions**

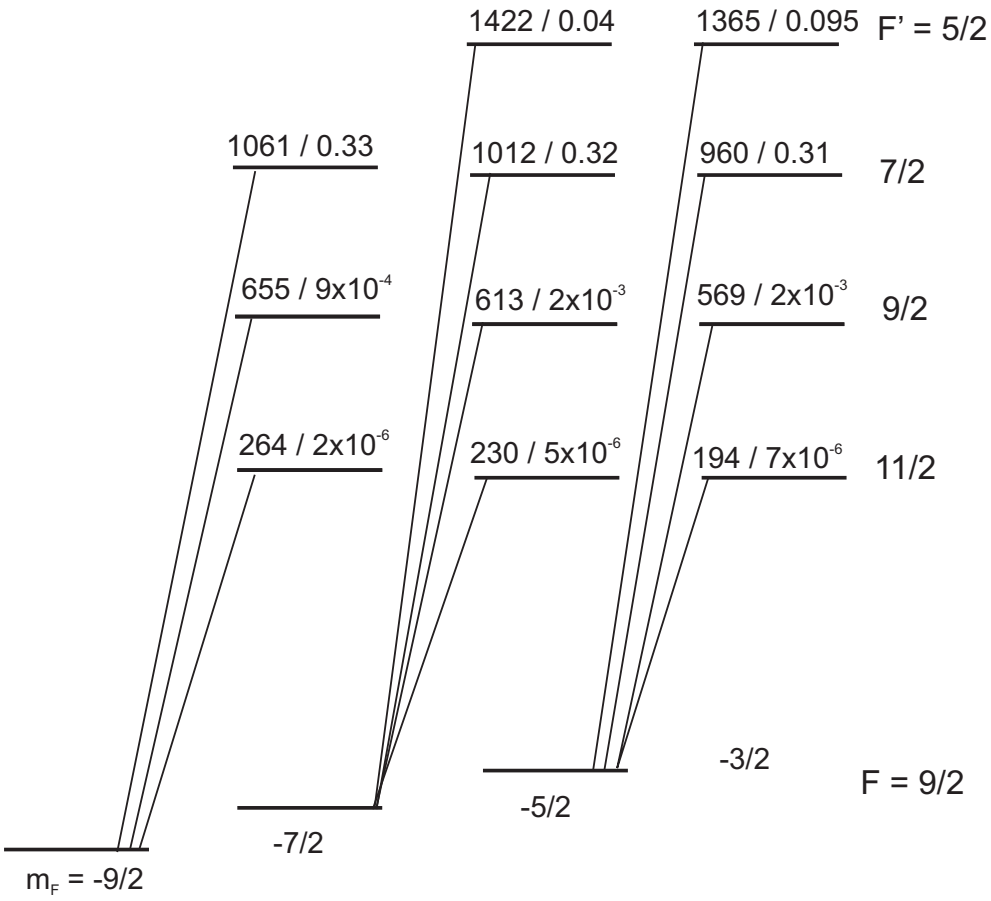

Figure A.3: $\sigma+$ **Transitions**

Appendix B

Subtracting the high-momentum background signal from optical pumping

In chapter 7, I presented a technique for measuring the momentum distribution of atoms from the center of a trapped gas using intersecting hollow light beams to optically pump atoms at large radius from the trap center. It was noted that this optical pumping is not perfectly efficient, and leaves some atoms in the same state with an extra momentum kick due to absorbing and spontaneously emitting a photon. We subtract this background using a simple model. Fig. 7.3 shows the measured atom momentum distribution with, and without the hollow light beams, as well as the predicted background contribution. In this appendix, I will sketch out the details of the model.

The first question to address is: how large do we expect the background signal to be based on the branching ratio of the optical pump transition? This calculation is easily done for a cloud at zero temperature. The density profile of the atoms is given by $n = n_0(1 - \frac{r^2}{R_{TF}}^2)^{3/2}$, where $r^2 = x^2 + y^2 + (\frac{z}{\lambda})^2$ and λ is the ratio of axial (along $\hat{z}$) to the radial (the (x-y) plane) trap frequency and R_{TF} is the Fermi radius in the radial direction, given by $R_{TF} = \sqrt{\frac{2E_F}{m\omega^2}}$. In our experiment $\lambda \approx 10$. A hollow light beam of order l has a profile given by Eq. 7.1. For a closed transition, the probability for an atom to absorb a certain number of photons, $P(N)$ is given by a Poissonian distribution $P(N) = e^{-I}\frac{I^N}{N!}$, where I corresponds to the mean number of photons absorbed per atom. For a non-cycling transition, with a probability T for the excited state to decay back into the original state, the probability that an atom absorbs a single photon and falls back into the original state is $TP(1)$. The probability to absorb two photons and still be in the original

state is $T^2P(2)$, which we will consider to be negligible as $T \ll 1$ for the transitions considered.

We consider a single, cylindrical hollow light beam with either $l = 1$ and $w = 1.1R_{TF}$ propagating along the axial direction ($\hat{z}$) or an $l = 2$ and $w = \lambda 0.75R_{TF}$ propagating perpendicular to the axial direction (along $\hat{y}$). To compute the number of atoms that fall back into the same state, we calculate the intensity of the light beam at each position in the cloud using Eq. 7.1, and the corresponding probability to absorb a single photon and fall back into the original state. For the $l = 1$ beam, we find the number of atoms absorbing a single photon and falling back into the same state as a fraction of the total initial number of atoms is approximately $1.12TN(0)(1-N(0))$ where $N(0)$ is the faction of atoms that absorbed 0 photons (the fraction of atoms remaining after the optical pumping excluding those that spontaneously decayed back to the original state). For the $l = 2$ beam we find the number to be approximately $0.37T\sqrt{N(0)(1-N(0))}$.

The atoms that absorb a photon and fall back into the same state will receive two momentum kicks equal to the photon recoil $k_0 = h\frac{2\pi}{\lambda_{ph}}$, where $\lambda_{ph} \approx 767$ nm. The first momentum kick will be in the direction of propagation of the cylindrical beam due to the absorption of a photon. The second will be in a random direction due to the spontaneous emission of a photon. For the $l = 1$ hollow light beam propagating along the axial direction of the cloud, we can ignore the effect of the first photon because it is along the imaging axis ($\hat{z}$). The momentum distribution of atoms after the spontaneous emission, $n_{bg}(k)$, is a convolution of the original momentum distribution of those atoms that absorb a single photon, $n_1(k)$, and a spherical shell with a radius of k_0. This can be written

$$n_{bg}(k) = \int n_1(|\vec{k} - \vec{p}|)\frac{\delta(p - k_0)}{4\pi p^2}d^3p = \frac{1}{2}\int_0^\pi n_1(k^2 + k_0^2 - 2kk_0 cos\theta)sin\theta d\theta \tag{B.1}$$

In an experiment, we cannot directly measure the momentum distribution of just the atoms that absorbed a single photon. However, a good approximation for $n_1(k)$ is to take the difference between the momentum distribution obtained with and without the hollow light beams, which is the momentum distribution of the atoms that absorbed at 1 or more photons.

The other hollow light beam propagates in the imaging plane (along $\hat{y}$) and so there will

be two photon recoils. This can be modeled by taking n_{bg} from Eq. B.1 and plugging it back into the same equation as n_1 to perform a second convolution. This neglects that the first photon kick will always be in a particular direction, but is a reasonable approximation since we take an azimuthal average of the images anyway. Typically, the background signal due to the $l = 2$ beams is approximately half the signal due to the other beam (based on blasting 50% of the atoms with $l = 1$ beam and 20% of the atoms with the $l = 2$ beam).

The procedure for analyzing images begins by taking images of atom clouds after time-of-flight expansion with and without the hollow light beams. We perform inverse Abel transforms on each image to obtain a 3D momentum distribution. We take the difference of the two momentum distributions to obtain $n_0(k)$ and then use Eq. B.1 to obtain the momentum distribution of the background signal. We scale the first background signal to have an amplitude given by $1.12TN(0)(1 - N(0))$ where we use the fraction of atoms remaining with the hollow light beams for $N(0)$. We scale the second background signal to be half of that. Finally, we subtract the background signal from the momentum distribution measured with the hollow light beam. A momentum distribution with and without the hollow light beams, as well as a calculated background signal are shown in Fig. 7.3.

Appendix C

Accounting for interactions with the third spin-state in measurements of the contact

In photoemission experiments, and measurements of the contact, we use an rf field to transfer atoms out of the strongly interacting system and into a weakly interacting state. In this thesis, the strongly interacting system consists of atoms in the $|9/2, -9/2\rangle$ and the $|9/2, -7/2\rangle$ spin states, which we will call states 1 and 2 respectively. The weakly interacting state is the $|9/2, -5/2\rangle$ state, which we will call state 3. It was pointed out in Ref. [111] that, due to residual interactions with the third spin state, rf spectra should go as $\omega^{-5/2}$ at large detunning, as opposed to the $\omega^{-3/2}$ tail predicted in the ideal case (Eq. 8.7). In Ref. [113], the exact form of the tail is derived and the authors find

$$\lim_{\nu\to\infty} \Gamma(\nu) = \frac{C}{2^{3/2}\pi^2}\nu^{-3/2}\frac{\left((k_F a_{12})^{-1} - (k_F a_{13})^{-1}\right)^2}{(k_F a_{13})^{-2} + \nu/2} \tag{C.1}$$

where a_{12} is the scattering length between the strongly interacting atoms, a_{13} is the scattering length between states 1 and 3, and ν is the rf frequency in units of the E_F/h with $\nu = 0$ defined as the single atom resonance. The rf field transfers atoms from state 2 to state 3. In the limit $k_F a_{13}$ small, this formula reduces to Eq. 8.7. In our experiments, the scattering length a_{13} is controlled by a Feshbach resonance at 224.2G [6], which has a width of 7.5 G [126]. At 202.2 G, which is the center of the Fesbach resonance for the 1 and 2 states, this gives a scattering length a_{13} of $233a_0$, and for a typical value of k_F, we find $(k_F a_{13})^{-1} = 9$, leading to a few percent correction to the value of the contact (Fig. C.1). The scattering length a_{13} varies by less than $10a_0$ over the range of magnetic-field strengths for the data presented here.

Final state corrections will also apply to the momentum distribution obtained from photoemission spectroscopy. To derive the high k tail from Eq. C.1, we use $\nu = 2k^2$, where k is the fermion wave-vector in units of k_F. This relation can be checked in the limit of rf dissociation of a dimer molecule. In this case, the initial state is a molecule with binding energy E_B. The final state is two atoms, each with momentum of magnitude k. Conservation of energy gives $\nu = E_B + 2k^2$. At large k, we can neglect E_B. Plugging this into Eq. C.1, we find,

$$N(k)dk = \Gamma(\nu)d\nu = \frac{C}{2\pi^2}k^{-2}\frac{\left((k_F a_{12})^{-1} - (k_F a_{13})^{-1}\right)^2}{(k_F a_{13})^{-2} + k^2}dk \tag{C.2}$$

where $N(k)$ is the number of atoms with wave-vector k. The momentum distribution, $n(k)$, is defined as $\frac{4\pi}{(2\pi)^3}n(k)k^2dk = N(k)dk$, such that

$$n(k) = Ck^{-4}\frac{\left((k_F a_{12})^{-1} - (k_F a_{13})^{-1}\right)^2}{(k_F a_{13})^{-2} + k^2}. \tag{C.3}$$

From this we see that the $n(k)$ obtained from photoemission spectroscopy will have a k^{-6} tail at very large k.

Fig. C.1 shows the contact extracted from rf spectra and photoemission data using the above equations, which take into account interactions with the third spin-state (red points). For comparison we also show the contact we reported in Ref. [10], where we neglected interactions with the third spin state (black points). While the corrections due to interactions with the third spin-state generally shift the data closer to the expected theory line from Ref. [22], the magnitude of the corrections is quite small. This justifies the approximation used in Ref. [10], which neglects the effects of interactions with the third spin-state.

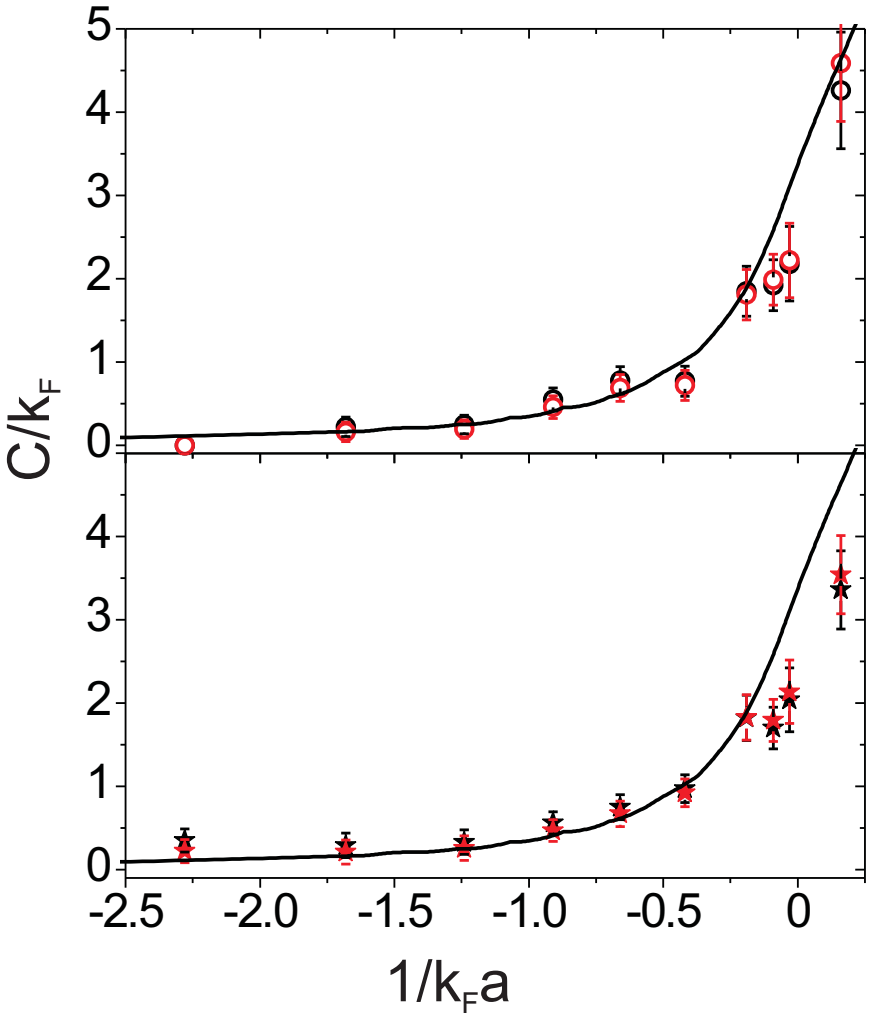

Figure C.1: **Interactions with third spin-state** Top) We plot the value of the contact extracted from photoemission data using Eq. 8.4 (black circles) and using Eq. C.3 (red circles), which accounts for the interactions with the third spin-state. On the BCS side ($1/k_F a < 0$), the correction leads to smaller values of the contact, while on resonance and on the BEC side ($1/k_F a < 0$), the correction leads to slightly smaller values. The solid line is the prediction from Ref. [22]. Bottom) We plot the value of the contact extracted from rf spectra using Eq. 8.7 (black stars) and using Eq. C.1 (red stars).

Appendix D

Simulating photoemission spectroscopy of molecules

RF dissociation of weakly interacting Feshbach molecules is a well understood process because the exact two-body wave-function of the molecule is known, see for example Refs. [74, 40]. This means we can simulate an atom photoemission experiment in the BEC limit, where interactions between the molecules can be ignored. In this appendix, I will explain in more detail how the simulation of Fig. 5.8 was obtained. I will also use the model to explore the effects of condensation and to look at the BCS-BEC crossover.

For a Feshbach molecule, the number of atoms outcoupled over a range of frequncies $d\nu$, as a function of rf frequency ν can be written [74]

$$\Gamma(\nu)d\nu = \frac{2\sqrt{E_B}}{\pi}\frac{\sqrt{\nu - E_B}}{\nu^2}d\nu \tag{D.1}$$

where ν is in units of E_F/h and E_B is the molecule binding energy in units of E_F. $\nu = 0$ corresponds to the transition energy for free atoms. The initial state is the bound molecule, and the final state is two free atoms with equal and opposite momentum k_ν, in the molecule center-of-mass frame. The energy of each atom is k_ν^2, where k_ν is given in units of k_F. From conservation of energy we have $\nu = E_B + 2k_\nu^2$. We plug this into Eq. D.1 to get the distribution of relative momenta for dissociated molecules

$$N(k_\nu)dk_\nu = \frac{2^{7/2}\sqrt{E_B}}{\pi}\frac{k_\nu^2}{(E_B + 2k_\nu^2)^2}dk_\nu. \tag{D.2}$$

For non-Bose-condensed molecules, there will also be a center-of-mass momentum. We assume this momentum distribution will be a gaussian distribution with a variance $\langle k_{cm}^2 \rangle$. In a

trapped $T = 0$ Fermi gas $\langle(\frac{k}{k_F})^2\rangle = \frac{3}{8}$, which is the ratio corresponding to the average kinetic energy per atom compared to the Fermi energy. Thus, an estimate for the variance in the pair momentum distribution is $\langle k_{cm}^2\rangle = \frac{3}{4}$ (twice the single-atom variance). In the case of Fig. 5.8, we calculated $\langle k_{cm}^2\rangle$ by assuming the molecules are in thermal equilibrium with unpaired atoms, whose momentum distribution we measure. For that case, we find $\langle k_{cm}^2\rangle = 1.3$. To simulate a gas with a condensate of molecules, we can set a fraction of the molecules to have a center-of-mass momenta equal to zero.

The total momentum the atom will be $k = k_\nu \pm k_{cm}/2$. The single-particle energy of the atom, E_S, is calculated from Eq. 5.7. Specifically, we have $E_S = k^2 - \nu = k^2 - (E_B + 2k_\nu^2)$.

To create simulated photoemission data: I fix the binding energy E_B, assume k_{cm} and k_ν are independent, generate a list of atoms obeying the probability distributions for k_{nu} and k_{cm}, calculate k and E_s for each atom, and then plot the number of atoms versus E_s and k. In these simulations I set $\langle k_{cm}^2\rangle = 1.1$.

The results of three simulated experiments with values of $E_B/E_F = 2.5, 1.0$, and 0.5 are shown in Fig. D.1. Fits to the EDCs are shown in Fig. D.2. As noted previously, in the limit of weakly bound molecules this simulation will be exact, and for $E_B/E_F = 2.5$ the simulation agrees well with the data in the BEC limit (as discussed in Chap 5 and Fig. 5.8). The center-of-mass momenta of the pairs leads to the observed energy widths, as can be seen in Fig. D.3, where a condensate of pairs leads to a sharp spectral feature. It is interesting that the energy widths are large, even for the long-lived pairs in the deeply bound-molecule regime. This shows explicitly that large energy widths of the single-particle excitations does not necessarily correspond to short-lived pairs, strong interactions between the pairs, or large pair binding energy. Rather, in this case, the large energy widths arise only from the center-of-mass momentum distribution of the pairs.

It is interesting to look at simulations for a gas of molecules with small binding energy compared to the Fermi energy. This is shown on the right hand side of Fig. D.1 and with a log-scale color map in Fig. D.4. Here the simulation produces spectral functions with a BCS-like dispersion with back-bending. In fact, this simulation is qualitatively similar to photoemission

data taken near the center of the BCS-BEC crossover (Fig. 6.13). The qualitative agreement is surprising because interactions between pairs must play an important role in the BCS-BEC crossover. Nevertheless, it is suggestive that the pseudogap phase could consist of long-lived pairs that have a large center-of-mass momenta.

In Fig. D.3, a simulation for a gas with $E_B = 2.5$ and a 20% condensate fraction is shown. The condensate leads to a sharp feature with a dispersion $E_S = -E_B - k^2$. While this feature should be observable in experiments, where we can obtain condensate fractions as high as 15%, it has not been seen. The feature could be washed out due to finite experimental resolution, or a condensate that still has significant center-of-mass motion of the pairs due to strong interactions (we have only obtained condensates for $1/k_F a < 1$). This is an interesting subject for future experiments.

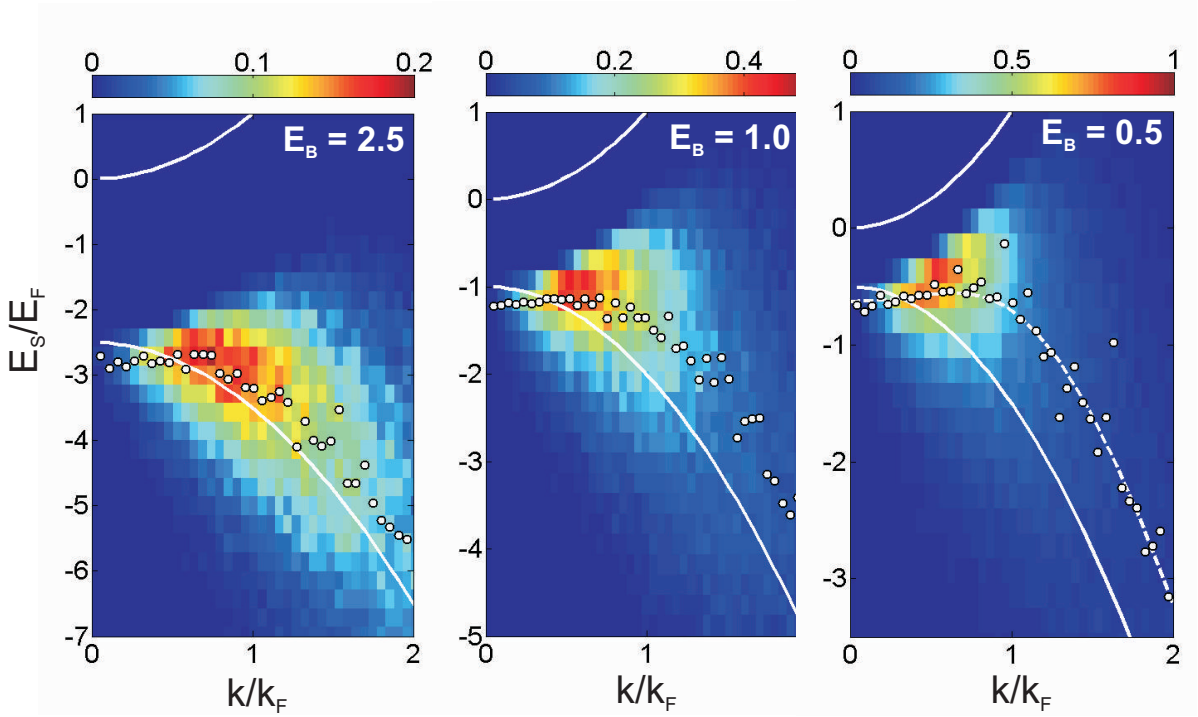

Figure D.1: **Simulated photoemission spectra** Three simulated photoemission spetra are shown for different values of the molecule binding energy E_B/E_F, labeled in the upper right corner. The upper white line is the free-particle dispersion. The lower white line is the dispersion that would be obtained in the limit of zero center-of-mass momentum of the molecules. The white circles are obtained from gaussian fits to the EDCs. As E_B decreases, the effect of the center-of-mass motion of the molecules becomes important at low k/k_F, and leads to a flattening, and eventually a BCS-like back-bending in the dispersion. For the spectrum with $E_B/E_F = 0.5$, a dashed line shows a BCS fit to the centers of the gaussians. The best fit parameters are $\mu, k_L, \Delta = 0.52 \pm 0.14, 0.64 \pm 0.07, 1.07 \pm 0.15$.

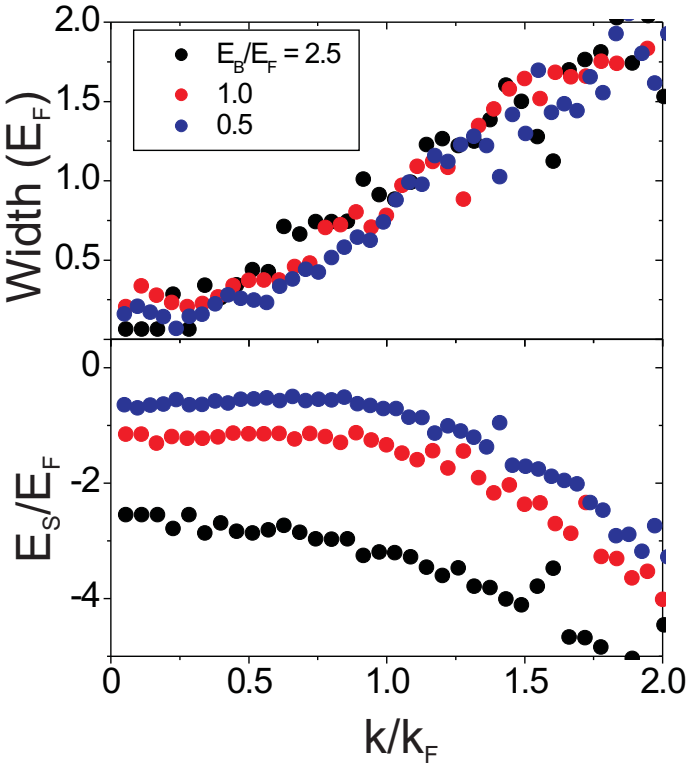

Figure D.2: **Dispersions and energy widths** The results of gaussian fits to the EDCs of simulations with the same parameters as those in Fig. D.1 are plotted versus k/k_F. Black circles correspond to the data with $E_B/E_F = 2.5$, red circles with $E_B/E_F = 1.0$, and blue circles with $E_B/E_F = 0.5$. Top) The rms widths, in units of the Fermi energy, are plotted. They are similar for all three data sets and increase as a function of k/k_F. The large energy widths are due to the center of mass momenta of the molecules. These widths can be compared to those in Fig. 6.15. Bottom) The centers of the gaussian fits.

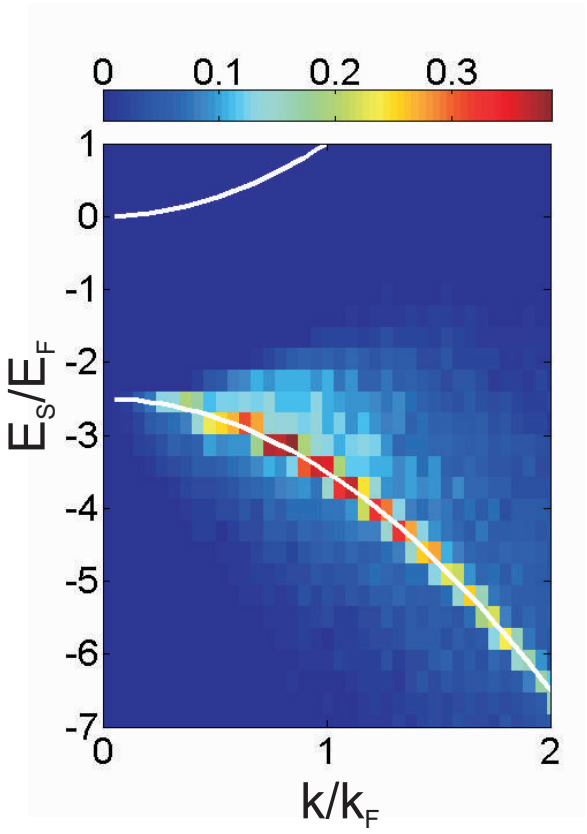

Figure D.3: **Simulated spectrum with a condensate** A simulated photoemission spectrum for a gas with $E_B/E_F = 2.5$ and a 20% condensate fraction. The condensate creates a sharp signal that exactly follows the lower white line, which is the dispersion in the limit of zero center-of-mass momentum. In the simulation, the condensate was given a small center-of-mass momentum spread $\langle k_c m^2 \rangle = 0.003 k_F$, so that it has a finite width in the simulated spectrum.

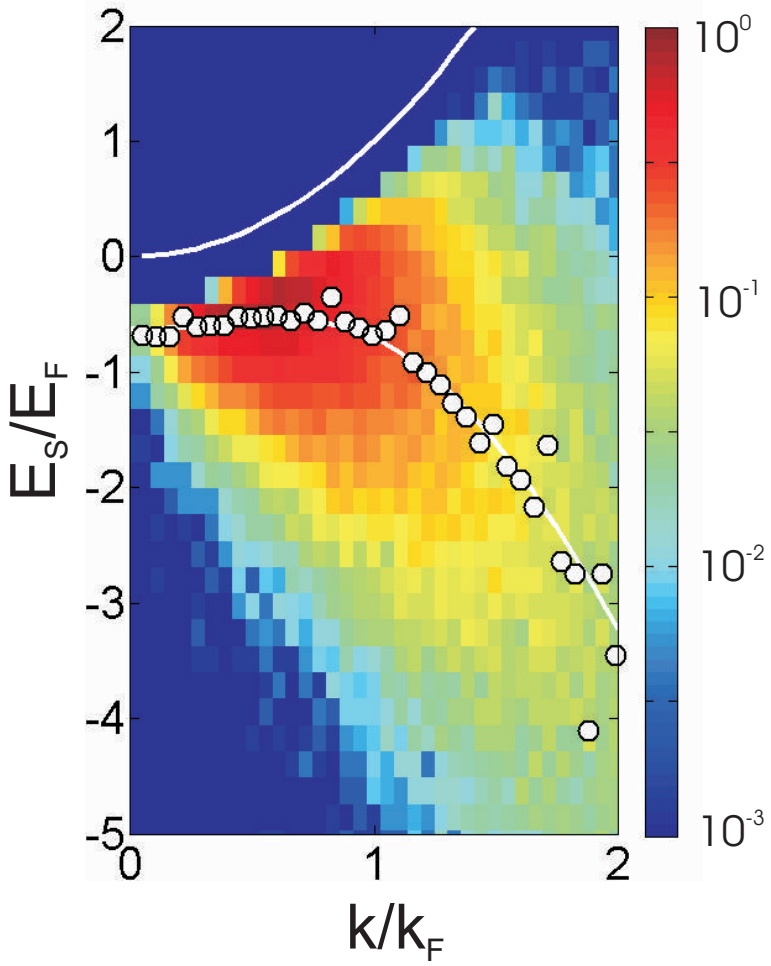

Figure D.4: **Log plot of photoemission simulation** This plot of the simulation with $E_B/E_F = 0.5$ (right hand side of Fig. D.1) uses a log intensity colormap and can be compared to the photoemission data in the pseudogap regime plotted in Figs. 6.6 and 6.13. The upper white line is the free particle dispersion. The lower white line is a BCS-fit to the data; the best fit parameters are given in the caption of Fig. D.1.